Bi-Global Investigation on the Secondary Instability of the Swept Hiemenz Boundary Layer

Bi-Global Investigation on the Secondary Instability of the Swept Hiemenz Boundary Layer

Barna E. M. Becsek

Mechanical Engineering MSc

Master Thesis HS 2013

Institute of Fluid Dynamics, IFD
ETH Zürich

Advisor: MSc ETH Mech. Eng. Michael O. John

Professor: Prof. Dr. Leonhard Kleiser

In loving memory of Ludmilla Krenicky

Abstract

The present work deals with the secondary bi-global instability of the swept Hiemenz boundary layer (SHBL) flow. It is the incompressible viscous flow along the attachment line of a wing that is swept backwards, i.e. not extending perpendicularly from the fuselage. The critical Reynolds number of classical linear stability theory is $\mathrm{Re}_{\mathrm{lin,crit}} = 583.1$, and modes with positive growth rates are found by stability calculations at $\mathrm{Re} = 300$, approaching the experimentally observed value of $\mathrm{Re} \approx 250$.
The flow stability is analysed by solving stability equations discretized in two dimensions, namely the chordwise x and normal y-direction. The stability equations are reformulated into a two-dimensional eigenvalue problem which is solved iteratively with an Arnoldi algorithm. The base flow for the stability equations is composed of a laminar SHBL and superimposed disturbance velocities. The base flow is extended from the ansatz introduced by Hiemenz for the classical SHBL analysis to one that is dependent on both x and y. The disturbances feature a bi-global dependence on chordwise and normal dimensions and a wave ansatz in the spanwise z direction.
The work first lays down the corresponding fundamentals of secondary stability theory, followed by the description of the numerical methods employed, providing general information as well as information on improvement of the code and the evaluation of the data. It then presents a numerical validation of the code (with benchmark data from literature) in which the numerical differentiation scheme was altered, the computational speed was increased by changing the implementation of the boundary conditions and the newly derived equations were incorporated. While the secondary problem converges smoothly in y, the solution was found to diverge after a certain optimal resolution in x.
Five distinct discrete modes were identified depending on the boundary conditions. The solutions are analysed in dependence of physical parameters such as the base flow, the wave number γ, boundary conditions and the spanwise downstream location. They are investigated both in the context of the discrete spectrum as well as the individual velocity components. Additionally, they are presented in a three-dimensional setting for better visualisation. The solutions are then compared to former findings in a dissertation dealing with the later stages of transition on a swept wing through crossflow instability.

Zusammenfassung

Die vorliegende Arbeit beschäftigt sich mit der sekundären bi-globalen Instabilität der schiebenden Hiemenz-Grenzschicht (SHGS) Strömung. Es ist die inkompressible, viskose Strömung entlang der Anlegelinie eines Flügels, welcher nach hinten angestellt ist (gepfeilt), d.h. sich nicht senkrecht vom Rumpf ausstreckt. Die kritische Reynolds-Zahl der klassischen linearen Stabilitätstheorie ist $\mathrm{Re}_{\mathrm{lin,crit}} = 583.1$ und Moden mit positiven Wachstumsraten werden gefunden bei $\mathrm{Re} = 300$, wodurch der experimentell beobachtete Wert $\mathrm{Re} \approx 250$ angenähert wird.
Die Stroömungsstabilität wird analysiert, indem in zwei Raumrichtungen diskretisierte Stabilitätsgleichungen, nämlich in Flügeltiefen- x und Flügelnormalenrichtung y, gelöst werden. Die Stabilitätsgleichungen werden in ein zweidimensionales Eigenwertproblem umformuliert, welches iterativ mit einem Arnoldi-Algorithmus gelöst wird. Die Grundströmung für die Stabilitätsgleichungen besteht aus einer laminaren SHGS und superponierten Störungsgeschwindigkeiten. Die Grundströmung wird vom Ansatz, der von Hiemenz eingeführt wurde, erweitert zu einer bi-globalen Abhängigkeit von x und y. Die Störungen folgen einem bi-globalen Ansatz in Flügeltiefen- und Flügeltnormalenrichtung und einem Wellenansatz in Spannweitenrichtung z.
Die Arbeit beschreibt zuerst die entsprechenden Grundlagen der sekundären Stabilitätstheorie, gefolgt von der Beschreibung der angewandten numerischen Methoden, wobei sowohl allgemeine Auskunft als auch Auskunft über die Verbesserung des Codes und die Auswertung der Daten gegeben wird. Anschliessend präsentiert sie eine numerische Validierung des Codes (mit Referenzdaten aus der Literatur), in welchem das numerische Differenzenschema geändert, die Rechenzeit verringert wurde und in welchen die neuen Stabilitägleichungen eingebunden wurden. Während die Lösung des sekundären Problems in y glatt konvergiert, zeigte sie in x-Richtung divergentes Verhalten ab einem bestimmten Optimum.
Fünf verschiedene diskrete Moden wurden je nach Randbedingungen identifiziert. Die Lösungen werden in Abhängigkeit physikalischer Parameter wie der Grundströmung, der Wellenzahl γ, Randbedingungen und der Flügeltiefenlage stromabwärts analysiert. Sie werden sowohl im Zusammenhang mit dem diskreten Spektrum als auch mit den einzelnen Geschindigkeitskomponenten behandelt. Ausserdem werden sie in einem dreidimensionalen Umfeld visualisiert. Die Lösungen werden daraufhin mit früheren Resultaten einer Dissertaion, welche sich mit den Spätstadien der Transition durch Querströmungsinstabilität auf gepfeilten Flügeln beschäftigte, verglichen.

Acknowledgements

In the course of this project at IFD at ETH I have had the chance to broaden my knowledge of flow stability extensively. I have witnessed a very professional, motivating, encouraging and inspiring work environment. I would like to thank my supervisor Michael John who throughout the entire time was very forthcoming and knowledgeable in kindly answering questions and discussing problems. Further, I would like to also extend my thanks to Prof. Dominik Obrist who kindly shared his great expertise on the field when addressed. Finally, I would like to say thanks to Prof. Leonhard Kleiser, head of the institute's group, for offering exciting topics of research and simultaneously showing interest in the students' work.

Contents

Nomenclature

Abbreviations

AoA	angle of attack
ASBL	asymptotic suction boundary layer
BC	boundary condition
BF	base flow
CoM	center of mass
DNS	direct numerical simulation(s)
EV	eigenvalue
GH	Görtler-Hämmerlin
HBL	Hiemenz boundary layer
HSS	high-speed streak
LFC	laminar flow control
LSS	low-speed streak
LST	linear stability theory
NACA	National Advisory Committee for Aeronautics
NASA	National Aeronautics and Space Administration
NSE	Navier-Stokes equations
ODE	ordinary differential equation
PDE	partial differential eqution
SH	swept Hiemenz
SHBL	swept-Hiemenz boundary layer

Greek Symbols

α	angle of attack
χ	weighting parameter
Δ	reference length scale

δ	boundary layer thickness (dimensionless)
η	dimensionless normal coordinate
γ	wave number in spanwise (downstream) direction
κ	dimensionless suction parameter
ω	angular frequency
ω_i	vorticity component
∂_i	partial derivative operator with respect to i, short for $\partial/\partial i$
ϕ	maximum of local vector norm $\phi = \max\|(\|\hat{u}(x,y)\|, \|\hat{v}(x,y)\|, \|\hat{w}(x,y)\|)^T\|$
Ψ	scalar streamfunction for planar base flow
τ	time scale
φ	sweep angle
ξ_j	Gauss-Lobatto grid points

Roman Letters

$\hat{u}$	disturbance velocity chordwise component amplitude
$\hat{v}$	disturbance velocity normal component amplitude
$\hat{w}$	disturbance velocity spanwise component amplitude
$\mathcal{Q}, \mathcal{R}$	eigenvalue matrices
Re	Reynolds number
a	strain rate
A_1	primary amplitude
A_2	secondary amplitude
c	wave speed
F	dimensional ansatz for the Hiemenz-flow components
f	dimensionless similarity variable
g	similarity variable
h	similarity variable
J_i^k	minimal cost of going to end node from node i at stage k
L_x	domain size in x direction
L_y	domain size in y direction

N_x	number of grid points in x direction
N_y	number of grid points in y direction
p	pressure
R^*	outer potential cylinder flow radius
U	inner base flow chordwise velocity component
u	chordwise total velocity component
U^*	dimensional outer flow chordwise velocity component
u'	chordwise disturbance velocity component
U_∞	far-field chordwise velocity component
U_B	base flow chordwise velocity component
u_i	velocity component in index notation
V	inner base flow normal velocity component
v	normal total velocity component
V^*	dimensional outer flow normal velocity component
v'	normal disturbance velocity component
V_0	suction velocity at the wall ($v(y=0) = -V_0$)
V_B	base flow normal velocity component
W	inner base flow spanwise velocity component
w	spanwise total velocity component
W^*	dimensional outer flow spanwise velocity component
w'	spanwise disturbance velocity component
W_∞	far-field spanwise velocity component
W_B	base flow spanwise velocity component
x	chordwise coordinate
X^*	dimensional outer flow chordwise coordinate
x_{half}	grid stretching parameter in x direction
y	normal coordinate
Y^*	dimensional outer flow normal coordinate
y_{half}	grid stretching parameter in y direction

z	spanwise coordinate
Z^*	dimensional outer flow spanwise coordinate
z_{extr}	extraction coordinate in spanwise direction

List of Figures

List of Tables

1. Introduction

1.1. Motivation

The flow scenario investigated in this work is that of a fluid flowing along the leading-edge of a swept wing, i.e. a wing that is angled back at the fuselage away from the parallel free stream as shown in Figure 1.1. Investigations have shown that such wing configurations present a high affinity to turbulent flow over the wing, unlike wings that are stretched outward perpendicularly from the fuselage. Even though turbulent flow over a wing may offer desired advantages over a

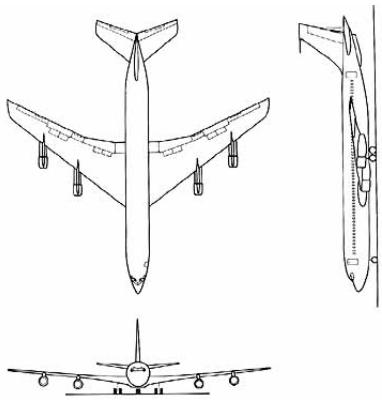

Figure 1.1.: A swept wing aircraft configuration. From the top the angle of the wings towards the back is apparent. NASA, [25].

laminar one (e.g. a higher resistance to adverse pressure gradients which results in delayed flow separation [19]) generally laminar flows are preferred in today's aeronautical design since the mentioned swept-wing configuration is most commonly found on commercial airliners. In that case, laminar flow around a wing offers lower friction drag due to lower rates of shear [24]. For these daily operating means of transport it is of great interest to improve efficiency.

1.2. Background

Early experimental investigations have found that certain stationary flow features called cross-flow vortices that were approximately aligned with the streamlines over the wing established themselves in the wing boundary layer. W. E. Gray [11] described Görtler-vortex-like flow patterns evolving on the wing only a small distance away from the leading edge. He lists them

in flight tests with wings of different sweep angles and leading-edge radii that all showed similar characteristics. Their eventual breakdown caused the flow over the wing to be contaminated. Later, F. W. Boltz [3] analysed the instability on swept wings in an experimental laboratory setup on untapered, unchambered (symmetrical) profile wings. He varied the sweep angle and the angle of attack in order to characterize the onset of instabilities. His results showed that sweep indeed has a significant effect on the flow stability and he claimed that depending on the AoA the transition could be categorized into one of two transition scenarios. It either was of viscous type which he called Tollmien-Schlichting type or of inviscid type. Thus, the AoA (as a function of the sweep angle) was responsible for dividing transition into these two domains. In different configurations of AoA, the side of the wing that experienced adverse pressure gradients (since the wing was symmetric) would show sooner formation of vortex-like structures that were immediately followed by a forward (chordwise) propagation of the transitional loci. Furthermore, flow visualization techniques showed that these vortices were well aligned with the primary streamlines of the flow and that they exhibited stationary patterns with spacings that were proportional to the boundary-layer thickness. Boltz also reported that the vortices all rotate in the same direction.

Poll [33] carried out experimental investigations at the leading edge of an aerofoil and introduced disturbances in different ways, e.g. by using trip-wires or a flat plate on which turbulence was generated. Poll measured the disturbance growth as a function of a similarity variable, the trip wire diameter and the separation distance between the trip wire and the turbulence detector, while turbulence would initially turn up as discrete bursts. He was able to find that there are upper and lower bounds for the detection of such bursts. Lower bounds correspond to small triggering disturbances and lie at Re= 600 and the upper bounds corresponding to large triggering disturbances can be found at Re= 245. Later, linear stability theory could confirm the lower bound of $\mathrm{Re}_{\mathrm{crit}} = 583.1$, while still no theoretical explanation exists for the upper bound of $\mathrm{Re}_{\mathrm{global}} \approx 250$.

Simultaneously, effort was put into ways of controlling the onset of instabilities or at least delaying their formation. A very popular way of achieving this was applying suction through the skin of the wing thereby removing part of the boundary layer and with it disturbances that may have developed into potential instabilities. This proved to be a very effective means of flow control when introduced correctly. Pfenninger [32] for that sake conducted studies that support the feasibility of flow control wings. He states that according to theory the largest suction is to be applied in regions of highest absolute pressure gradients, i.e. close to the attachment line and the trailing edge. He further investigated the effect of suction ducts and perforations in the wing surface and observed that for badly placed holes, horseshoe-like vortices shed from the perforations and were responsible for premature transition to turbulence on the wing. Nonetheless, he was able to show that the critical Reynolds number can be raised by applying suction. He obtained results of patterns that show co-rotating vortices on the wing as already seen above and also confirmed the role of the AoA on stability. Initial experiments were carried out on a 30° swept modified NACA 66012 LFC wing and eventually tests were undertaken on a modified wing of the Northrop X-21A experimental aircraft. Of course, introducing such perforations goes with the expense of structural integrity of the wing structure, for which he

redirects to an investigation carried out by Northrop (also found in [32]). This topic is, however, not within the scope of this thesis and will not be further elaborated herein.

Gaster on the other hand proposed a component to be mounted to the front of the wing at the attachment line close to the fuselage. This so-called *Gaster-Bump* would provide for turbulent flow (originating from the fuselage) deceleration along the attachment line and thus prevent transition from occurring or at least raise the critical Reynolds number [9].

There have also been various theoretical and numerical analyses concerning this stability problem. Mathematical models for a planar stagnation point (or line) flow have been proposed by Hiemenz [16] and later have been extended to the three-dimensional swept Hiemenz (SH) flow. By adding sweep to the wing of an airplane there is an added spanwise velocity component along the leading edge of the wing from the fuselage to the tip. The base flow is an exact solution to the NSE. Later, Görtler [10] and Hämmerlin [15] suggested an ansatz for superimposed disturbances for linear stability theory whose solution is known as the Görtler-Hämmerlin (GH) eigenmode. The disturbance equations are derived by plugging the complete base flow with superimposed disturbances into the NSE, removing the base flow solution and linearizing the remaining equations. The LST poses an eigenvalue problem to the disturbances with either temporal (complex frequency) or spatial setting (complex wave number). The *temporal* LST for the SHBL has identified a critical Reynolds number of $\mathrm{Re} = 583.1$. The first ones to numerically solve this problem were Hall et al. [13]. Further, Lin and Malik [26] identified certain eigenmodes of the LST, also recovering the GH eigenmode. Another contribution of similar statement was produced by Robitaillié-Montané [35]. Obrist [28] makes use of a spectral method where he employs Hermite polynomials as an ansatz for the disturbances. He further addresses the phenomenon of transient disturbance growth and takes up the idea of receptivity of flows to external disturbances. Using the spectral approach he as well recovers the GH Mode for a polynomial order of $N = 1$ [30]. For higher-order modes he distinguishes their behavior outside the boundary layer in normal direction, he identifies algebraically decaying modes which he states belong to the continuous spectrum whereas the exponentially decaying modes constitute the discrete spectrum. Additionally, even and odd modes in the order N are distinguished. A more general and recent approach to the SHBL LST was conveyed by Theofilis et al. [31], who solved an extended BiGlobal PDE model to the disturbance equations, recovering results that confirmed former findings. Their work additionally included the addition of a non-zero angle of attack which they varied as a parameter.

As the results of linear theory were not in complete agreement with the experimental data, particularly with respect to the critical Reynolds number, new theoretical models and investigations arose. Models were extended to include non-linear effects. For that sake DNS were carried out with some disturbance in the boundary layer flow. The instabilities were usually *primarily* triggered by counterrotating vortices that depending on the sign of their amplitude A_1 created low- or high-speed streaks along the attachment line with adjacent high- and low-speed streaks, respectively. This means of triggering was shown to be the optimal initial condition for linear disturbance growth [12]. Already earlier, Asai et al. have conducted experimental research on the breakdown of these boundary layer streaks [2]. Following that, Brandt presented numerical results on the breakdown of near-wall streaks [5], [4]. As for the *spatial* formulation of the sta-

bility problem, Obrist has shown [29] that adding a *secondary disturbance* of smaller amplitude A_2 on top of the counterrotating vortices leads to subcritical (Re = 300) transition of the SHBL.

At this point it is important to mention that instability of a flow generally can be of two types. Either it is triggered solely by the flow profile and the corresponding pressure gradients, in which case it is referred to as being of the inviscid type (corresponding to a Re $\rightarrow \infty$, see definition for Re). Criterions for the classification of inviscid (in-)stability have been derived by Rayleigh, who states that in order for a flow to be inviscidly unstable there has to be an inflection point in its velocity profile, i.e. the second derivative of the velocity has to change sign at least once over a coordinate. Fjørtoft has added a stronger criterion to that of Rayleigh's, in which he requires the product of the second derivative of the velocity times the difference of the local velocity and the inflection point velocity to be less than zero along a coordinate. The latter basically requires the velocity profile to have an irregularity somewhere. Both criterions present *necessary* conditions for *inviscid instability* [23].
Or, flow instability can be triggered by the viscosity of a fluid [23], i.e. by the shear, in which case one speaks of viscous instability. In certain cases, however, viscosity may have a stabilizing effect rather than a destabilizing one. The viscous stability theory has been derived over the years for many flow scenarios, many of them two-dimensional or reduced to a quasi two-dimensional model with the consideration of symmetry.

1.3. Thesis Outline

The boundary-layer flow investigated here is the three-dimensional incompressible swept Hiemenz flow with superimposed vortices as primary disturbances that build up a high-speed streak along the attachment line. The disturbances are triggered further by secondary disturbances of time-periodic type vortex amplitude changes. The above mentioned experimentally observed crossflow instability (crossflow vortices) present on the wing surface is described by the Falkner-Skan-Cooke boundary layer which is a three-dimensional extension of the two-dimensional Falkner-Skan boundary layer dealing with flows subject to favorable or adverse pressure gradients. This type of flow will not be elaborated further in this context, since the flow of interest is that along the attachment line. Figure 1.2 shows the two different boundary layers present on a swept wing.

In this thesis effort is put in identifying certain solutions of the bi-global secondary eigenvalue problem for a range of parameters including different base flows, the wave number γ, the spanwise downstream location of the flow and different boundary conditions. The experimentally observed critical Reynolds number of around Re$\approx$ 250 is aimed to be explained or approximated by secondary instability theory on a flow of Re= 300.

In a first part, the theoretical groundwork is presented and laid out in Chapter 2 so as to offer a physical insight into the mechanisms present in this particular problem. It first presents the underlying governing equations in Section 2.1 upon which the specific mathematical background available for this kind of flow is presented in Section 2.2. The report proceeds with the description

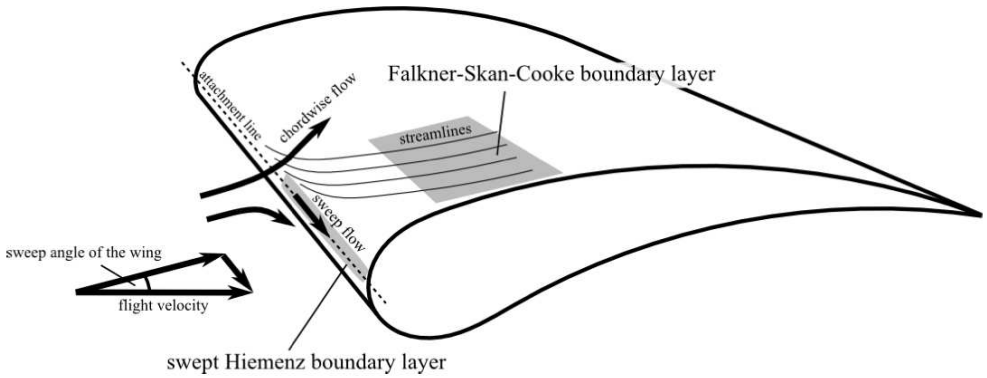

Figure 1.2.: The two boundary layer types present on a swept wing. The principal streamlines of the flow are qualitatively sketched out. [23].

of the base flow in Section 2.3. Chapter 2 then concludes with the bi-global stability theory and newly derived equations.

In Chapter 3, the utilised numerical code framework[1] and extensions made as part of the present work are elaborated in Section 3.1, followed by a presentation of post-processing algorithms in Section 3.2.

Chapter 4 demonstrates the validation of the changes made to the original code in Section 4.1 by comparison to benchmark data from literature, monitors the code's performance in Section 4.2 and analyses numerical convergence of the secondary SHBL eigenvalue problem in Section 4.3.

Eventually, Chapter 5 presents and visualizes the obtained solution to the secondary SHBL eigenvalue problem. First, Section 5.1 quantifies errors resulting from a modification of the base flow that is described in Section 2.3.1. Second, in Section 5.2 the results are shown in the context of the eigenvalue spectrum and the eigenmodes' characteristics are pointed out. Subsequently, the solutions are analysed more precisely in Section 5.3 by means of the velocity components. Section 5.4 then provides a more visual approach of presentation of the solutions in a three-dimensional setting. In the last Section 5.5 the results of a bi-global investigation of crossflow instability are briefly brought up for comparison.

[1]The code was originally written by Prof. Dominik Obrist and tested by Pascal Diggelmann.

Chapter 6 concludes the thesis by summarizing the main points of the thesis and discussing possible extensions to the investigation.

2. Mathematical Fundamentals

2.1. Governing Equations

This theoretical study deals with the stability of incompressible viscous fluid flow. The governing equations that describe the evolution of such flows are the incompressible continuity equation

$$\frac{\partial u_i}{\partial x_i} = 0, \tag{2.1}$$

the incompressible Navier-Stokes equations

$$\frac{\partial u_i}{\partial t} + u_j \frac{\partial}{\partial x_j} u_i = -\frac{\partial p}{\partial x_i} + \frac{1}{\mathrm{Re}} \frac{\partial^2}{\partial x_j \partial x_j} u_i \tag{2.2a}$$

or, alternatively, the vorticity equation that is derived by taking the curl of the NS-equations (2.2a)

$$\frac{\partial \omega_i}{\partial t} + u_j \frac{\partial}{\partial x_j} \omega_i = \omega_j \frac{\partial}{\partial x_j} u_i + \frac{1}{\mathrm{Re}} \frac{\partial^2}{\partial x_j \partial x_j} \omega_i. \tag{2.2b}$$

The coordinate system spans a cartesian space where

$$\begin{pmatrix} x \\ y \\ z \end{pmatrix} = \begin{pmatrix} x_1 \\ x_2 \\ x_3 \end{pmatrix} \tag{2.3}$$

and the directions are defined as follows:

$$x=\text{: chordwise}, \quad y=\text{: normal}, \quad z=\text{: spanwise direction.}$$

2.2. Previous Work[1]

2.2.1. Plane Stagnation Flow

For the planar case (corresponding to a wing with no sweep), Hiemenz [16] had proposed a solution to the viscous stagnation point (or line) flow by introducing the function $F(y)$. The

[1] This section is a summary based on [36], [28], [23], [21] and [7]

flow field ansatz

$$\begin{pmatrix} u(x,y) \\ v(y) \end{pmatrix} = \begin{pmatrix} xF'(y) \\ -F(y) \end{pmatrix} \tag{2.4}$$

satisfies the continuity and Navier-Stokes equations exactly. Substituting (2.4) into the Navier-Stokes equations, results in the third-order ordinary differential equation

$$\nu F''' + FF'' - F'^2 + a^2 = 0, \tag{2.5}$$

where $a = U_\infty \Delta$ is the strain rate and ν the kinematic viscosity of the fluid. Constructed with the length scale Δ based on the strain rate a and kinematic viscosity ν, the parameters a and ν can be dropped with

$$\eta = \alpha y = \frac{y}{\Delta}, \tag{2.6a}$$

$$\alpha = \sqrt{a/\nu} = \frac{1}{\Delta}, \tag{2.6b}$$

$$f(\eta) = F(y)/(\nu\alpha), \tag{2.6c}$$

that provide the non-dimensional ansatz

$$\begin{pmatrix} u(x,\eta) \\ v(\eta) \end{pmatrix} = \begin{pmatrix} axf'(\eta) \\ -\sqrt{a\nu} f(\eta) \end{pmatrix}, \tag{2.7}$$

with which the equation reads

$$f''' + ff'' - f'^2 + 1 = 0. \tag{2.8}$$

Equation (2.8) constitutes a simple numerical problem with boundary conditions

$$f(0) = \kappa, \quad f'(0) = 0, \quad f'(\eta \to \infty) = 1$$

$$\kappa = \frac{V_0}{\sqrt{\nu a}} \qquad (= 0 \text{ in case of no suction}).$$

2.2.2. Three-Dimensional Stagnation Flow

When considering flow over a swept wing, the stagnation point becomes an attachment line. Mathematically, this can be described by adding a constant spanwise velocity component W_∞^* to the far field. The ansatz for the boundary-layer flow component is

$$w(\eta) = W_\infty^* g(\eta). \tag{2.9}$$

Inserting (2.7) and (2.9) into the NSE gives an additional ODE to the already known Equation (2.8):

$$g'' + fg' = 0 \tag{2.10}$$

with boundary conditions

$$g(0) = 0, \quad g(\eta \to \infty) = 1. \tag{2.11}$$

Using W_∞^* as the reference velocity, together with the reference length scale Δ (2.6b) leads to the SHBL Reynolds number

$$\mathrm{Re_{SH}} = \frac{W_\infty^*}{\sqrt{a\nu}} = \frac{W_\infty^* \Delta}{\nu}. \tag{2.12}$$

The three non-dimensional velocity components then are

$$\begin{pmatrix} U \\ V \\ W \end{pmatrix} = \begin{pmatrix} \frac{x f'(\eta)}{\mathrm{Re_{SH}}} \\ -\frac{f(\eta)}{\mathrm{Re_{SH}}} \\ g(\eta) \end{pmatrix}. \tag{2.13}$$

The solution to Equations (2.8) and (2.10) describes the exact laminar base flow of the SHBL.

Once the flow has been non-dimensionalized, the boundary layer thickness can be defined as either a distance from the wall where the flow reaches a certain percentage of the far-field value or by definitions stemming from *mass* and *momentum* conservation called *displacement* and *momentum* thickness, respectively. The different values are tabulated in Table 2.1. In subsequent Chapters of this thesis the boundary layer thickness will be considered $\delta = \delta_{0.9995}$ to illustrate the upper bound. All other BL thicknesses then lie within that bound.

Table 2.1.: Definitions of boundary layer thickness

99.95% thickness	$\delta_{0.9995} = 0.9995 \cdot W_\infty$	≈ 4
99%-thickness	$\delta_{0.99} = 0.99 \cdot W_\infty$	≈ 3.05
Momentum-thickness	$\delta_\theta = \int_0^\infty g(1-g)\mathrm{d}\eta$	≈ 0.404
Displacement-tickness	$\delta_u = \int_0^\infty (1 - \frac{w}{W_\infty})\mathrm{d}y$	≈ 1.026

2.2.3. Three-Dimensional Swept Cylinder Flow

In order to model the flow around a swept cylinder of radius R^* in a *constant* free-stream velocity V_∞^*, the **outer** potential flow has to be considered as shown in Figure 2.1. The flow around the cylinder consists of an inner and an outer flow region. The components $(U, V, W)^T$ from Equation (2.13) describe the exact non-dimensional swept Hiemenz boundary layer flow inside the boundary layer and constitute the **inner flow**. It is valid in the vicinity of the attachment line.

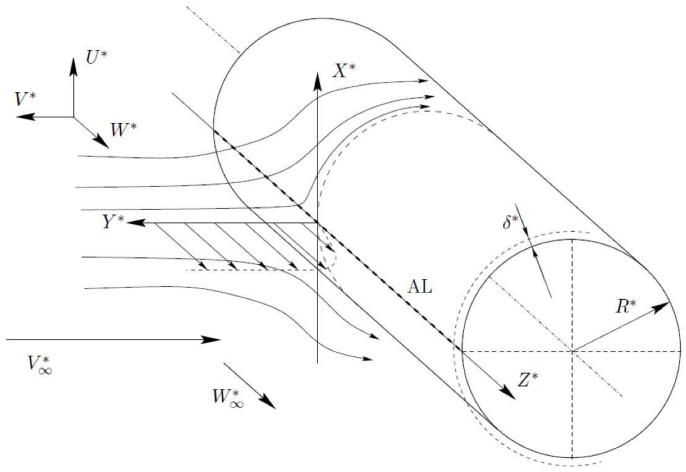

Figure 2.1.: Swept Hiemenz flow over a cylinder with its coordinate system, flow components and boundary layer. [28].

The inner flow is matched to the **outer flow** (Figure 2.2), whose components are[2]:

$$U^* = 2V_\infty^* R^* \frac{X^{*2}(Y^* + R^*)}{[X^{*2} + (Y^* + R^*)^2]^2} \tag{2.14}$$

$$V^* = -V_\infty^* \left\{ 1 + R^{*2} \frac{X^{*2} - (Y^* + R^*)^2}{[X^{*2} + (Y^* + R^*)^2]^2} \right\} \tag{2.15}$$

$$W^* = W_\infty^*. \tag{2.16}$$

The SHBL is a valid model for a three-dimensional swept cylinder flow as one approaches the attachment line, i.e. $X^* \to 0$, $Y^* \to 0$, with the potential

$$\Phi = aX^*Y^* \qquad \text{with strain rate } a = 2V_\infty^*/R^* \tag{2.17}$$

This limit flow is the boundary condition for the inner flow.

Disturbances are superimposed on the base flow (inner flow) and the first ones to suggest an ansatz for the disturbances were Görtler [10] and Hämmerlin [15]. They proposed the chordwise disturbance component be linearly dependent on the chordwise coordinate x with no dependence on x of the normal and spanwise disturbance components:

$$(u', v', w') = (xu(y), v(y), w(y))e^{\mathrm{i}\gamma(z-ct)} + \text{c.c.} \tag{2.18}$$

Hall [13] was the first to solve this problem with linear stability theory and he showed that below a $\mathrm{Re}_{\mathrm{lin,crit}} = 583.1$ the flow remained linearly stable. Later in 1988 Spalart [37] was able to confirm the solution to the linear stability problem of Görtler and Hämmerlin with DNS simulations (GH Mode).

[2] the superscript * marks dimensional values

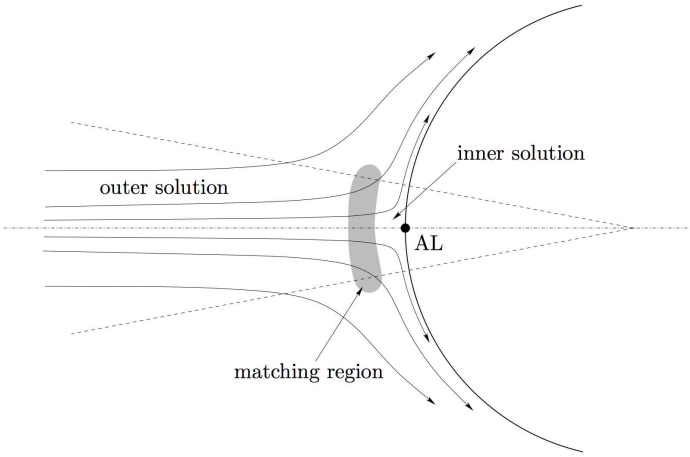

Figure 2.2.: Inner and outer flow regions of the swept Hiemenz boundary layer flow. The outer inviscid potential flow serves as a boundary condition for the inner flow. [28].

2.2.4. Generalized Flat-Plate Boundary-Layer Flows

John et al. [21] were able to merge the flow models of the Hiemenz, Swept Hiemenz and Asymptotic Suction boundary layers. By introducing a sweep angle $\varphi \in [0, \pi/2]$ and AoA α and redefining the reference quantities used for non-dimensionalization in order to satisfy both flow scenarios they were able to extend Equations (2.8) and (2.10) to the following

$$f''' + ff'' - f'^2 + \cos^2\varphi \sin^2\alpha = 0 \tag{2.19a}$$

$$h'' + fh' - f'h = \text{const.} \tag{2.19b}$$

$$g'' + fg' = 0, \tag{2.19c}$$

with the boundary conditions

$$f(0) = \kappa,\ f'(0) = 0,\ f'(\eta \to \infty) = \cos\varphi \sin\alpha \tag{2.20a}$$

$$g(0) = 0,\ g(\eta \to \infty) = 1 \tag{2.20b}$$

$$h(0) = 0,\ h'(\eta \to \infty) = \cos\alpha. \tag{2.20c}$$

κ in this case is defined as $V_0/\sqrt{\nu\gamma}$ and $h(\eta)$ describes the shear flow in x-direction. From this model one can recover the individual cases of the HBL ($\varphi = 0$, $\alpha = \pi/2$), SHBL ($\alpha = \pi/2$) and ASBL ($\varphi = \alpha = \pi/2$).

2.3. Base Flow

The employed code uses two different approaches to solving for the disturbance quantities. The first approach solely uses the analytical swept Hiemenz BF with a bi-global ansatz for the disturbances, whereas the second uses extended disturbance equations for a general base flow that is dependent on both x and y coordinates. The former is used herein for validation of the implemented grid resolution and difference schemes and the memory study. The latter is crucial for the solution of the bi-global secondary instability where the base flow is obtained from IMPACT[3].

2.3.1. Primarily Disturbed Base Flow

This base flow is obtained from the IMPACT DNS Simulations where the initial base flow consists of two counter-rotating vortices inside the swept Hiemenz boundary layer. These two vortices have a superimposed finite disturbance amplitude $A_2(\tau)$ which is fluctuating in time. Such flow configurations have been shown to be optimal sources of streak formation [12]. The so created high and low speed streaks eventually lead to lift-up of the flow and finally breakdown to turbulence. However, after the first transient disturbance growth has occured, new modes start to grow exponentially on top of the stream-wise vortices. It is these exponentially growing modes that are sought herein. Since the base flow is assumed to be of generally arbitrary shape of votices with high and low speed streaks of flow, but based on an exact solution and primary disturbances which fulfill the condition $\partial/\partial z = 0$, it was modelled to be dependent on x and y.

$$\begin{pmatrix} U \\ V \\ W \end{pmatrix} = \begin{pmatrix} U_B(x,y) \\ V_B(x,y) \\ W_B(x,y) \end{pmatrix}. \tag{2.21}$$

However, some minor dependence of $\underline{U}(\underline{x},t)$ on z exists, such that the extraction location

$$z_{\text{extr}} = \min_z \int_y \int_x \left(\frac{\partial}{\partial z} W\right)^2 \mathrm{d}x\mathrm{d}y \tag{2.22}$$

of the base flow plane on the z-axis was determined by searching for local minima in the divergence of the base flow in the region of secondary modal growth between primary transient growth and turbulent breakdown. Finding the location of minimal span-wise gradient of the span-wise component W makes sure the base-flow is as close to being divergence-free in the extraction plane as possible. The so extracted base-flow can then either be used in an unmodified state or to better conform with the two-dimensional continuity equation it can be 'relaxed'. Then, the extracted plane flow is artificially made into a planar potential flow by creating streamfunctions

$$\Psi_U = \int_y U(x,y)\mathrm{d}y + g(x), \qquad g(x) = -\int_x V(x, y = y_0)\mathrm{d}x \tag{2.23}$$

[3] An in-house DNS code from IFD at ETH for Incompressible Turbulent Flows with Compact differentiation on Massively Parallel Computers: http://www.ifd.mavt.ethz.ch/research/group_lk/projects/impact

and

$$\Psi_V = -\int_x V(x,y)\mathrm{d}x + f(y), \qquad f(y) = \int_y U(x = x_0, y)\mathrm{d}y \tag{2.24}$$

from both baseflow components U and V separately and combining these to a common streamfunction Ψ

$$\Psi = \chi\Psi_U + (1-\chi)\Psi_V, \qquad \chi \in [0,1]. \tag{2.25}$$

The weight χ is varied to control the contribution of the individual baseflow components to the streamfunction. The divergence-free base flow components U and V are then retrieved by

$$U = \frac{\partial}{\partial y}\Psi \quad \text{and} \quad V = -\frac{\partial}{\partial x}\Psi. \tag{2.26}$$

As a last step of pre-processing the BF, it is reduced to the domain where $x, y > 0$.

2.4. Bi-Global Stability

The total flow $(u, v, w)^T$ consists of the base flow quantities $(U, V, W)^T$, which are a solution to the Navier-Stokes equations, and superimposed disturbance quantities $(u', v', w')^T$

$$(u,\ v,\ w) = (U + u',\ V + v',\ W + w'). \tag{2.27}$$

For the biglobal stability problem discussed herein, the disturbance quantities are assumed to be globally dependent on x and y with a wave ansatz in the spanwise z-direction:

$$\phi' = \begin{pmatrix} u' \\ v' \\ w' \end{pmatrix} = \begin{pmatrix} \hat{u}(x,y) \\ \hat{v}(x,y) \\ \hat{w}(x,y) \end{pmatrix} \cdot e^{\mathrm{i}(\gamma z - \omega t)} + \text{c.c.} = \begin{pmatrix} \hat{u}(x,y) \\ \hat{v}(x,y) \\ \hat{w}(x,y) \end{pmatrix} \cdot e^{\mathrm{i}\gamma(z - ct)} + \text{c.c.} \tag{2.28}$$

In Equation (2.28) $\gamma \in \mathbb{R}$ represents the spanwise wave number and $\omega \in \mathbb{C}$ is the angular frequency. Alternatively one can define $c = \frac{\omega}{\gamma} \in \mathbb{C}$. Then the real part $c_r = \mathcal{R}\{c\}$ denotes the phase speed of that particular monochromatic wave and the imaginary part $c_i = \mathcal{I}\{c\}$ denotes the growth or decay rate of the particular eigenmode. Summarizing:

c_r	Phase Speed
$c_i > 0$	$\propto$ growth rate (temporally unstable eigenmode)
< 0	$\propto$ decay rate (temporally stable eigenmode).

When inserting (2.27) into the NS-equations, neglecting the resulting nonlinear terms, then subsequently substracting the base flow solution, one ends up with linearized disturbance equations for all three velocity components. From these three equations the pressure disturbance p' and the spanwise velocity component w' can be eliminated by taking the curl of the linearized disturbance equations and employing the continuity equation. Doing so results in two equations in u' and v' which can be arranged in a way to formulate the eigenvalue problem that is sought to be solved. Alternatively, the equations can also be derived by directly inserting (2.27) into the

vorticity equation and proceeding from there. Depending on the applied base flow the resulting equations differ in terms of derivatives (the Hiemenz base flow only contains total derivatives with respect to y, whereas the secondary base flow contains partial derivatives in both x and y) and some additional terms related with the secondary base flow.

For the derivation of the stability equations the span-wise gradient of the base flow ($\partial/\partial z(.)$) was neglected due to the assumption of self-similarity. While this holds true for the classical analytical swept Hiemenz boundary-layer flow, it is not the case for the primarily distrubed swept Hiemenz boundary-layer flow. Means of accounting for this are shown in Section 2.3.1 and the consequences of this assumption are discussed in Section 5.1.

The previously derived classical equations [30], [35], [7] for bi-global stability with the exact **swept Hiemenz base flow** without primary disturbances read

$$(\mathscr{L} + V' + \mathrm{i}\gamma\mathrm{Re}c)\left[(\partial_x^2 - \gamma^2)\hat{u} + \partial_x\partial_y\hat{v}\right] + (\mathrm{i}\gamma\mathrm{Re}W'\partial_x - \gamma^2 xV'')\hat{v} = 0 \tag{2.29a}$$

$$(\mathscr{L} - V' + \mathrm{i}\gamma\mathrm{Re}c)\left[(\partial_y^2 - \gamma^2)\hat{v} + \partial_x\partial_y\hat{u}\right] - (\mathrm{i}\gamma\mathrm{Re}W'\partial_x - xV''\partial_x^2)\hat{u} + (\mathrm{i}\gamma\mathrm{Re}W'' + xV''\partial_x\partial_y)\hat{v} = 0 \tag{2.29b}$$

where

$$\mathscr{L} \equiv \partial_x^2 + \partial_y^2 + xV'\partial_x - V\partial_y - \gamma^2 - \mathrm{i}\gamma\mathrm{Re}W$$

and the 'prime' denotes the total derivative w.r.t. y.

The equations for bi-global **secondary** stability derived in the scope of this thesis read

$$(\mathscr{L} + \partial_y V + \mathrm{i}\gamma c)\left[(\partial_x^2 - \gamma^2)\hat{u} + \partial_x\partial_y\hat{v}\right] + (\mathrm{i}\gamma\partial_x^2 W - \partial_x V\partial_x\partial_y)\hat{u} (\partial_x\partial_y W\mathrm{i}\gamma - \partial_y W\partial_x\mathrm{i}\gamma + \partial_x W\partial_y\mathrm{i}\gamma - \partial_x V\partial_y^2 + \gamma^2\partial_y U)\hat{v} = 0 \tag{2.30a}$$

$$(\mathscr{L} - \partial_y V + \mathrm{i}\gamma c)\left[(\partial_y^2 - \gamma^2)\hat{v} + \partial_x\partial_y\hat{u}\right] + (\mathrm{i}\gamma\partial_y^2 W - \partial_y U\partial_x\partial_y)\hat{v} (\partial_x\partial_y W\mathrm{i}\gamma - \partial_y W\partial_x\mathrm{i}\gamma + \partial_x W\partial_y\mathrm{i}\gamma - \partial_y U\partial_x^2 + \gamma^2\partial_x V)\hat{u} = 0 \tag{2.30b}$$

where

$$\mathscr{L} \equiv \Delta/\mathrm{Re} - (U\partial_x + V\partial_y + W\mathrm{i}\gamma), \quad \Delta \equiv \partial_x^2 + \partial_y^2 - \gamma^2.$$

2.4.1. Boundary Conditions

The boundary conditions applied to the equations in the case of validation for the GH eigenmode in Sections 4.1 and 4.2 in conjunction with Equations (2.29a) and (2.29b) were

$$\text{at } x = 0: \quad \text{none}, \tag{2.31a}$$

$$\text{at } x \to L_x: \quad \partial_x^2\hat{u} = \partial_x^2\hat{v} = 0, \tag{2.31b}$$

$$\text{at } y = 0: \quad \hat{u} = \hat{v} = \partial_y\hat{v} = 0, \tag{2.31c}$$

$$\text{at } y \to L_y: \quad \hat{u} = \hat{v} = \partial_y\hat{v} = 0. \tag{2.31d}$$

These boundary conditions have been verified before by Diggelmann [7] and were adopted for verification here.

The boundary conditions applied to the equations in the case of secondary instability eigenmodes in conjunction with Equations (2.30a) and (2.30b) were

$$\text{at } x = 0: \quad \partial_x^2 \hat{u} = 0 \quad \text{or} \quad \hat{u} = 0, \tag{2.32a}$$

$$\text{at } x \to L_x: \quad \hat{u} = \hat{v} = 0, \tag{2.32b}$$

$$\text{at } y = 0: \quad \hat{u} = \hat{v} = \partial_y \hat{v} = 0, \tag{2.32c}$$

$$\text{at } y \to L_y: \quad \hat{u} = \hat{v} = 0. \tag{2.32d}$$

3. Methods

3.1. Numerical Code

The following sections describe important parts of the eigenvalue problem solver. The discussed parts of the code can be found in Appendix D.

3.1.1. Grid

The computational domain is discretized with a structured non-equidistantly meshed grid. The grid points in both x- and y-directions use a Gauss-Lobatto distribution which are defined in the interval $[-1, 1]$ as

$$\xi_j = \cos \frac{j-1}{N_\alpha - 1}, \qquad j = 1, \ldots, N_\alpha. \tag{3.1}$$

Since the physical domain considered in the eigenvalue problem makes use of symmetry, the x- and y-dimensions span a semi-infinite domain. Due to computational limits they nonetheless have to be restricted to finite size. Hence, the grid points ξ_j have to be mapped onto the quasi semi-infinite domain of $x \in [0, L_x]$ and $y \in [0, L_y]$. L_x and L_y must be chosen sufficiently large. The mapping is done with an algebraic mapping of the form

$$\alpha_j = A \frac{1 + \xi_j}{B - \xi_j} \tag{3.2}$$

where

$$B = \frac{L_\alpha}{L_\alpha - 2\alpha_{\text{half}} + \epsilon} \qquad A = B \cdot \alpha_{\text{half}}, \quad \text{with} \quad \alpha = \{x, y\}. \tag{3.3}$$

This way the grid points N_x and N_y are mapped from $\xi_j \in [-1, 1]$ to $[0, L_\alpha]$ in such a way that one half of the points lie within $[0, \alpha_{\text{half}}]$ and the other lie within $(\alpha_{\text{half}}, L_\alpha]$. A and B are related to α_{half} and L_α as follows:

$$L_\alpha = \frac{2A}{B-1}, \qquad \alpha_{\text{half}} = \frac{A}{B}. \tag{3.4}$$

Discretization input parameters of the code are $N_x,\ N_y,\ L_x,\ L_y,\ x_{\text{half}}$ and y_{half} and they fully define the computational domain. Alternatively to the Gauss-Lobato distribution of grid points a uniform distribution can be specified if desired. Three different grid discretizations are shown in Figure 3.1.

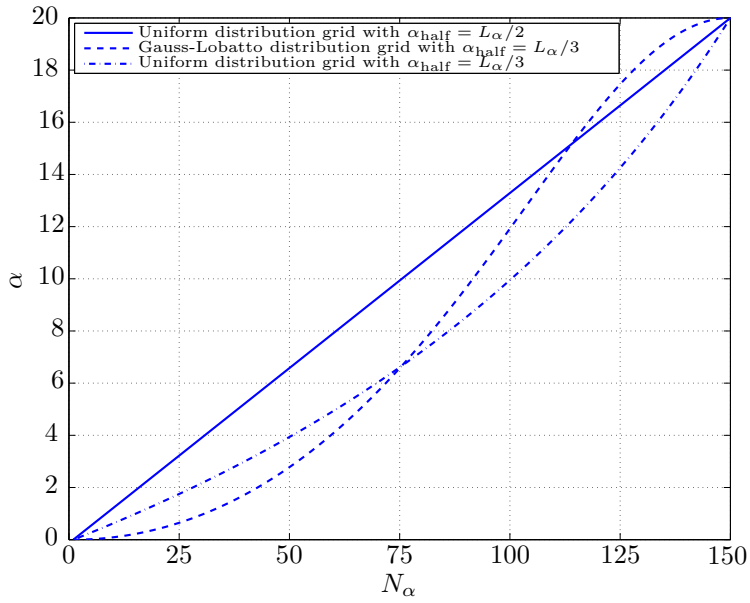

Figure 3.1.: Three different grid discretizations that can be employed. The variable α takes values x or y. Typically uniform distribution grids with different x_{half} were used in x and Gauss-Lobatto distribution grids were used in y.

3.1.2. Numerical Schemes

The code uses a finite-difference type scheme with a five-point stencil with values stored at the grid points (x_j, y_j) of a collocated grid. Differences at the boundaries are computed through a one-sided 4^{th} order stencil (forwards or backwards respectively), for coordinates next to boundary coordinates a mixed forward or backward 4^{th} order stencil is used and for all points within a 4^{th} order central scheme is applied. The code was extended to perform with non-equidistant grid spacing as well as equidistant arrangements.
The discretization can be expressed in a matrix representation to be

$$\mathbf{A} \cdot \mathbf{D}f(x) = f \tag{3.5}$$

where the RHS of Equation (3.5) $f \in \mathbb{R}^{5\times 1}$ represents the known local solution around the coordinate x. $\mathbf{D}f(x) \in \mathbb{R}^{m\times 1}$ defines the wanted local derivations at coordinate x, and it is multiplied from the left with a local stencil matrix $\mathbf{A} \in \mathbb{R}^{5\times m}$ that defines the local Taylor series terms. The differential operators of first and second order for the central grid points are

computed from

$$A_{i,C} = \underset{\text{at } i=3,\ldots,(N-2)}{\begin{pmatrix} 1 & \frac{\Delta_{i-1}}{1!} & \frac{\Delta_{i-1}^2}{2!} & \frac{\Delta_{i-1}^3}{3!} & \frac{\Delta_{i-1}^4}{4!} \\ 1 & \frac{\Delta_i}{1!} & \frac{\Delta_i^2}{2!} & \frac{\Delta_i^3}{3!} & \frac{\Delta_i^4}{4!} \\ 0 & 0 & 0 & 0 & 0 \\ 1 & \frac{\Delta_{i+1}}{1!} & \frac{\Delta_{i+1}^2}{2!} & \frac{\Delta_{i+1}^3}{3!} & \frac{\Delta_{i+1}^4}{4!} \\ 1 & \frac{\Delta_{i+2}}{1!} & \frac{\Delta_{i+2}^2}{2!} & \frac{\Delta_{i+2}^3}{3!} & \frac{\Delta_{i+2}^4}{4!} \end{pmatrix}}. \tag{3.6}$$

where $\Delta_i = x_i - x_{i-1}$. Terms f and $\mathbf{D}f(x)$ will only be be presented here for the central scheme, but can be interpreted for boundary points from the stencil matrices below.

$$\mathbf{D}f(x) := \begin{pmatrix} f(x) \\ f'(x) \\ \vdots \\ f^{(m)}(x) \end{pmatrix} \qquad f := \begin{pmatrix} f(x - \Delta_i - \Delta_{i-1}) \\ f(x - \Delta_i) \\ f(x) \\ f(x + \Delta_{i+1}) \\ f(x + \Delta_{i+1} + \Delta_{i+2}) \end{pmatrix} \tag{3.7}$$

The other differential operators are created from either

$$A_{i,BP} = \underset{\text{at } i=2}{\begin{pmatrix} 1 & \frac{\Delta_i}{1!} & \frac{\Delta_i^2}{2!} & \frac{\Delta_i^3}{3!} & \frac{\Delta_i^4}{4!} \\ 0 & 0 & 0 & 0 & 0 \\ 1 & \frac{\Delta_{i+1}}{1!} & \frac{\Delta_{i+1}^2}{2!} & \frac{\Delta_{i+1}^3}{3!} & \frac{\Delta_{i+1}^4}{4!} \\ 1 & \frac{\Delta_{i+2}}{1!} & \frac{\Delta_{i+2}^2}{2!} & \frac{\Delta_{i+2}^3}{3!} & \frac{\Delta_{i+2}^4}{4!} \\ 1 & \frac{\Delta_{i+3}}{1!} & \frac{\Delta_{i+3}^2}{2!} & \frac{\Delta_{i+3}^3}{3!} & \frac{\Delta_{i+3}^4}{4!} \end{pmatrix}} \quad \text{and} \quad \underset{\text{at } i=N-1}{\begin{pmatrix} 1 & \frac{\Delta_{i-2}}{1!} & \frac{\Delta_{i-2}^2}{2!} & \frac{\Delta_{i-2}^3}{3!} & \frac{\Delta_{i-2}^4}{4!} \\ 1 & \frac{\Delta_{i-1}}{1!} & \frac{\Delta_{i-1}^2}{2!} & \frac{\Delta_{i-1}^3}{3!} & \frac{\Delta_{i-1}^4}{4!} \\ 1 & \frac{\Delta_i}{1!} & \frac{\Delta_i^2}{2!} & \frac{\Delta_i^3}{3!} & \frac{\Delta_i^4}{4!} \\ 0 & 0 & 0 & 0 & 0 \\ 1 & \frac{\Delta_{i+1}}{1!} & \frac{\Delta_{i+1}^2}{2!} & \frac{\Delta_{i+1}^3}{3!} & \frac{\Delta_{i+1}^4}{4!} \end{pmatrix}} \tag{3.8}$$

or

$$A_{i,B} = \underset{\text{at } i=1}{\begin{pmatrix} 0 & 0 & 0 & 0 & 0 \\ 1 & \frac{\Delta_{i+1}}{1!} & \frac{\Delta_{i+1}^2}{2!} & \frac{\Delta_{i+1}^3}{3!} & \frac{\Delta_{i+1}^4}{4!} \\ 1 & \frac{\Delta_{i+2}}{1!} & \frac{\Delta_{i+2}^2}{2!} & \frac{\Delta_{i+2}^3}{3!} & \frac{\Delta_{i+2}^4}{4!} \\ 1 & \frac{\Delta_{i+3}}{1!} & \frac{\Delta_{i+3}^2}{2!} & \frac{\Delta_{i+3}^3}{3!} & \frac{\Delta_{i+3}^4}{4!} \\ 1 & \frac{\Delta_{i+4}}{1!} & \frac{\Delta_{i+4}^2}{2!} & \frac{\Delta_{i+4}^3}{3!} & \frac{\Delta_{i+4}^4}{4!} \end{pmatrix}} \quad \text{and} \quad \underset{\text{at } i=N}{\begin{pmatrix} 1 & \frac{\Delta_{i-3}}{1!} & \frac{\Delta_{i-3}^2}{2!} & \frac{\Delta_{i-3}^3}{3!} & \frac{\Delta_{i-3}^4}{4!} \\ 1 & \frac{\Delta_{i-2}}{1!} & \frac{\Delta_{i-2}^2}{2!} & \frac{\Delta_{i-2}^3}{3!} & \frac{\Delta_{i-2}^4}{4!} \\ 1 & \frac{\Delta_{i-1}}{1!} & \frac{\Delta_{i-1}^2}{2!} & \frac{\Delta_{i-1}^3}{3!} & \frac{\Delta_{i-1}^4}{4!} \\ 1 & \frac{\Delta_i}{1!} & \frac{\Delta_i^2}{2!} & \frac{\Delta_i^3}{3!} & \frac{\Delta_i^4}{4!} \\ 0 & 0 & 0 & 0 & 0 \end{pmatrix}}. \tag{3.9}$$

Since the term of interest is $\mathbf{D}f(x)$, for each grid point x_i, the above matrix A_i is computed and then inverted. After doing so, the local differentiation stencils for first and second derivative

are recovered by storing the second and third rows of A^{-1} in the differentiation operators `Dx1` and `Dx2`, respectively. Higher differentiations are not needed but could be obtained from for example the fourth row etc. of A^{-1} at which point, however, the stencil would optimally have to be broadened to a stencil across more than five points.

3.1.3. Solution Algorithm

The linear stability equations (2.30) are formulated as a generalized eigenvalue problem for the complex EV c,

$$\mathcal{Q}\underline{\phi} = c\mathcal{R}\underline{\phi}, \quad \text{where} \quad \phi = \begin{pmatrix} \underline{\hat{u}} \\ \underline{\hat{v}} \end{pmatrix}. \tag{3.10}$$

More precisely the matrices $\mathcal{Q}$ and $\mathcal{R}$ are $\in \mathbb{C}^{2N_xN_y \times 2N_xN_y}$ and sparse. They have a block structure of 2×2 wherein the submatrices $\mathcal{Q}_{\alpha\alpha}$ and $\mathcal{R}_{\alpha\alpha} \in \mathbb{C}^{N_xN_y \times N_xN_y}$ act either on $\underline{\hat{u}}$ or $\underline{\hat{v}}$:

$$\begin{pmatrix} \mathcal{Q}_{11} & \mathcal{Q}_{12} \\ \mathcal{Q}_{21} & \mathcal{Q}_{22} \end{pmatrix} \begin{pmatrix} \underline{\hat{u}} \\ \underline{\hat{v}} \end{pmatrix} = c \begin{pmatrix} \mathcal{R}_{11} & \mathcal{R}_{12} \\ \mathcal{R}_{21} & \mathcal{R}_{22} \end{pmatrix} \begin{pmatrix} \underline{\hat{u}} \\ \underline{\hat{v}} \end{pmatrix}. \tag{3.11}$$

The individual submatrices follow from (2.30) as

$$\begin{aligned}
&\underbrace{\left[(\mathscr{L} + \partial_y V)\left(\partial_x^2 - \gamma^2\right) + \mathrm{i}\gamma\partial_x^2 W - \partial_x V \partial_x \partial_y\right]}_{\mathrm{i}\gamma\mathcal{Q}_{11}} \hat{u} \\
&+ \underbrace{\left[(\mathscr{L} + \partial_y V)(\partial_x\partial_y) + \partial_x\partial_y W \mathrm{i}\gamma - \partial_y W \partial_x \mathrm{i}\gamma + \partial_x W \partial_y \mathrm{i}\gamma - \partial_x V \partial_y^2 + \gamma^2 \partial_y U\right]}_{\mathrm{i}\gamma\mathcal{Q}_{12}} \hat{v} \\
&\qquad = -\mathrm{i}\gamma c[\underbrace{\left(\partial_x^2 - \gamma^2\right)}_{-\mathcal{R}_{11}} \hat{u} + \underbrace{\partial_x\partial_y}_{-\mathcal{R}_{12}} \hat{v}] \qquad (3.12a) \\
&\underbrace{\left[(\mathscr{L} - \partial_y V)(\partial_x\partial_y) + \partial_x\partial_y W \mathrm{i}\gamma - \partial_y W \partial_x \mathrm{i}\gamma + \partial_x W \partial_y \mathrm{i}\gamma - \partial_y U \partial_x^2 + \gamma^2 \partial_x V\right]}_{\mathrm{i}\gamma\mathcal{Q}_{21}} \hat{u} \\
&+ \underbrace{\left[(\mathscr{L} - \partial_y V)\left(\partial_y^2 - \gamma^2\right) + \mathrm{i}\gamma\partial_y^2 W - \partial_y U \partial_x \partial_y\right]}_{\mathrm{i}\gamma\mathcal{Q}_{22}} \hat{v} \\
&\qquad = -\mathrm{i}\gamma c[\underbrace{\partial_x\partial_y}_{-\mathcal{R}_{21}} \hat{u} + \underbrace{\left(\partial_y^2 - \gamma^2\right)}_{-\mathcal{R}_{22}} \hat{v}] \qquad (3.12b)
\end{aligned}$$

After constructing $\mathcal{Q}$ and $\mathcal{R}$ they are altered to define the boundary conditions as described below in Section 3.1.5. The routine employs the Arnoldi algorithm to solve the eigenvalue problem.

3.1.4. Arnoldi Algorithm[1]

The MATLAB function `eigs` uses the ARPACK package code. The Arnoldi algorithm can be explained based on the following general eigenvalue problem:

$$\mathbf{A}\underline{x} = \lambda\mathbf{M}\underline{x}. \tag{3.13}$$

Two parameters have to be specified when starting the *Arnoldi-algorithm*. The first parameter m specifies the number of eigenvalues that are to be resolved and ultimately also is responsible for the convergence of the algorithm. The second parameter σ is an initial eigenvalue that the algorithm takes as a seed around which to compute the other eigenvalues. The basic idea of the Algorithm is to project the matrix $\mathbf{A}$ onto the orthonormal basis of the *Krylov* sub-space $\mathcal{K}_m$ that is constructed from an initially random vector v_1, thereby creating a Hessenberg matrix $\mathbf{H}_m$ whose eigenvalues (Ritz EV) are the approximate eigenvalues of the original eigenvalue problem matrix $\mathbf{A}$. The Algorithm first does a shift-and-invert operation which transforms Equation (3.13) into

$$\mathbf{S}\underline{x} = \mu\underline{x}, \qquad \mathbf{S} = (\mathbf{A} - \sigma\mathbf{M})^{-1}\mathbf{A}\underline{x}, \qquad \mu = \frac{1}{\lambda - \sigma}. \tag{3.14}$$

With the reformulated eigenvalue problem the algorithm goes as:

1. Start with an arbitrary vector v_1 with $||v_1|| \equiv 1$.
2. for $j = 1, \ldots, m$ do:

$$\begin{aligned} h_{ij} &= (\mathbf{S}v_i, v_j), \qquad i = 1, \ldots, j \\ w_j &= \mathbf{S}v_j - \sum_{i=1}^{j} h_{ij}v_i \\ h_{j+1,j} &= ||w_j|| \\ v_{j+1} &= w_j / h_{j+1,j} \end{aligned}$$

The resulting m Arnoldi vectors v_i span the orthonormal basis $\mathbf{W}_m$ of the Krylov sub-space

$$\mathcal{K}_m = \text{span}\left\{v_1, \mathbf{S}v_1, \ldots, \mathbf{S}^{m-1}v_1\right\}.$$

The algorithm computes a factorization of type

$$\mathbf{S}\mathbf{W}_m = \mathbf{W}_m\mathbf{H}_m + h_{m+1,m}v_{m+1}e_m^* \tag{3.15}$$

$$\mathbf{W}_m^*\mathbf{S}\mathbf{W}_m = \mathbf{H}_m. \tag{3.16}$$

The original matrix $\mathbf{S}$, or $\mathbf{A}$ respecively, of size $\mathbb{R}^{m\times m}$ in in this process reduced to the Hessenberg matrix $\mathbf{H}_m$ of size $\mathbb{R}^{n\times n}$ with $n < m$. The problem is thus reduced in size and the approximate eigenvalues are regained from the eigenvalues ϑ (Ritz values) of the Hessenberg matrix. The eigenvectors are obtained through an inverse iteration from the eigenvector $\underline{s}$ of the Hessenberg

[1] The information in this section is a summary based on [1], [7] and [39]

matrix. The respective Ritz eigenvector is obtained through $\underline{y} = \mathbf{W}_m \underline{s}$. The approximate eigenvector of the eigenvalue problem (3.13) is recovered as

$$\mathbf{S}\underline{y} = \mathbf{W}_m \mathbf{H}_m \underline{s} + \underbrace{h_{m+1,m} v_{m+1}}_{r_m} e_m^* \underline{s} = \underline{y}\theta + r_m e_m^* \underline{s}. \tag{3.17}$$

3.1.5. Implementation of Boundary Conditions

The boundary conditions are implemented into the eigenvalue Matrices $\mathcal{Q}$ and $\mathcal{R}$, which are both *sparse*. Element-wise accessing of the elements therefore is very slow, since for every zero-element that is made non-zero in that occasion or for every non-zero-element that is made zero the indices of all subsequent non-zero entries have to be shifted to account for the new entry. This procedure is a significant bottleneck when considering speed.
To overcome this limitation, the boundary conditions were incorporated into the *full* sub-matrices. Instead of accessing each element individually, two stencil matrices were assembled, one for multiplication (essentially creating zero-entries) and one for superposition of non-zero elements (Figure 3.2). Thanks to the block-wise structure of the operator matrices, the routine for assembling the stencil matrices only needs two calls in total. This method gave the code a noticeable speed-up. Ideally, a further speed-up could be realized using pointer arithmetics, which, however, is not possible in the current MATLAB environment.

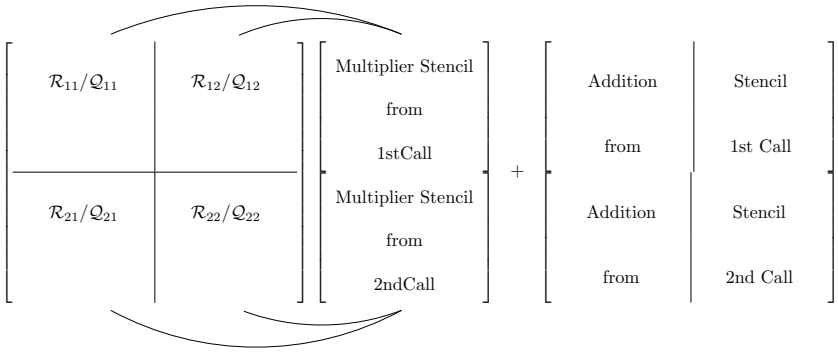

Figure 3.2.: The two stencil matrices used to impose the BCs on $\mathcal{Q}$ and $\mathcal{R}$. Two calls are necessary, one of which constructs stencils for coordinate x and the other for coordinate y.

3.2. Evaluation

3.2.1. Numerical Convergence Criterion

As a first goal, the numerical convergence of the eigenvalue solver was characterized and the numerical error quantified. As there is no exact solution to which the numerical result can be compared, the error ε was considered the absolute difference of the complex eigenvalues in the

spectrum:

$$\varepsilon = \sqrt{\frac{|EV_i - EV_{i+1}|^2}{N_{x,i} \cdot N_{y,i}}} \tag{3.18}$$

with i indicating a certain resolution and $i+1$ the next greater. The reason this criterion was chosen over comparing the eigenfunctions is the ability to study convergence without the need of interpolation and thereby potentially altering the convergence behavior.

3.2.2. Mode Filtering

The numerical solver returns the specified number of eigenvalues and their corresponding eigenfunctions. For easier and more efficient post-processing a filter was implemented to help identify or track eigenvalues throughout the eigenvalue spectra. For analysing the numerical convergence for example it was assumed that EVs of the same mode would stand out in the spectra by having moved only little. Other modes that may have arisen by numerics only with no physical relevance would not behave in the same way. In other words, all physically relevant and realistic Modes would only weakly if at all be dependent on numerical parameters. The same was assumed to be applicable to variations of physical parameters. As an example tracking of a mode through a sweep over the spanwise wavenumber γ is desirable. Instead of manually extracting the corresponding solutions from the spectrum at each parameter step, all spectra should be fed to a processing algorithm and the matching values returned. For the sake of this, two algorithms were implemented. One of them essentially a 'deterministic dynamic programming shortest path algorithm' and the other an algorithm that searches for local minimal differences.

DP algorithm

This algorithm is fed with the spectra of all parametric steps. Subsequently a cost matrix is computed. The cost to go from node i to node j at stage k is specified as the absolute value of the difference between node j at stage $k+1$ and node i at stage k. Nodes in this context describe eigenvalues and the stages are the steps of the parametric sweeps:

$$\text{cost2go}_{ij}^{k} = |\text{EV}_j^{k+1} - \text{EV}_i^{k}|. \tag{3.19}$$

The cost was then calculated as

$$J_i^k = \min_j \{J_j^{k+1} + \text{cost2go}_{ij}^{k}\}. \tag{3.20}$$

The paths were tracked and sorted with ascending cost.

Local Minumum Algorithm

Two ways of calculating the cost can be chosen, the reason being the different filtered spectra. For eigenvalues that would follow a path upon undergoing a parametric sweep a *static cost*

matrix was precomputed that stored the cost from each eigenvalue at one parameter step to every eigenvalue at the next parameter step (according to Equation (3.19)). The cost of going from the last step $k = N$ to step k was in this case always locally complemented with the local minimal cost-to-go:

$$J_i^k = J_j^{k+1} + \min_i\{\text{cost2go}_{ij}^k\}. \tag{3.21}$$

This algorithm is somewhat simpler but for not very cluttered spectra it is also faster. However, both Algorithms (3.20) and (3.21) have the disadvantage of equally punishing the drift of an eigenvalue in any direction. So for eigenvalues that would cluster around a certain value the cost was implemented to be *dynamically computed* with respect to a center of mass (CoM), which again would be recomputed once the next path step was found. This would punish the cost more if the algorithm would drift far away from the actual eigenvalue, given of course an already large enough weight of the CoM. At step $k = N$ the CoM is simply an eigenvalue of the N-th spectrum

$$\text{CoM}_i^N = \text{EV}_i^N. \tag{3.22}$$

For all other steps the CoM is

$$\text{CoM}_i^k = (\text{CoM}_j^{k+1} \cdot (N - k - 1) + \text{EV}_i^{k+1})/(N - k) \tag{3.23}$$

and the cost is computed as

$$J_i^k = J_j^{k+1} + \min_i\{|\text{CoM}_j^{k+1} - \text{EV}_i^k|\}, \tag{3.24}$$

where

$$k = N - 1, \ldots, 1. \tag{3.25}$$

Again the paths were tracked in both cases and accordingly sorted with ascending cost.

4. Validation, Characterization and Convergence

4.1. Grid Discretization

The altered code was tested for correctness by validating it with the Görtler-Hämmerlin mode from the analytical swept Hiemenz base flow. The reference value that was used can be found in Lin and Malik [26]. The corrected discretization and differentiation schemes for a non-equidistant mesh in x and y directions were shown to be valid since the EV of the GH mode now is practically independent of the resolution in the x direction N_x. Figure 4.1 shows the dependence of c_{GH} on the grid resolution. The values are also summarized in Table 4.1 together with the reference c_{GH} from Lin and Malik.

Moreover, it was made certain that the derived equations yielded the correct Results for the GH eigenmode at the linearly critical stable Reynolds number $\mathrm{Re}_{\mathrm{lin,crit}} = 583.1$ when supplied with the corresponding base flow.

4.2. Memory Requirement and CPU Time

In order to gain insight into the computational effort that arises from the solution of the stability problem the code was run at several grid resolutions where $N = N_x = N_y$ following Pascal Diggelmanns [7] approach to solving for the GH mode. As a means to control the memory allocated during runtime, up to eight different reoccurring terms of Equation (3.12) were either stored as separate variables in memory to reduce runtime or recomputed every time their values were needed to reduce memory. The code was then run for each resolution first with all variables locally computed and then the first variable in Table (4.2) globally saved. Step by step variables were added to the memory while runtime and memory requirement was monitored. The resulting plot is shown in Figure (4.2).

This analysis was done using the analytical base flow where it was known that square resolution would yield a physically correct result and the number of eigenvalues computed[1] was constantly kept equal to 10. The information obtained would serve as further resource for estimating the computational time and memory requirement when running the code on different computation clusters. As can be seen, memory requirement is proportional to N^4 as was expected, since the eigenvalue problem matrices are $\in \mathbb{R}^{2NN \times 2NN}$. In fact, memory requirement is effectively $\propto (N^4 \cdot \{\text{No. of eigenvalues}\})$.

[1] variable `nom`

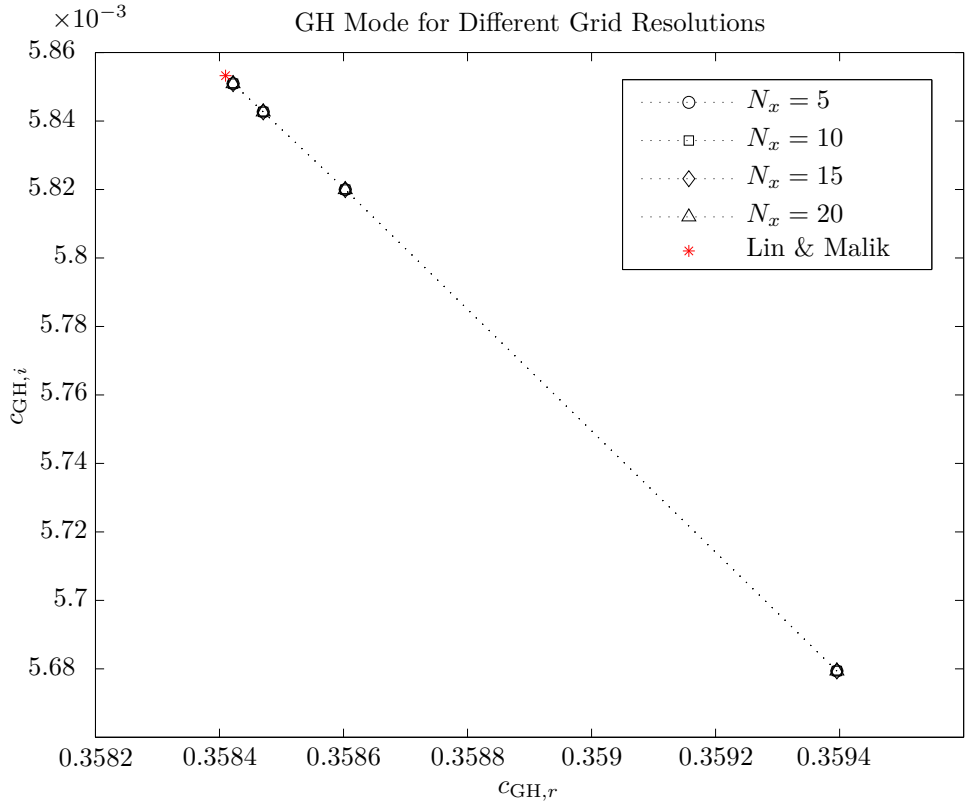

Figure 4.1.: Dependence of the GH mode on grid resolution. N_y is varied from 40, 60, 80 to 120 (right-to-left). The values were obtained for $Re = 800$, $\gamma = 0.255$, $L_x = 120$, $L_y = 70$, $x_{half} = 60.8$ and $y_{half} = 0.5$.

Table 4.1.: GH eigenvalues for different grid resolutions to eight significant digits. It can be seen that for a given y-resolution the problem has converged already for 5 x-gridpoints. For $N_y = 120$ the phase speed has come within four digits and c_i within five digits to the value of Lin and Malik [26].

N_y	40	60	80	120
N_x	c_{GH}	c_{GH}	c_{GH}	c_{GH}
5	0.35939555 +0.00567938i	0.35860279 +0.00581997i	0.35847051 +0.00584266i	0.35842190 +0.00585092i
10	0.35939555 +0.00567938i	0.35860279 +0.00581997i	0.35847051 +0.00584266i	0.35842190 +0.00585092i
15	0.35939555 +0.00567938i	0.35860279 +0.00581997i	0.35847051 +0.00584266i	0.35842190 +0.00585092i
20	0.35939555 +0.00567938i	0.35860279 +0.00581997i	0.35847051 +0.00584266i	0.35842190 +0.00585092i
L&M	0.35840982 + 0.00585325i			

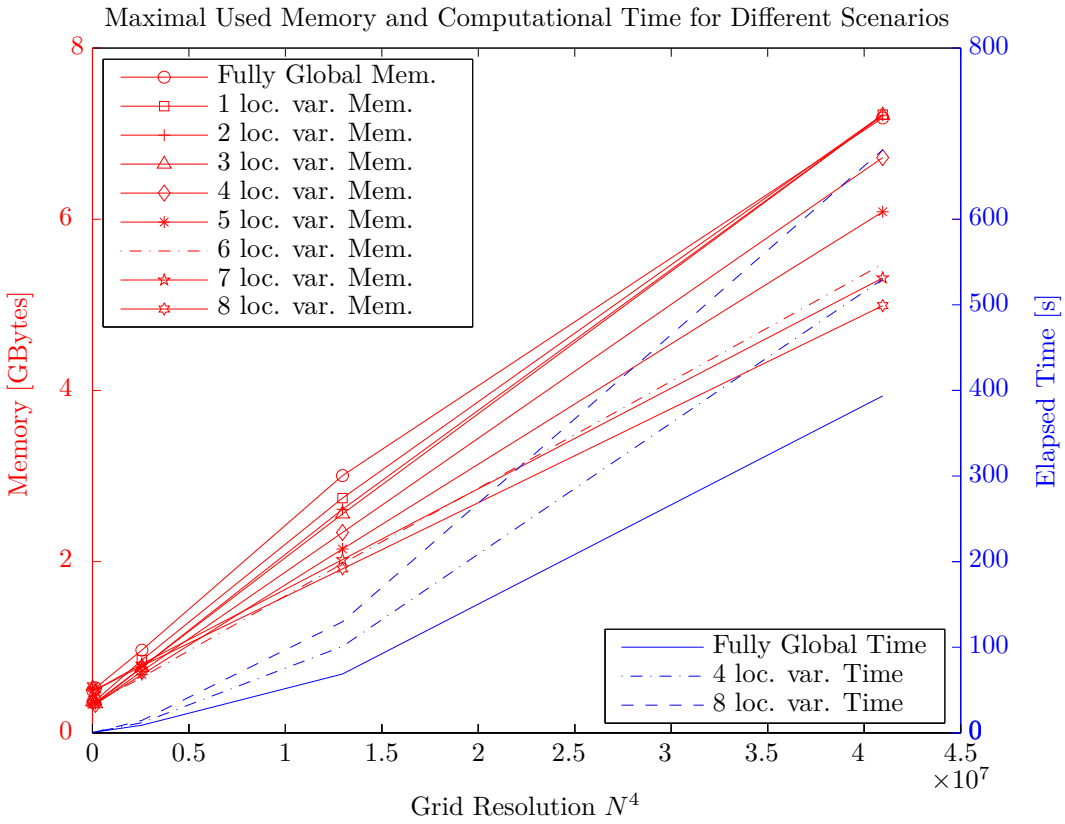

Figure 4.2.: Memory requirement and CPU time

Table 4.2.: Different variable configurations that were utilized for memory and CPU testing of the eigenvalue solver. For subsequent configurations in this table the globally computed variables from the previous configurations are adopted and the newly listed variable is added to the selection.

Configuration	Separately Stored Variables
8 local variables	–
7 local variables	`Laplacex`
6 local variables	`Laplacey`
5 local variables	`Lop`
4 local variables	`LopPlusVy`
3 local variables	`LopMinuVy`
2 local variables	`WyD_Dx`
1 local variable	`xVyy/WxD_Dy`
Fully Global	`Dx1Dy1`

4.3. Convergence Study

This section shows the convergence behavior of the eigenvalue solver for the secondary instability of the swept Hiemenz boundary layer as a function of the number of grid points N_x and N_y of the x and y coordinate, respectively, and the influence of the domain size parameter L_x. Once the numerical part is understood, a conclusion is drawn from the presented data regarding optimal resolution.

The simulations that are presented below were, unless otherwise noted, conducted on a domain of size $L_x = L_y = 15$. The grid was chosen to be linear in x and mapped according to Section 3.1.1 in y with a $y_{\text{half}} = L_y/3 = 5$. The resolutions N_x and N_y are first treated independently, and convergence is sought individually in each direction. This analysis is followed by a study in which the influence of the resolutions' convergence behavior on each other is examined and limitations of the grid are discussed. Sections 4.3.1 and 4.3.2 employed a base flow of resolution $N_{x,b} = 193 \times N_{y,b} = 129 \times N_{z,b} = 513$ for a domain size of $L_{x,b} \in [-15, 15] \times L_{y,b} \in [0, 20] \times L_{z,b} \in [0, 120]$ without secondary amplitude ($A_2 = 0$), Section 4.3.3 employs a base flow of resolution $N_{x,b} = 1025 \times N_{y,b} = 129 \times N_{z,b} = 2049$ for a domain size of $L_{x,b} \in [-150, 150] \times L_{y,b} \in [0, 20] \times L_{z,b} \in [0, 600]$ with secondary amplitude ($A_2 \neq 0$).

4.3.1. N_x Resolution

Convergence in x-direction was investigated by fixing $N_y = 50$ and raising N_x from 40 in steps of 10 to a maximum of 300. Although, the y coordinate is likely to be under-resolved in this scenario as demonstrated in Section 4.3.2, it was kept at this low value. The convergence was described according to Equation (3.18) and is shown in Figure 4.3(a). The convergence was checked for different Reynolds number base flows, each with primary vortices and no secondary amplitude. In each case the base flow resolution was of $N_{x,b} = 193 \times N_{y,b} = 129 \times N_{z,b} = 513$. The flow was respectively extracted from the DNS data at the location of minimal $\partial W_B / \partial z$. Figure 4.3(a) shows the error of convergence for the same eigenmode shape that was recovered at each Reynolds number. It corresponds to eigenmode **S3** introduced in Section 5.2.1. The eigenvalues' individual trace in the complex plane for the different resolutions is shown in Figure 4.3(b). It is apparent that there is a certain optimal N_x above which the solution starts to diverge. In this case convergence is continuous within $120 < N_x < 200$ (marked in grey in Figure 4.3(a)).

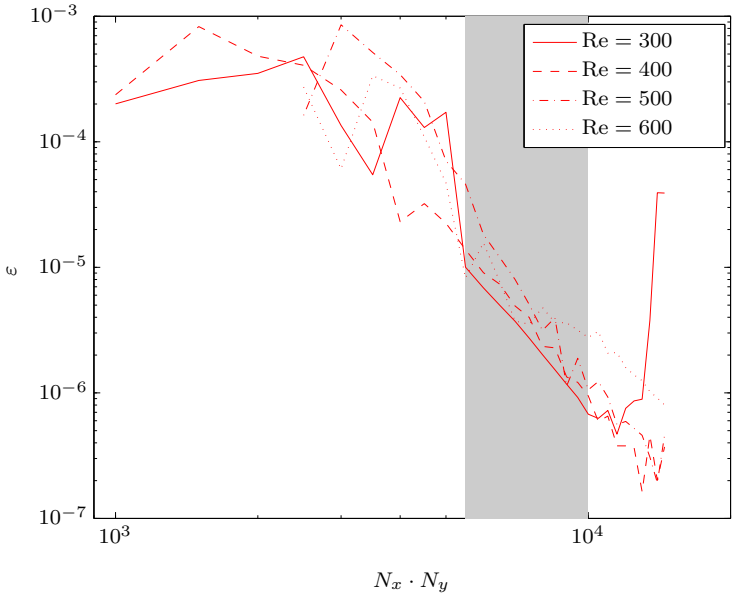

(a) Convergence Error. N_x has an optimum close to $N_x = 200$.

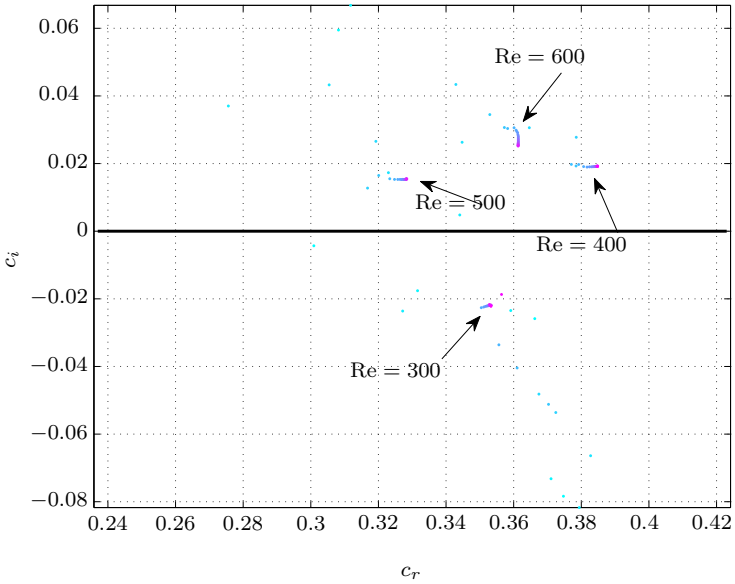

(b) Spectrum. Eigenvalues **S3** travel from cyan (low resolution) to magenta (high resolution)

Figure 4.3.: N_x Convergence. Simulations for Re $= \{300, 400, 500, 600\}$ were performed for wave numbers $\gamma = \{0.4, 0.6, 0.7, 0.8\}$, respectively.

4.3.2. N_y Resolution

The convergence in y-direction was investigated analogously to that in x-direction (Section 4.3.1). N_x was fixed equal to 80 while Ny was varied from 40 to 250 in steps of 10. Again, x is assumed to be underresolved, however in this case the limiting factor was available memory. This issue is addressed later in Section 4.3.3. The base flow extraction locations correspond to those used in Section 4.3.1. Figure 4.4(a) clearly shows a different behaviour than that in x-direction. There seems to be no optimum. The solution converges continuously to some fixed value.

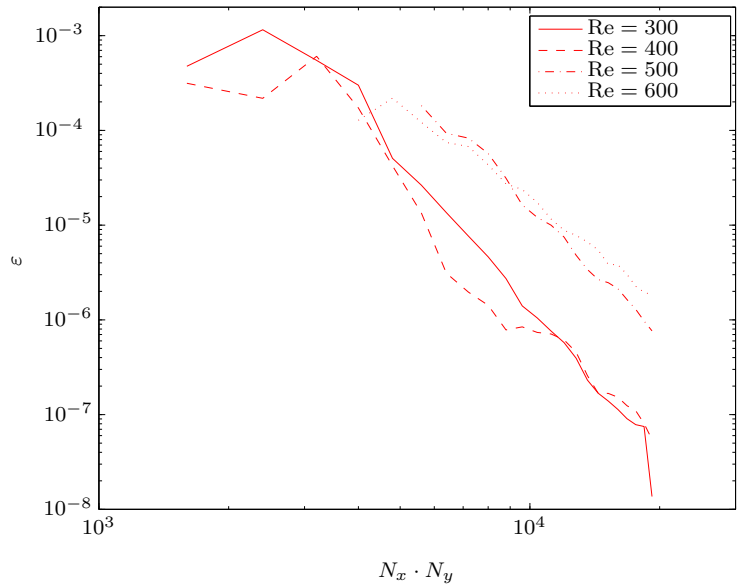

(a) Convergence Error. Raising N_y monotonically makes the solution converge.

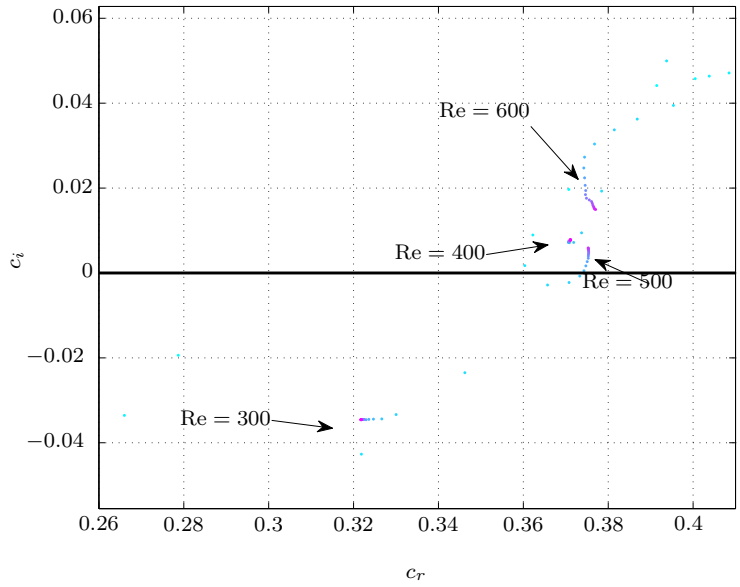

(b) Spectrum. Eigenvalues **S3** travel from cyan (low resolution) to magenta (high resolution)

Figure 4.4.: N_y Convergence. Simulations for Re $= \{300, 400, 500, 600\}$ were performed for wave numbers $\gamma = \{0.4, 0.6, 0.7, 0.8\}$, respectively.

4.3.3. Optimal Resolution and Limitations

Since the studies conducted above always had the issue of one under-resolved dimension another approach was taken for analysing the influence of resolution on the solution. The goal was to alternately raise N_x and N_y and thereby acquire an optimal resolution dependent on both coordinate dimensions that could account for cross-influence of the Resolutions. In order to do so, the resolution was altered as summarized in Table 4.3. The results were evaluated

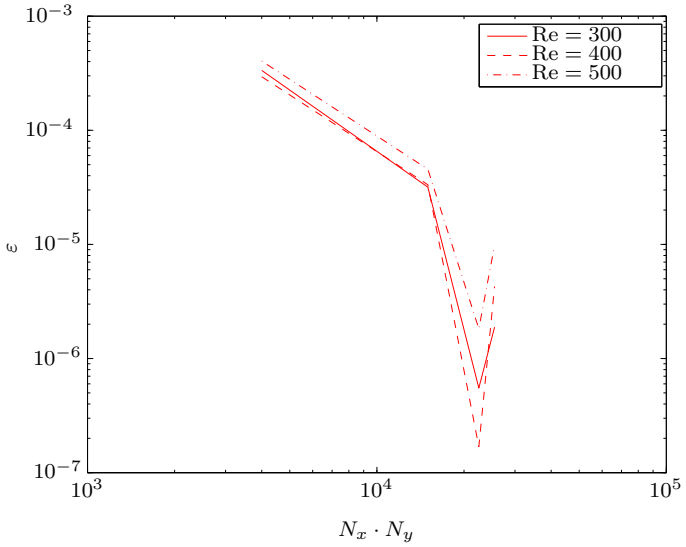

Figure 4.5.: Convergence error resulting from alternatively raising resolutions in x and y as listed in Table 4.3. Simulations for Re = 300, Re = 400 and Re = 500 were performed for wave numbers $\gamma = 0.4$, $\gamma = 0.6$ and $\gamma = 0.7$, respectively. The reason being preliminary findings that suggested maximal growth rates lie around there.

by recording the convergence error (Equation (3.18)), shown in Figure 4.5 and by looking at the eigenfunctions' shapes shown in Figure 4.6. Based on these findings, it was decided that a resolution of $N_x = N_y = 150$ provided a satisfactory number of grid points. Limitations of the code are thus related to available memory. Computational time had already been reduced as far as possible as mentioned in Section 4.2. By extrapolating the data acquired in Figure 4.2 this

Table 4.3.: Different resolutions used to find optimum.

	N_x	N_y
A	80	50
B	100	150
C	150	150
D	150	170
E	170	170

Table 4.4.: Performance capacities of clusters on which the code was run. The possible resolutions with respect to their memory limits are also listed. Resolutions marked green were chosen for computation.

Cluster	VENANT		EIGER	
Maximum total memory for one node	64 GB		46 GB	
	N_x	N_y	N_x	N_y
	200	100	196	90
	182	110	176	100
Possible resolutions	167	120	160	110
	154	130	147	120
	143	140	135	130

optimal resolution was estimated to take up between 62-87 GB of peak Memory depending on the variable configuration (see Table 4.2). Clusters were searched that provided sufficient memory. The computational clusters VENANT[2] and EIGER[3] were chosen to run variable configuration '*5 local variables*' (for trade-off between time and memory) on a resolution of $N_x = 154 \times N_y = 130$ and $N_x = 147 \times N_y = 120$, respectively. Their capacities and other possible resolutions are summarized in Table 4.4.

[2]VENANT is a Rocks Cluster at IFD with three processor nodes, one of which is reserved for graphical jobs and features a GPU. Each of the other two contain 16 2.3GHz processors that have access to 64GB of RAM.

[3]EIGER is a DALCO SUPERMICRO cluster at CSCS. Among others it houses 8 visualization nodes with NVIDIA GeForce 285 GTX cards with 48GB of memory (46GB available). Source: cscs.ch.

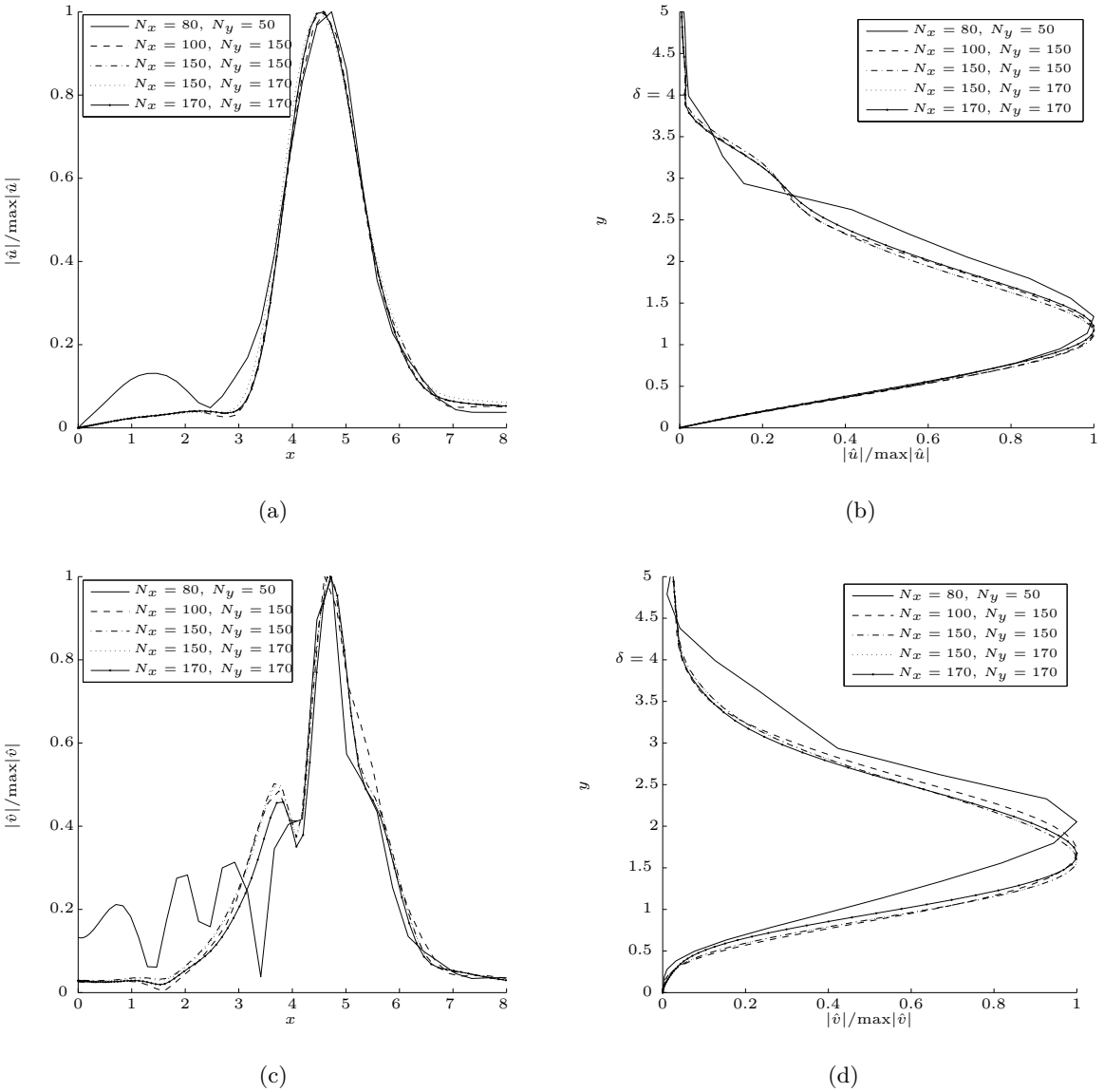

Figure 4.6.: Eigenfunction **S3**'s shapes for different resolutions at $\gamma = 0.4$, Re= 300, $L_x = L_y = 15$, $x_{\text{half}} = L_x/2$, $y_{\text{half}} = L_y/3$.

4.3.4. Domain Size L_x

The physical domain in the above sections of size $L_x = L_y = 15$ was extended in x to see the effect on the physical solutions. The results are shown in Figures 4.7 and 4.8 for all of the three disturbance velocity components $\hat{u}$, $\hat{v}$ and $\hat{w}$. It can be noted that the physical shape of the modes changes very little with varying L_x. Minor differences can be made out where the velocities' gradients are higher, for example where $\hat{u}$ shows a dip in amplitude around $x = 8$ or similarly so for $\hat{v}$ around $x = 6$ and $\hat{w}$ around $x = 4$. For too large L_x those features seem to be smoothed out. This is explained by the fact that while the parameter L_x was varied in this study, the resolution N_x was kept constantly equal to 147. So for larger L_x the ratio $\frac{N_x}{L_x}$ shrinks to a point where the local resolution is not sufficient to fully resolve the finest features. On the other hand, for too small L_x the applied boundary conditions seem to un-physically force the velocities to zero. In fact, the exponential decay is only really apparent for $L_x > 19$. The location of the eigenmodes in the spectrum did not change drastically, either. On the contrary, they seem to be well converged. Their numerical values are summarized in Table 4.5. The values seem to

Table 4.5.: Eigenvalues for different values of L_x for eight significant digits.

L_x	Mode **S1**	Mode **S2**
15	0.74955172 + 0.06021929	0.81543129 + 0.05336194
17	0.74930831 + 0.06009775	0.81544776 + 0.05334418
19	0.74926418 + 0.06007544	0.81545401 + 0.05334090
21	0.74925444 + 0.06007146	0.81545847 + 0.05333933
23	0.74925694 + 0.06007052	0.81546520 + 0.05333938
25	0.74925152 + 0.06006935	0.81547161 + 0.05333684

agree for four digits after the decimal point, with the exception of the values at $L_x = 15$ where the boundary condition forcing is probably responsible for the higher deviation. Based on these findings, for further simulations it was decided to employ a domain size of $L_x = 20 \times L_y = 15$ in order to guarantee a more natural decay over x but still not risk to set the ratio $\frac{N_x}{L_x}$ too low. This was combined with changing x_{half} to $L_x/3$ in order to provide enough grid points around the base flow vortex that the eigenmodes lie around.

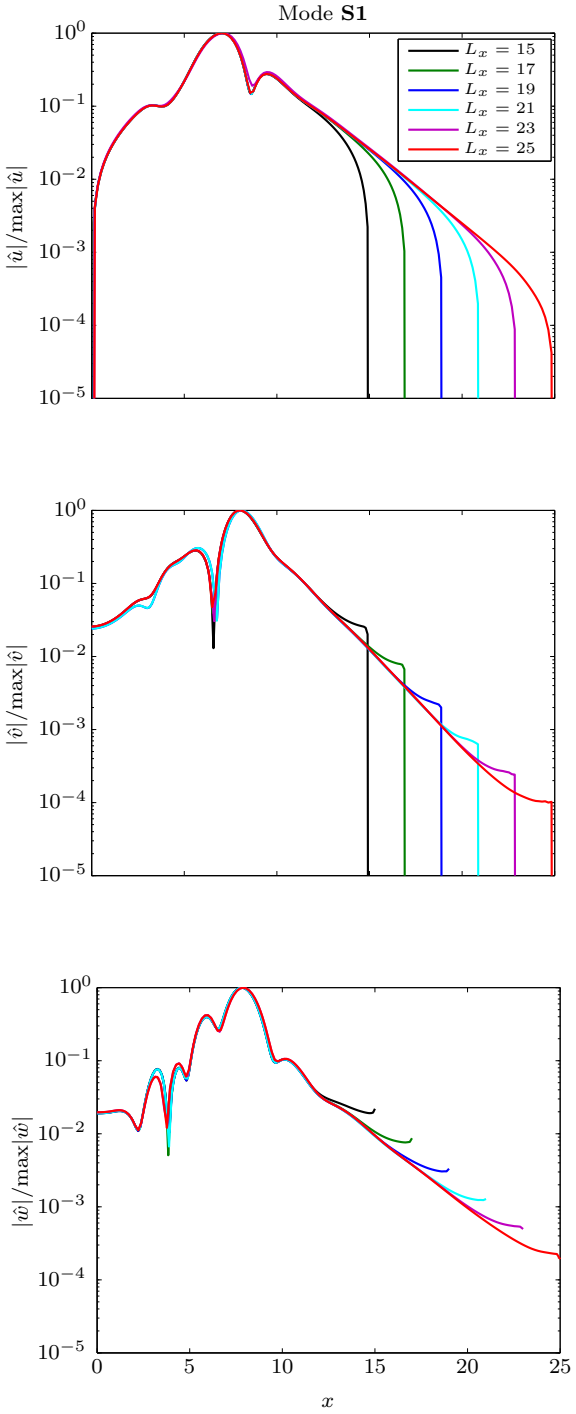

Figure 4.7.: Eigenfunctions of mode **S1** for different L_x, with Re$= 300$, $\gamma = 0.4$, $L_y = 15$, $N_x = 147$, $N_y = 120$, $x_{\text{half}} = L_x/2$, $y_{\text{half}} = L_y/3$, $\Psi = \Psi_U$, $\hat{u}(x = 0, y) = 0$.

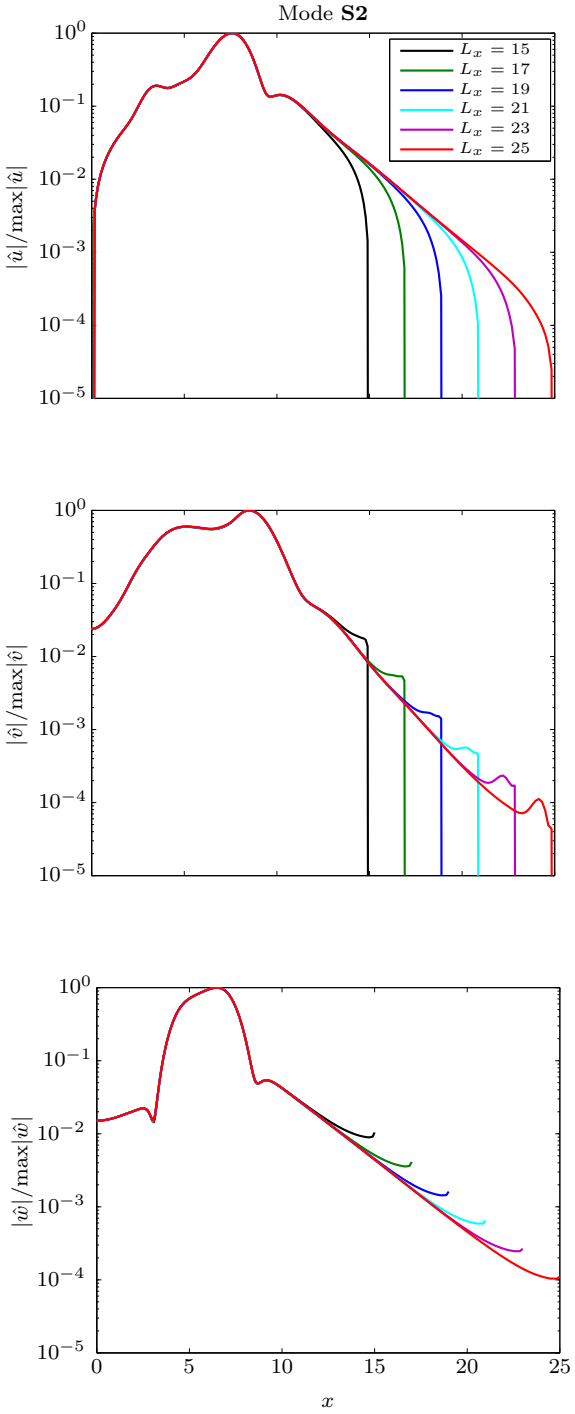

Figure 4.8.: Eigenfunctions of mode **S2** for different L_x, with Re= 300, $\gamma = 0.4$, $L_y = 15$, $N_x = 147$, $N_y = 120$, $x_{\text{half}} = L_x/2$, $y_{\text{half}} = L_y/3$, $\Psi = \Psi_U$, $\hat{u}(x = 0, y) = 0$.

5. Results

In this chapter the obtained results are presented, i.e the eigenmodes of the secondary instability are depicted. The base flow employed in solving the problem features counterrotating vortices as primary disturbances that lead to the formation of streamwise streaks with a superimposed secondary temporally fluctuating amplitude to cause modal disturbance growth.

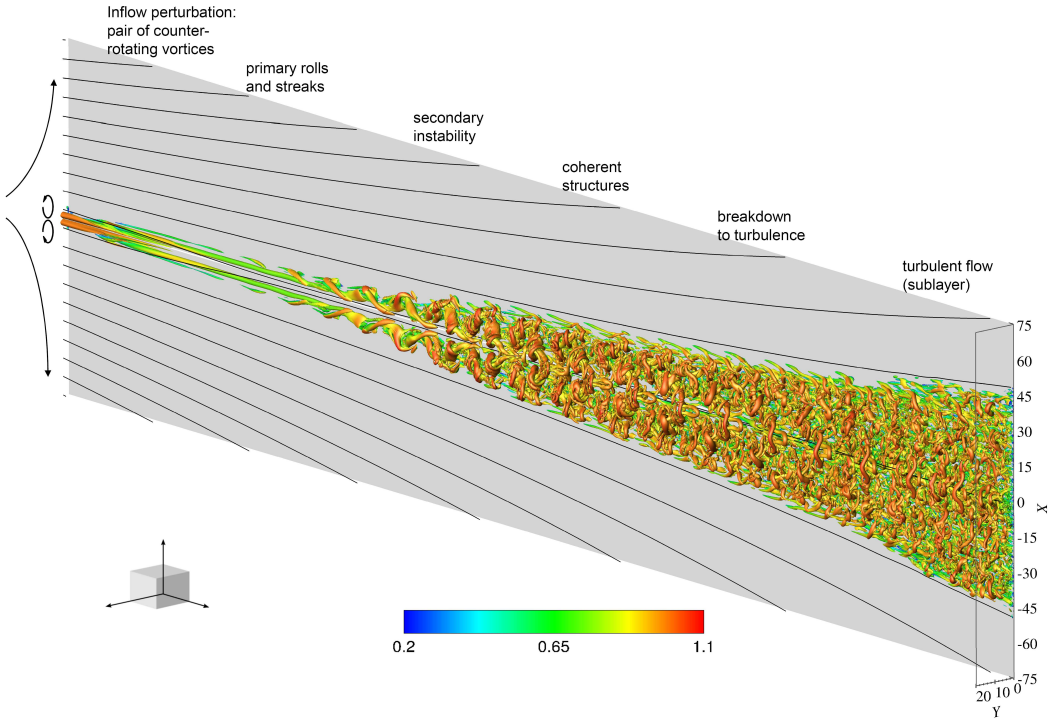

Figure 5.1.: Flow field obtained from DNS. This figure neatly illustrates the flow evolution from the primary vortices to streak formation to secondary modal growth and finally to turbulence breakdown. [22]

For the sake of providing a clear picture, this section is subdivided into five parts. Section 5.1 shows the influence of the base flow modification with the streamfunction Ψ explained in Section 2.3.1. It qualitatively and quantitatively assesses the errors stemming from that artificial operation on the base flow. Section 5.2 shows the complex discrete eigenvalue spectrum and outlines the characteristics of the individual solutions. It summarizes the results from a more distant, broader view. Section 5.3 reports the eigenmodes more in-depth, detailing their unique

features and pointing out their main attributes but also the limiting factors of the analysis. Both Sections 5.2 and 5.3 will lay down the dependencies of the solutions on various physical quantities, such as

- the streamfunction Ψ,
- the wavenumber γ,
- the BCs for $\hat{u}(x = 0, y)$,
- the extraction location z_{extr}.

In Section 5.4, the eigenmodes are presented in a three-dimensional illustration. Eventually, in the last part in Section 5.5 a comparison is presented with the results of a 2002 dissertation by Wintergerste [39].

5.1. Base Flow Discrepancy

As mentioned in Sections and 2.4, the stability equations (3.12) are derived under the assumption of a self-similar flow along the attachment line independent of the span-wise downstream coordinate z. However, it is also mentioned in Section 2.3.1 that the base flow obtained from DNS does not fulfill this assumption. For the solution of the eigenvalue problem (3.10) there are thus two possibilities of of coping with this conflict:

A) neglect the small dependence of the base flow in z, utilizing the fact that the flow is extracted at a location with locally minimal dependence on z (according to Equation (2.22)). This solution thus describes one of a "weakly non-parallel" assumption and is referred to as being 'unrelaxed',

B) modify the base flow according to Equations (2.25) and (2.26) with a weight $\chi \in [0, 1]$. This solution with the modified base flow is referred to as being 'relaxed'.

The resulting divergence according to Equation (2.22) is displayed for case A) and different types of case B) in Table 5.1. Essentially, it can not be said that either one of these alternatives is the 'correct' one. It is shown later, however, that the qualitative results are obtained independent of the choice of the procedure.

Table 5.1.: Divergence of relaxed and unrelaxed base flow

	Streamfunction			
Location	Ψ_U	Ψ_{UV}	Ψ_V	unrelaxed
$z = 94$	2.2732e-15	2.2834e-15	2.2312e-15	3.2779e-05
$z = 159$	2.2763e-15	2.2693e-15	2.3057e-15	2.9660e-05

From the results that are presented in the subsequent sections, it can be said that there is usually nonetheless a small visible effect on the solutions of the eigenvalue problem when the base flow

is relaxed so as to conform to the two-dimensional continuity equation. It is also apparent, however, that there sometimes is a noticeable discrepancy in the respective results and that the unrelaxed solution best agrees with the solution of a relaxation weight of $\chi = 1$ ($\Psi = \Psi_U$). This Section thus tries to shed some light into why there is such disagreement between the individual outcomes. For this purpose, the relative local errors of the base flow components U and V (W remains unchanged) were calculated. Obviously, errors are greatest when a velocity is derived from the streamfunction of its counterpart, i.e. U from Ψ_V or V from Ψ_U. These errors are graphically illustrated in logarithmic contour plots in Figure 5.2. For a better comparison of

Table 5.2.: Quantitative local error integrals that result from forcing the base flow to satisfy the two-dimensional continuity equation. The values are obtained by integrating the local relative errors over x and y.

	Streamfunction			
Velocity component	Ψ_U	Ψ_{UV}	Ψ_V	unrelaxed
$(U_{unrel} - U_{rel})/U_{unrel}$	6.793112e-04	2.926029e02	5.852064e02	—
$(V_{unrel} - V_{rel})/V_{unrel}$	4.055024e-01	2.024120e-01	2.593498e-03	—

the created errors, the relative local errors were integrated over the $x - y$-plane and tabulated in Table 5.2. It was noticed that U is affected much stronger by a derivation from Ψ_V than V is from Ψ_U. In fact, the error is around 1500 times greater. This fact combined with the actual locations of the highest absolute values of the errors (the top plot in Figure 5.2 shows that there is a significant error concentration right along the boundary layer edge and within the boundary layer itself) most probably is the reason for the inconsistency.

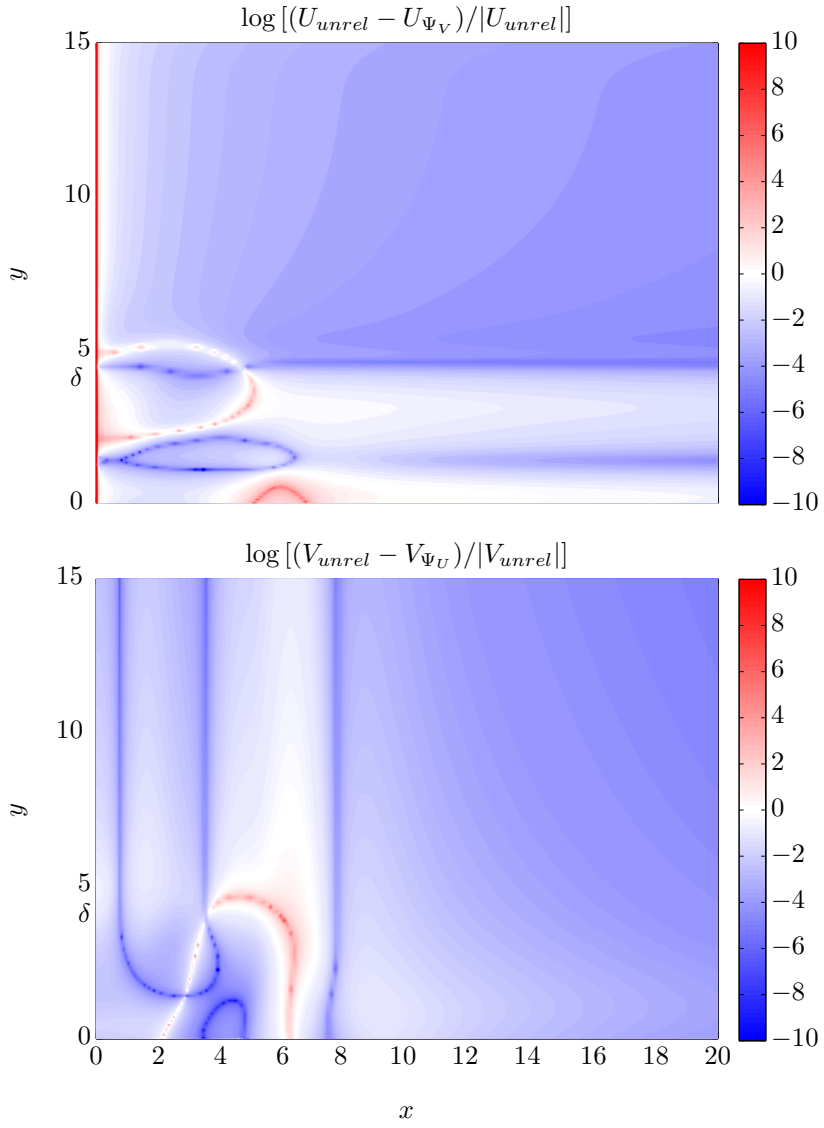

Figure 5.2.: Relative local errors in the base flow at $z_{extr} = 94$ resulting from making the 3D base flow divergence-free in two dimensions. Here the two largest errors are shown. The top shows the local error relative to a non-relaxed BF for the component U when it is relaxed with the streamfunction Ψ_V of the component V. The bottom shows the local error relative to a non-relaxed BF for the component V when it is relaxed with the streamfunction Ψ_U of the component U. The plot is logarithmically presented and the color bars feature orders of magnitude.

5.2. The Discrete Spectrum

5.2.1. The Influence of the Streamfunction Ψ

From the solution of the eigenvalue problem with boundary condition $\hat{u}(x = 0, y)$ four distinct symmetric discrete eigenmodes were found. They are labeled with the prefix **S** and numbered starting with the highest imaginary part of their eigenvalue. The modes are presented in Figure 5.3 for different base flows.
Mode **S1** is the most unstable and the fastest of the symmetric modes. Its phase speed is rather constant at around $c_r = 0.86$. Mode **S2** shows about half the growth rate of Mode **S1** with a growing phase speed for increasing γ. It is the second fastest of the symmetric modes. Modes **S3** and **S4** both are stable at different phase speeds with **S3** being the slower of the two. By changing the base flow, both growth rates and phase speeds are altered.
It is observed that mode **S3** and mode **S4** are intertwined in the spectrum and that, especially for the base flow Ψ_V, their branches show a relatively large leap where they meet. The question arises whether these two modes might actually constitute one single mode.
Growth rates rise without exception the more the streamfunction Ψ contains Ψ_V (corresponding to a weight $\chi = 0$). Phase speeds are affected very individually, i.e. mode **S1** and mode **S4** show very little difference in c_r and mode **S2** loses whereas mode **S3** gains in speed.
The locations of the modes around the base flow vortex are shown in contour plots in Figures 5.4-5.7. Both unstable modes lie on the outer upper flank of the vortex, mode **S1** being slightly atop mode **S2**. The stable modes lie on the outer lower flank of the vortex, while mode **S3** extends further underneath the vortex. Generally, it can be followed that for increasing phase speed the modes wander from underneath the vortex to its outer flank along its spinning direction up to its top.
The influence of the base flow streamfunction Ψ (or the weight χ) seems to be least when the flow is relaxed with weigth $\chi = 1$. The more component Ψ_V is added the more the base flow and thus the eigenmodes become distorted. Thus, Ψ_U creates the smallest deviation from the unrelaxed base flow solution. It was shown in Section 5.1 that this is indeed the case.

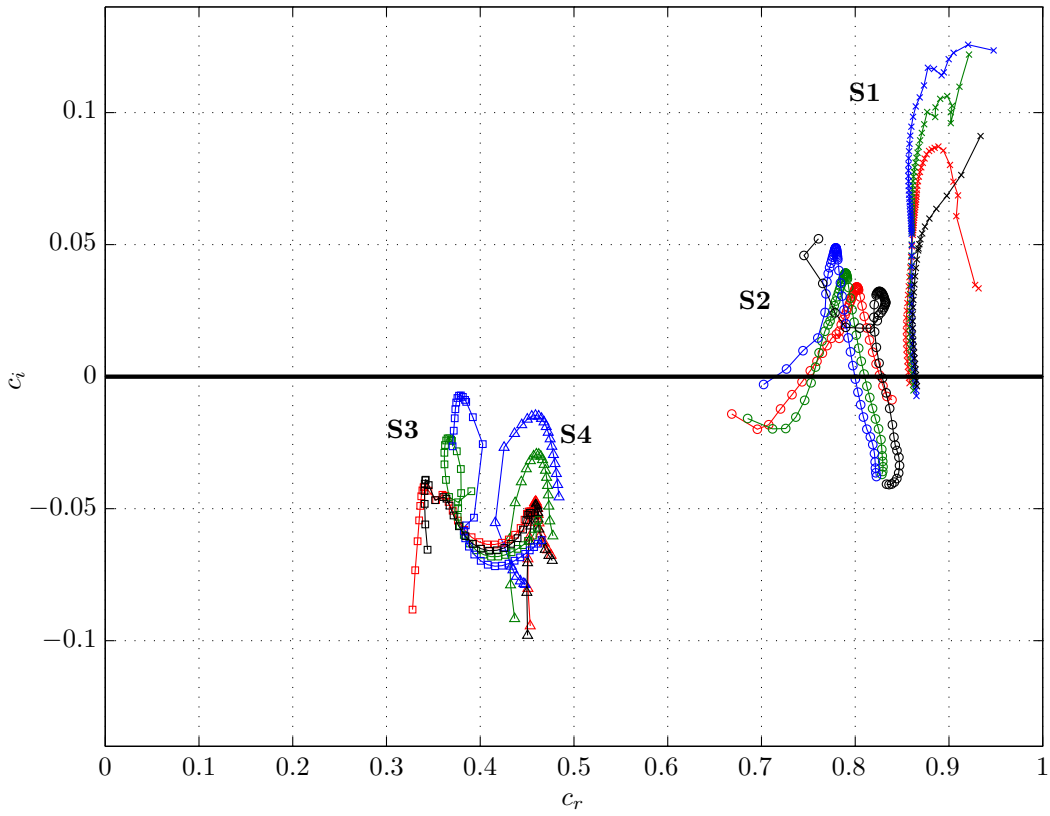

Figure 5.3.: Eigenspectrum for a baseflow of Re= 300 extracted at $z_{extr} = 94$ for parameters $L_x = 20$, $L_y = 15$, $N_x = 147$, $N_y = 120$ (**S1**, **S2**), $N_x = 154$, $N_y = 130$ (**S3**, **S4**) and $x_{\text{half}} = L_x/3$, $y_{\text{half}} = L_y/3$ and BC $\hat{u}(x = 0, y) = 0$. The branches are a result of varying the wavenumber γ. The colors represent: —Ψ_U, —Ψ_{U+V}, —Ψ_V, —unrelaxed.

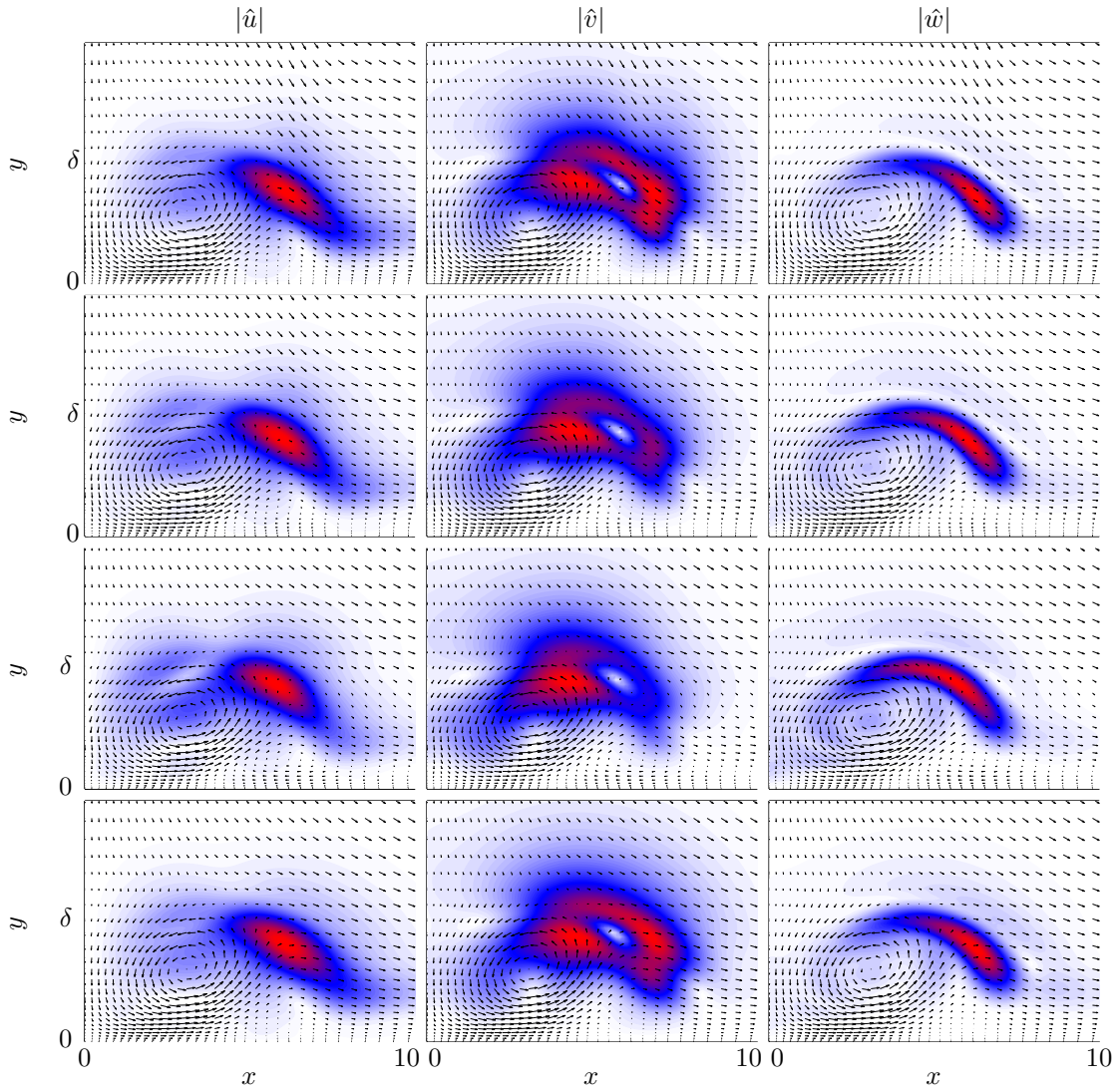

Figure 5.4.: Shapes of eigenmode **S1** for various Ψ at $z_{extr} = 94$ for Re = 300, $\gamma = 0.6$, $L_x = 20$, $L_y = 15$, $Nx = 147$, $Ny = 120$, $x_{\text{half}} = L_x/3$, $y_{\text{half}} = L_y/3$ and BC $\hat{u}(x = 0, y) = 0$. Top: Ψ_U, Second Row: Ψ_{U+V}, Third Row: Ψ_V, Bottom: unrelaxed. White equals 0 and red equals 1.

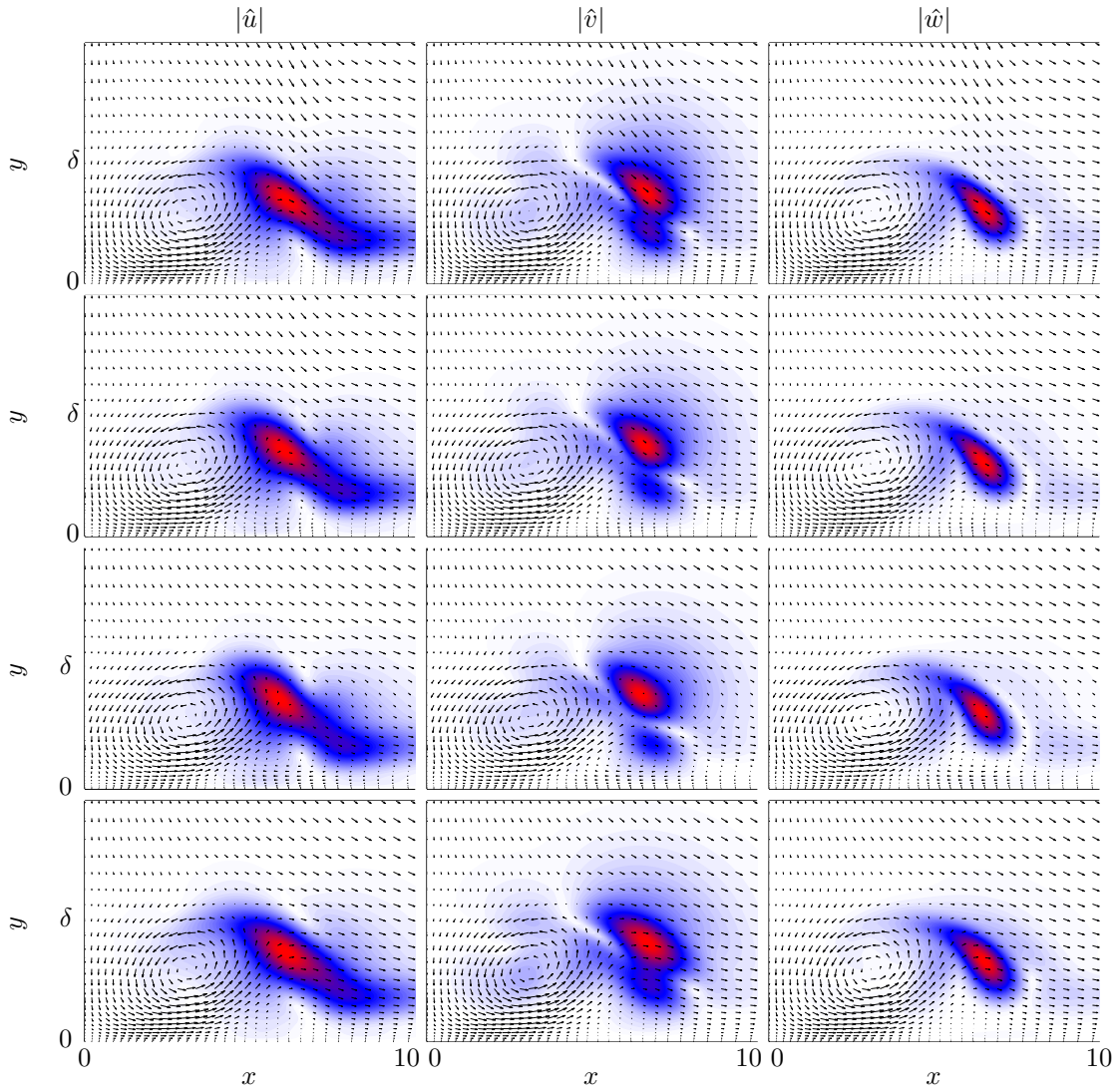

Figure 5.5.: Shapes of eigenmode **S2** for various Ψ at $z_{extr} = 94$ for Re = 300, $\gamma = 0.6$, $L_x = 20$, $L_y = 15$, $Nx = 147$, $Ny = 120$, $x_{\text{half}} = L_x/3$, $y_{\text{half}} = L_y/3$ and BC $\hat{u}(x = 0, y) = 0$. Top: Ψ_U, Second Row: Ψ_{U+V}, Third Row: Ψ_V, Bottom: unrelaxed. White equals 0 and red equals 1.

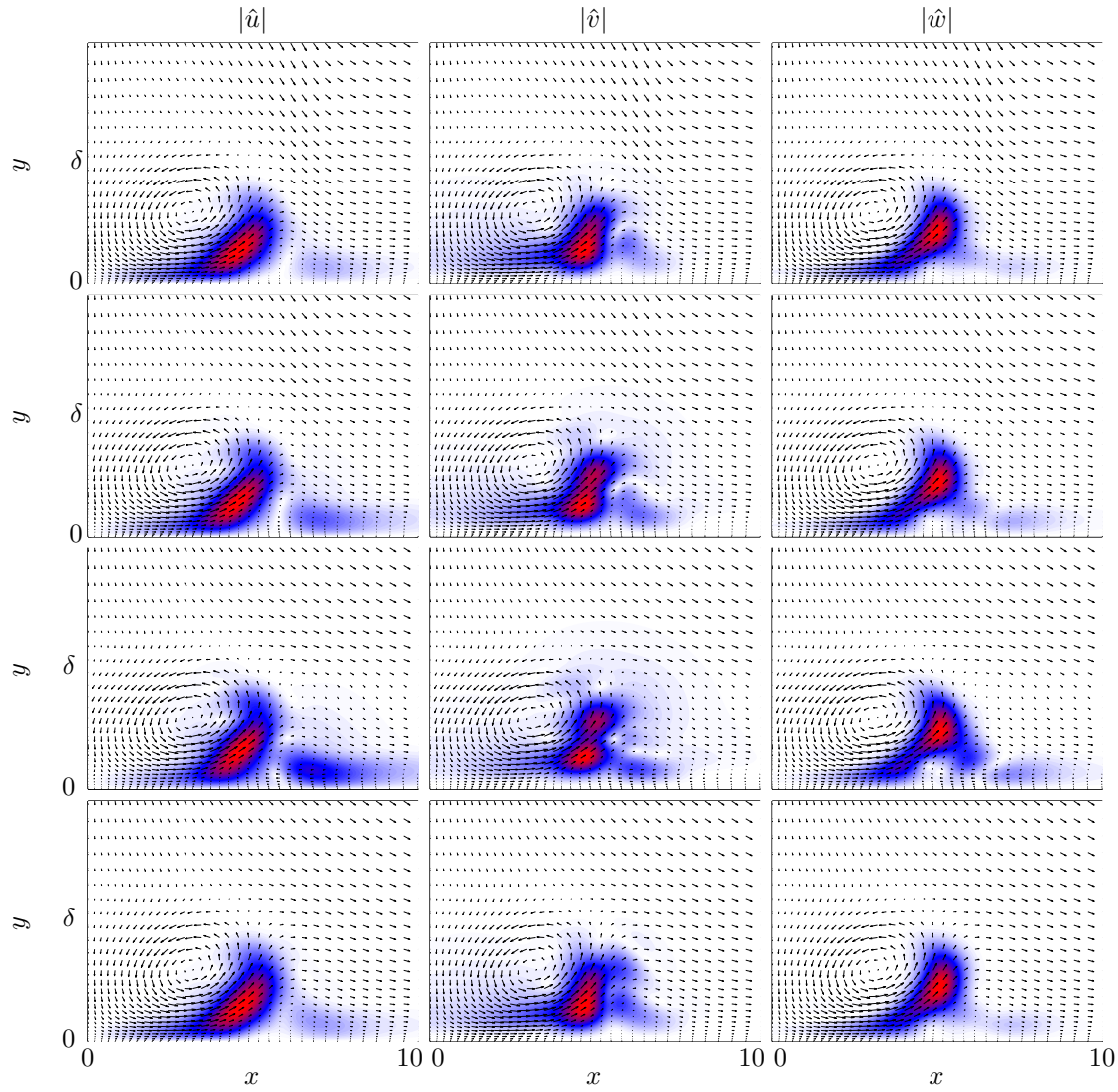

Figure 5.6.: Shapes of eigenmode **S3** for various Ψ at $z_{extr} = 94$ for Re = 300, $\gamma = 0.6$, $L_x = 20$, $L_y = 15$, $Nx = 154$, $Ny = 130$, $x_{\text{half}} = L_x/3$, $y_{\text{half}} = L_y/3$ and BC $\hat{u}(x = 0, y) = 0$. Top: Ψ_U, Second Row: Ψ_{U+V}, Third Row: Ψ_V, Bottom: unrelaxed. White equals 0 and red equals 1.

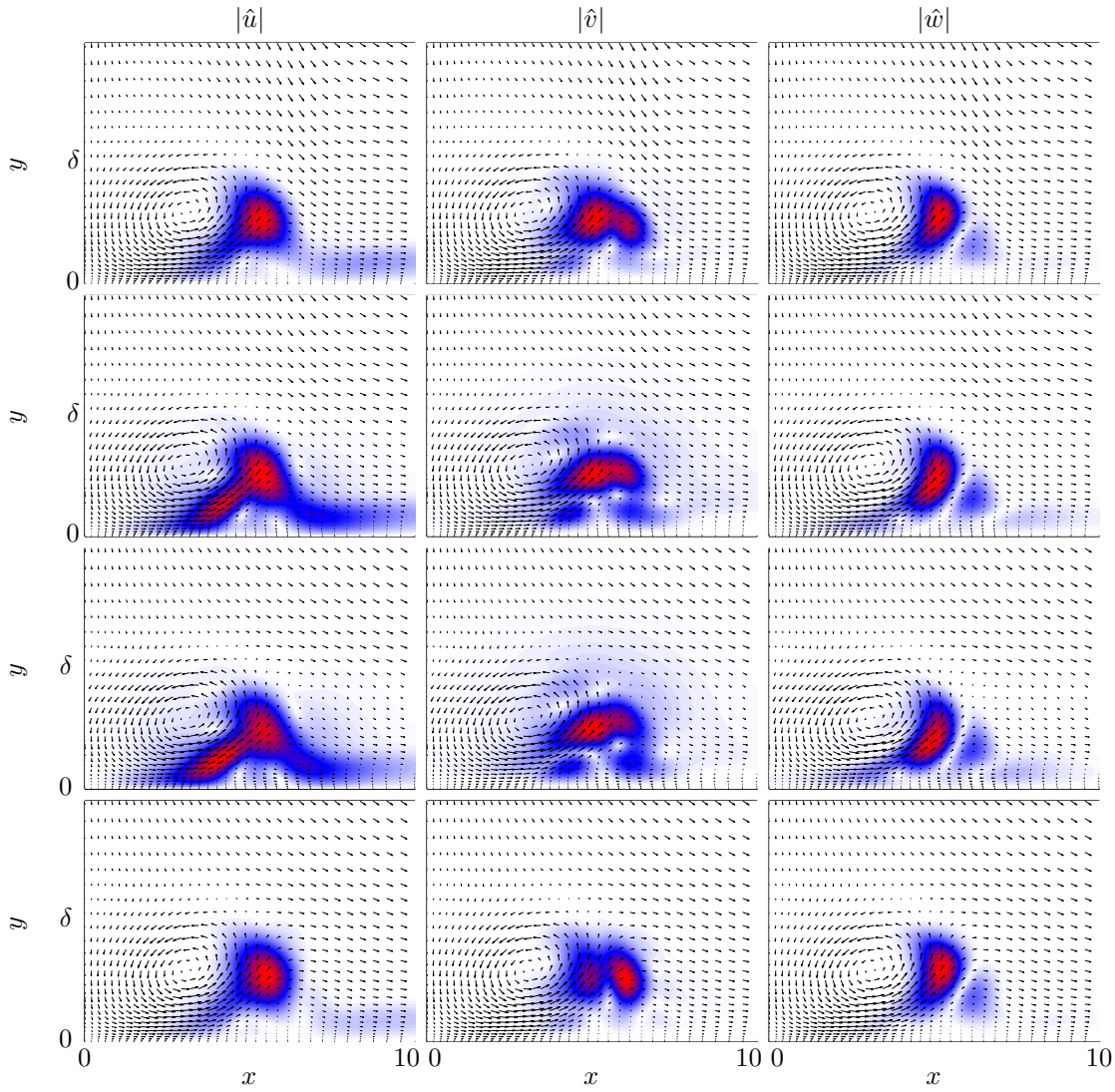

Figure 5.7.: Shapes of eigenmode **S4** for various Ψ at $z_{extr} = 94$ for Re = 300, $\gamma = 0.6$, $L_x = 20$, $L_y = 15$, $Nx = 154$, $Ny = 130$, $x_{\text{half}} = L_x/3$, $y_{\text{half}} = L_y/3$ and BC $\hat{u}(x = 0, y) = 0$. Top: Ψ_U, Second Row: Ψ_{U+V}, Third Row: Ψ_V, Bottom: unrelaxed. White equals 0 and red equals 1.

5.2.2. The Influence of the Wave Number γ

The branches of the eigenmodes in the spectrum were already shown in Figure 5.3. Here they are presented in the $\gamma - c_i$ plane. Figure 5.8(a) shows the branches of the unstable symmetric eigenmodes **S1** and **S2** and Figure 5.8(b) those of the damped symmetric eigenmodes **S3** and **S4**. Unfortunately, the branches become somewhat frayed below $\gamma = 0.3$ as marked in grey. This is mainly due to the solution domain being too small. This issue is addressed below in Section 5.3.2. However, for $\gamma > 0.3$ in agreement with the findings above, especially for the damped modes, the relaxed solution which best follows the unrelaxed one is that with weight $\chi = 1$. Moreover, mode **S1** shows an exceptionally little dependence on the weight χ and it is unstable for a broader range of wavenumbers γ than mode **S2**. Due to the fraying, the peak of mode **S1** unfortunately could not be recovered but if the Ψ_U branch can be considered as a hint it should come to lie around $\gamma = 0.1$. Further, it can be stated that modes **S2** and **S3** peak at a similar wavenumber of $\gamma \approx 0.3$. Mode **S4** show its peak at a higher value, namely for $0.8 < \gamma < 1$. As will be shown in Section 5.3.2, **S4** also is affected by the limited domain size L_x for a certain wavelength. It holds true also with this mode that for longer wavelengths the boundary forcing plays a non-negligible role. The only mode in this case not affected by it is mode **S3**. Due to its location underneath the vortex, the remaining distance to the quasi-infinite boundary is great enough for a 'natural' decay.

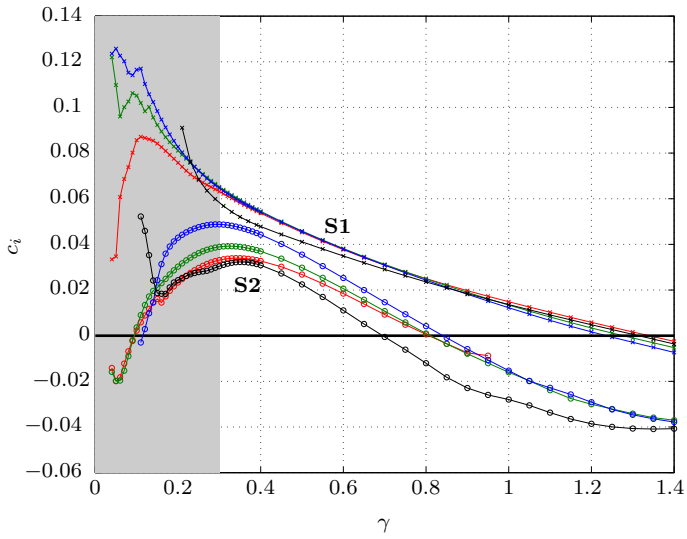

(a)

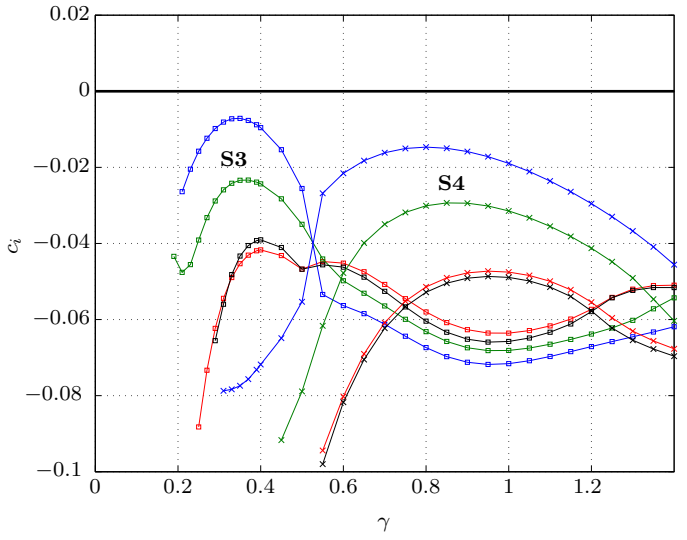

(b)

Figure 5.8.: Recovered eigenmodes' growth rates vs. γ for Re = 300 at $z_{extr} = 94$ for parameters $L_x = 20$, $L_y = 15$, $N_x = 147$, $N_y = 120$ (**S1**, **S2**), $N_x = 154$, $N_y = 130$ (**S3**, **S4**) and $x_{\text{half}} = L_x/3$, $y_{\text{half}} = L_y/3$ and BC $\hat{u}(x = 0, y) = 0$. The colors represent: —Ψ_U, —Ψ_{U+V}, —Ψ_V, —unrelaxed.

5.2.3. The Influence of the BCs for $\hat{u}(x = 0, y)$

The BCs 2.32 were changed from $\hat{u}(x = 0, y) = 0$ (Dirichlet) to $\partial^2/\partial x^2 \hat{u}(x = 0, y) = 0$ in order to allow more degrees of freedom to the solution and allow for antisymmetric modes as for odd forcing. Indeed, there was a new mode that appeared. Subsequently, it will be labeled **A1**, the prefix signifying '*antisymmetric*'. This mode has a non-zero $\hat{u}$ component at $x = 0$, allowing for a chord-wise 'gust'. Its contours are presented in Figure 5.11. The phase speed becomes negative for large wavelengths. An explanation for this is the fact that the wavenumber vector is of an arbitrary oblique direction, whose projection upon the z-direction becomes negative when the spanwise wavenumber γ reduces. The symmetric modes **S1**-**S4** were again recovered with very good agreement to the original BC solutions. There is no apparent difference in their qualitative shapes as they remain like the ones shown in Figures 5.4-5.7 (see Appendix C). Their position in the spectrum remains unchanged as well. The spectrum is presented in Figure 5.9 and their branches along γ in Figure 5.10. **A1** has the highest growth rate, thus showing the highest affinity to instability with its peak at $\gamma \approx 0.5$. Again, the variation of the base flow (different Ψ) has a minor effect on the solution.

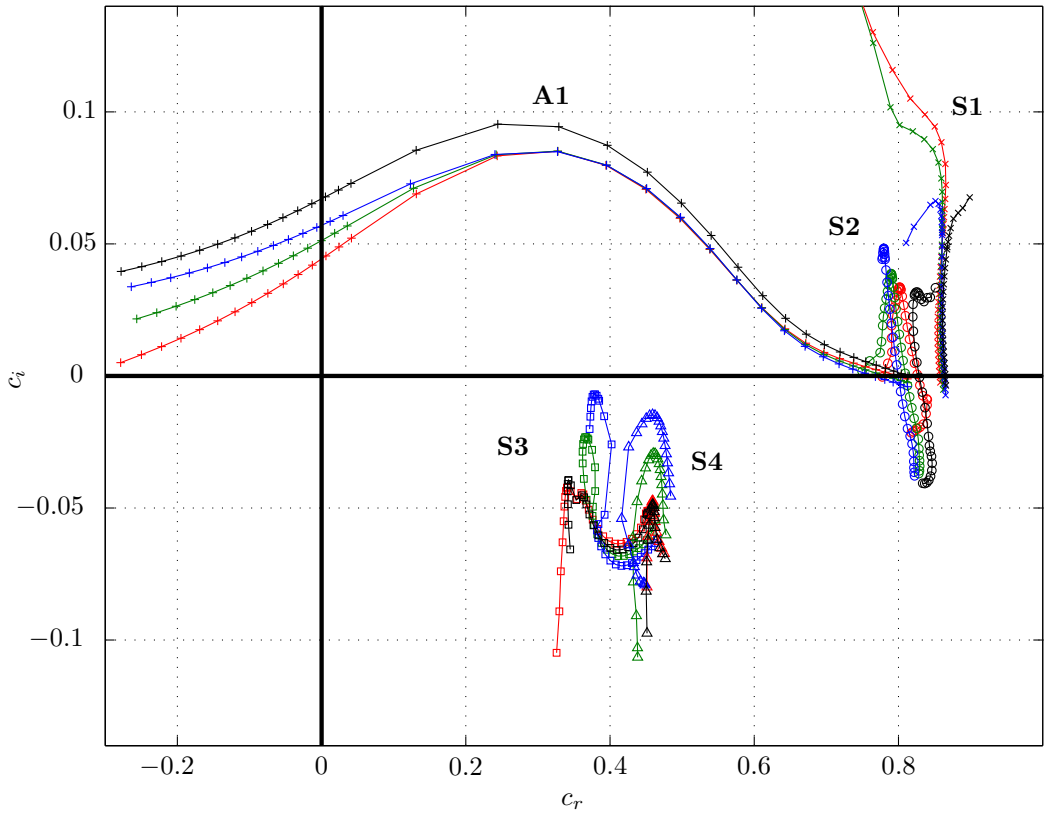

Figure 5.9.: Eigenspectrum for a baseflow of Re= 300 extracted at $z_{extr} = 94$ for parameters $L_x = 20$, $L_y = 15$, $N_x = 147$, $N_y = 120$ (**S1**, **S2**, **A1**), $N_x = 154$, $N_y = 130$ (**S3**, **S4**) and $x_{\text{half}} = L_x/3$, $y_{\text{half}} = L_y/3$ and BC $\partial^2/\partial x^2 \hat{u}(x = 0, y) = 0$. The branches are a result of varying the wavenumber γ. The colors represent: —Ψ_U, —Ψ_{U+V}, —Ψ_V, —unrelaxed.

S1

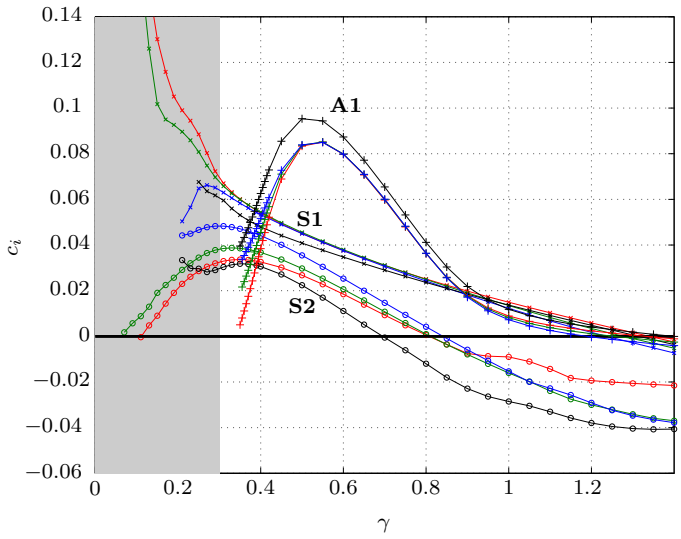

(a)

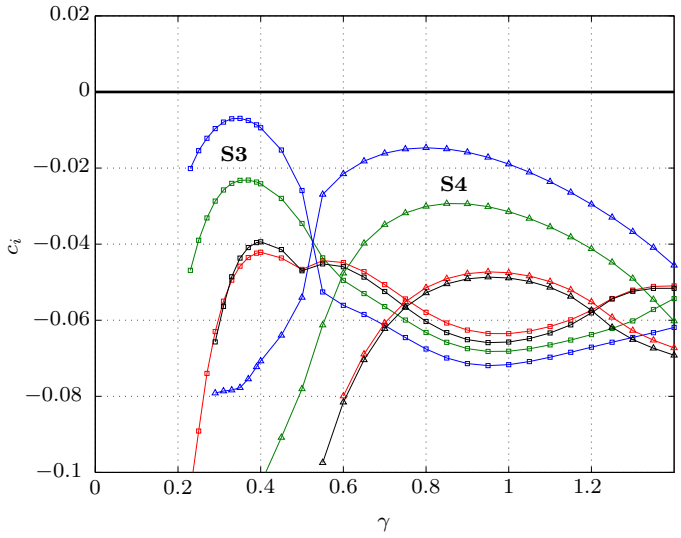

(b)

Figure 5.10.: Recovered eigenmodes' growth rates vs. γ for $\mathrm{Re} = 300$ at $z_{extr} = 94$ for parameters $L_x = 20$, $L_y = 15$, $N_x = 147$, $N_y = 120$ (**S1**, **S2**, **A1**), $N_x = 154$, $N_y = 130$ (**S3**, **S4**) and $x_{\mathrm{half}} = L_x/3$, $y_{\mathrm{half}} = L_y/3$ and BC $\partial^2/\partial x^2 \hat{u}(x = 0, y) = 0$. The colors represent: —Ψ_U, —Ψ_{U+V}, —Ψ_V, —unrelaxed.

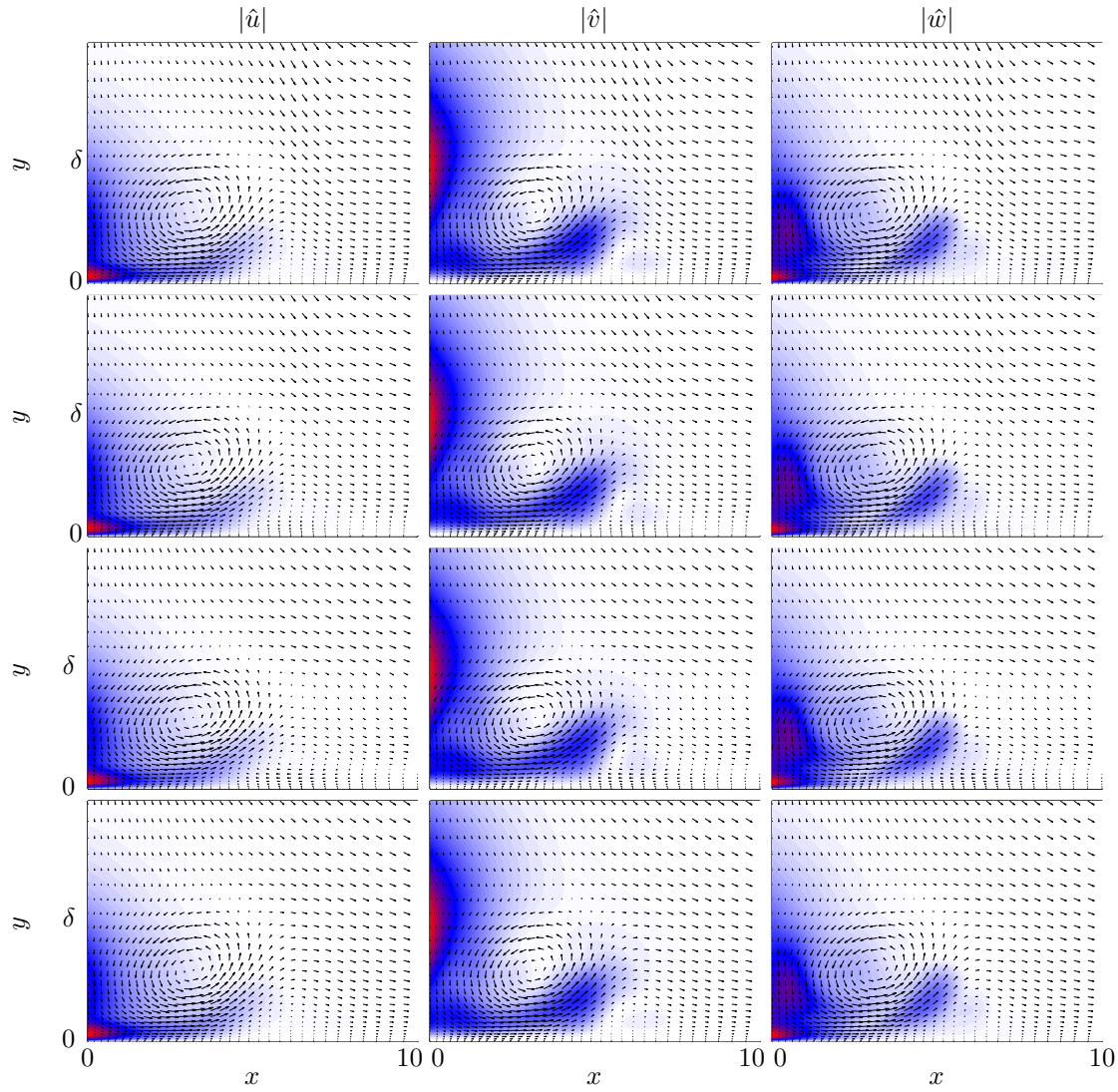

Figure 5.11.: Shapes of eigenmode **A1** for various Ψ at $z_{extr} = 94$ for Re $= 300$, $\gamma = 0.6$, $L_x = 20$, $L_y = 15$, $Nx = 147$, $Ny = 120$, $x_{\text{half}} = L_x/3$, $y_{\text{half}} = L_y/3$ and BC $\partial^2/\partial x^2 \hat{u}(x = 0, y) = 0$. Top: Ψ_U, Second Row: Ψ_{U+V}, Third Row: Ψ_V, Bottom: unrelaxed. White equals 0 and red equals 1.

5.2.4. The Influence of the Extraction Location z_{extr}

The absolute minimum of $W_{b,z}$ lies at $z \approx 159$. While good for physical correctness of the equations, the location lies in the midst of modal growth and the vortices have moved further apart. However, if discrete modes were actually identifiable at the upstream location then eigenmodes of similar shape ought to be observable also further downstream. With that in mind, simulations were run at a downstream location of $z_{extr} = 159$ compared to the above of $z_{extr} = 94$.
Indeed, at the new location the modes were qualitatively recovered, however, their growth rates differ. At this downstream location the vortices have moved further apart and the IMPACT base flow features a noticeable secondary modal growth when looking at a spectral energy decomposition like the one in Figure B.5, Appendix B. Only modes **S1**-**S4** were recovered because the boundary condition was not altered from $\hat{u}(x = 0, y) = 0$. While the modes still have about the same phase speeds, mode **S2** here presents higher growth rates than mode **S1**, in contrast to the above as can be seen in Figure 5.12 and Figure 5.17. Mode **S4** seems to become unstable for a wavenumber of $\gamma \approx 0.25$ when computed with a weight of $\chi = 0$ (Ψ_V), shifting its maximum growth rate to lower γ. The shapes of all modes are well recognizable in Figures 5.13-5.16. For the same wavelength, though, modes **S1** and **S2** have moved closer to the top of the vortex. Again, numerical convergence was obtained only for $\gamma > 0.3$, while the quantitative resolution for lower values was limited by the issue of the too close quasi-infinite boundary at $x = L_x$. The region of interest is again marked in grey in 5.17(a).

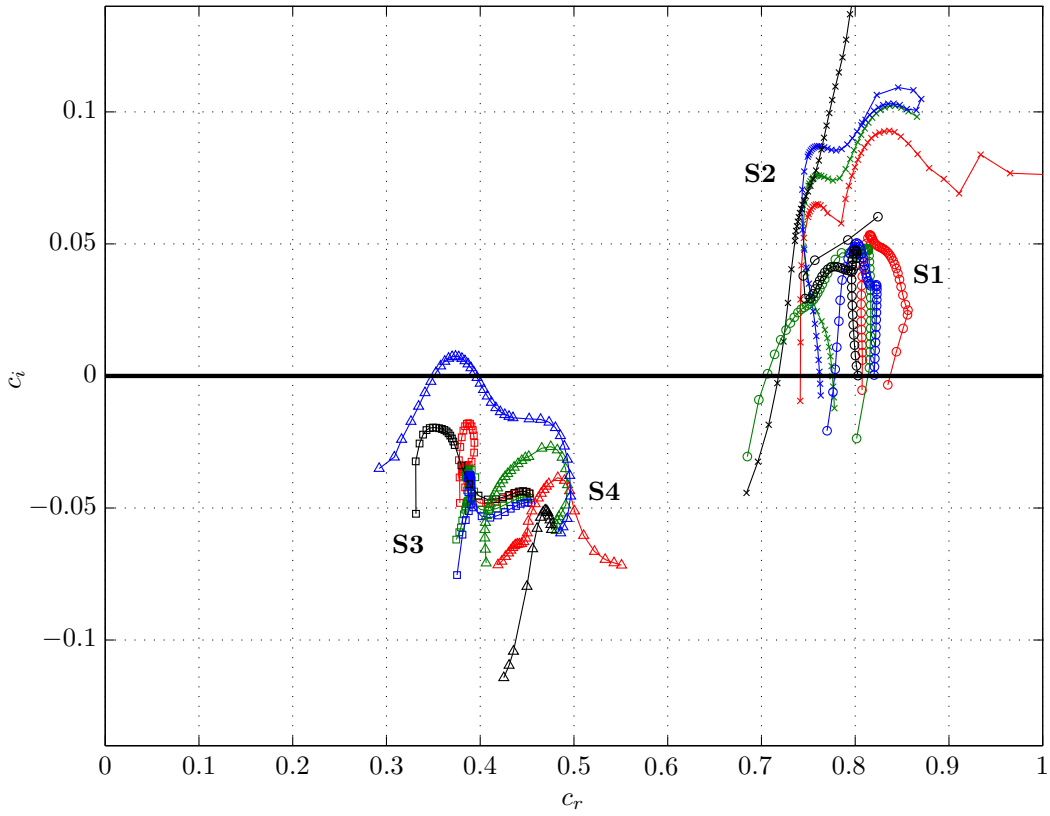

Figure 5.12.: Eigenspectrum for a baseflow of Re= 300 extracted at $z_{extr} = 159$ for parameters $L_x = 20$, $L_y = 15$, $N_x = 147$, $N_y = 120$ (**S1**, **S2**), $N_x = 154$, $N_y = 130$ (**S3**, **S4**) and $x_{\text{half}} = L_x/3$, $y_{\text{half}} = L_y/3$ and BC $\hat{u}(x = 0, y) = 0$. The branches are a result of varying the wavenumber γ. The colors represent: —Ψ_U, —Ψ_{U+V}, —Ψ_V, —unrelaxed.

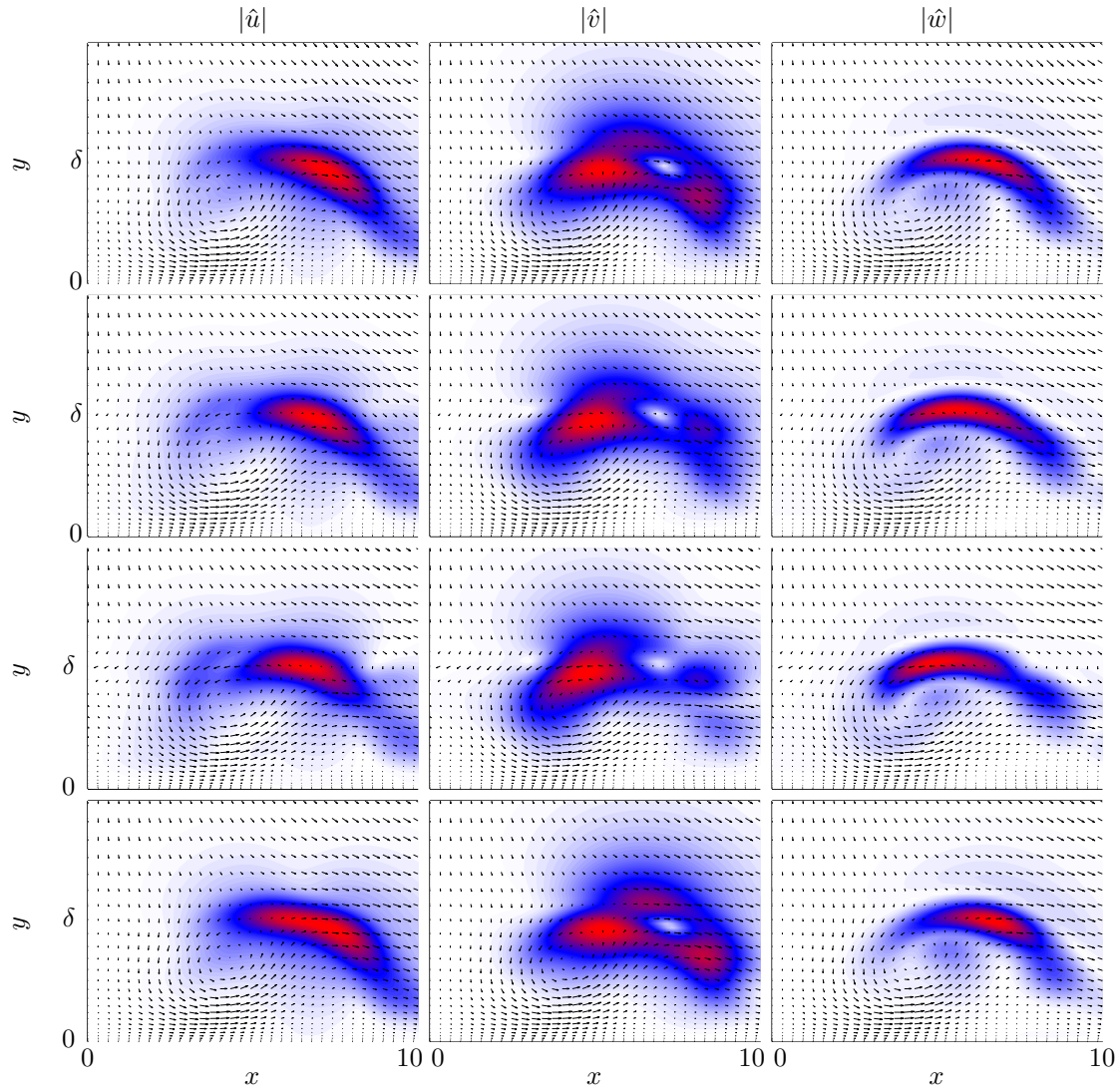

Figure 5.13.: Shapes of eigenmode **S1** for various Ψ at $z_{extr} = 159$ for Re $= 300$, $\gamma = 0.6$, $L_x = 20$, $L_y = 15$, $Nx = 147$, $Ny = 120$, $x_{\text{half}} = L_x/3$, $y_{\text{half}} = L_y/3$ and BC $\hat{u}(x = 0, y) = 0$. Top: Ψ_U, Second Row: Ψ_{U+V}, Third Row: Ψ_V, Bottom: unrelaxed. White equals 0 and red equals 1.

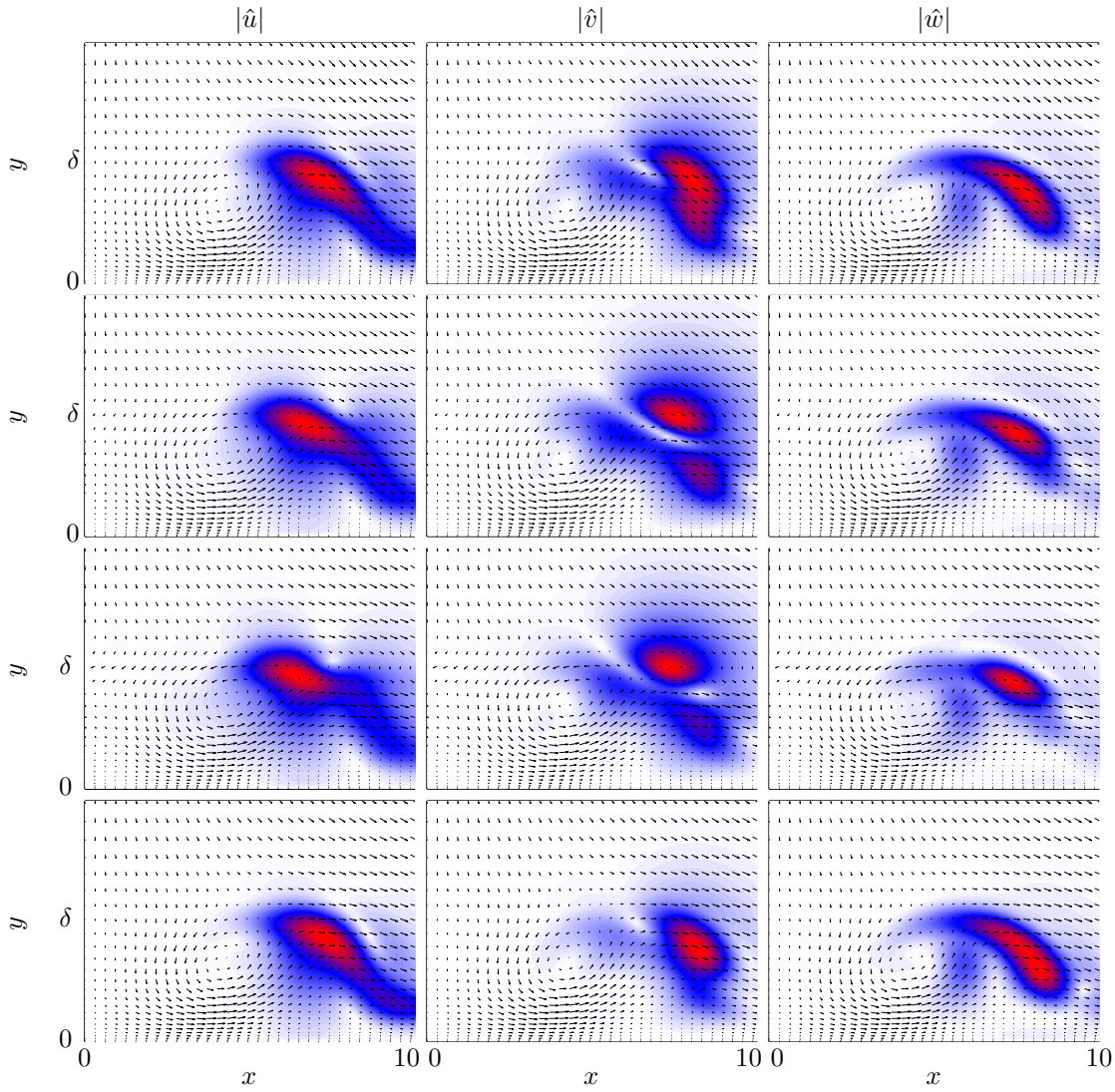

Figure 5.14.: Shapes of eigenmode **S2** for various Ψ at $z_{extr} = 159$ for Re $= 300$, $\gamma = 0.6$, $L_x = 20$, $L_y = 15$, $Nx = 147$, $Ny = 120$, $x_{\text{half}} = L_x/3$, $y_{\text{half}} = L_y/3$ and BC $\hat{u}(x = 0, y) = 0$. Top: Ψ_U, Second Row: Ψ_{U+V}, Third Row: Ψ_V, Bottom: unrelaxed. White equals 0 and red equals 1.

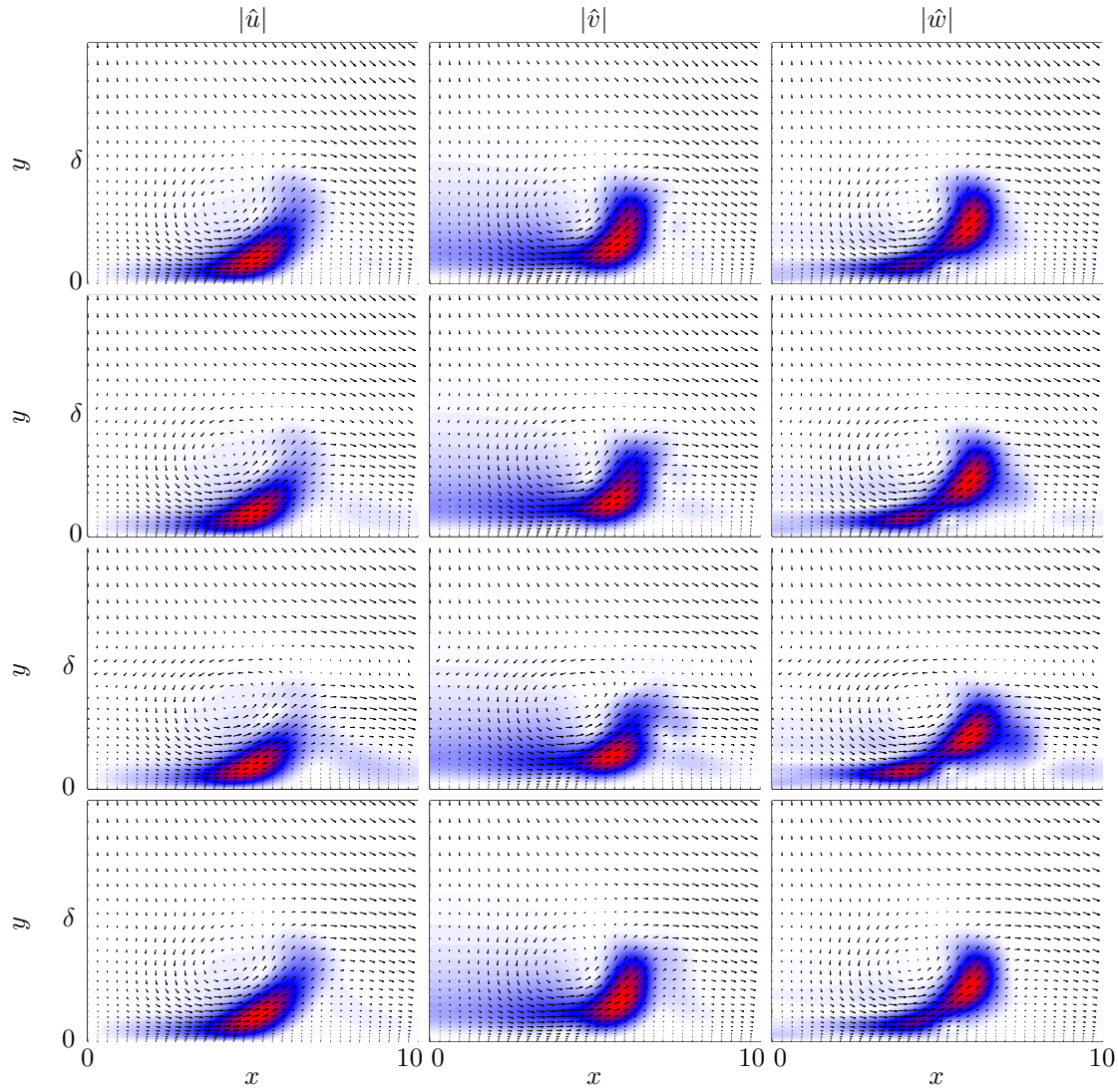

Figure 5.15.: Shapes of eigenmode **S3** for various Ψ at $z_{extr} = 159$ for Re $= 300$, $\gamma = 0.6$, $L_x = 20$, $L_y = 15$, $Nx = 154$, $Ny = 130$, $x_{\text{half}} = L_x/3$, $y_{\text{half}} = L_y/3$ and BC $\hat{u}(x = 0, y) = 0$. Top: Ψ_U, Second Row: Ψ_{U+V}, Third Row: Ψ_V, Bottom: unrelaxed. White equals 0 and red equals 1.

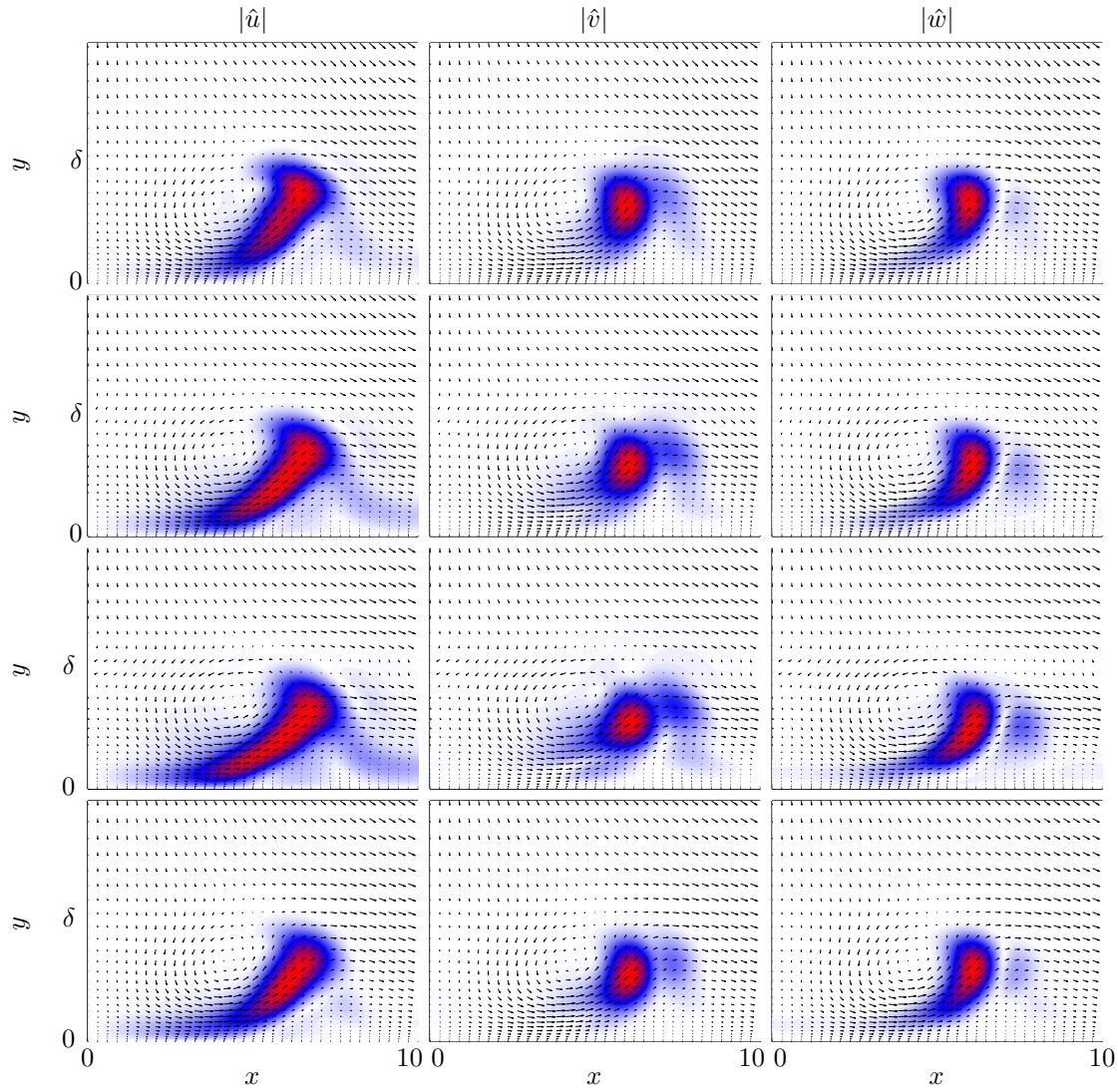

Figure 5.16.: Shapes of eigenmode **S4** for various Ψ at $z_{extr} = 159$ for Re $= 300$, $\gamma = 0.6$, $L_x = 20$, $L_y = 15$, $Nx = 154$, $Ny = 130$, $x_{\text{half}} = L_x/3$, $y_{\text{half}} = L_y/3$ and BC $\hat{u}(x = 0, y) = 0$. Top: Ψ_U, Second Row: Ψ_{U+V}, Third Row: Ψ_V, Bottom: unrelaxed. White equals 0 and red equals 1.

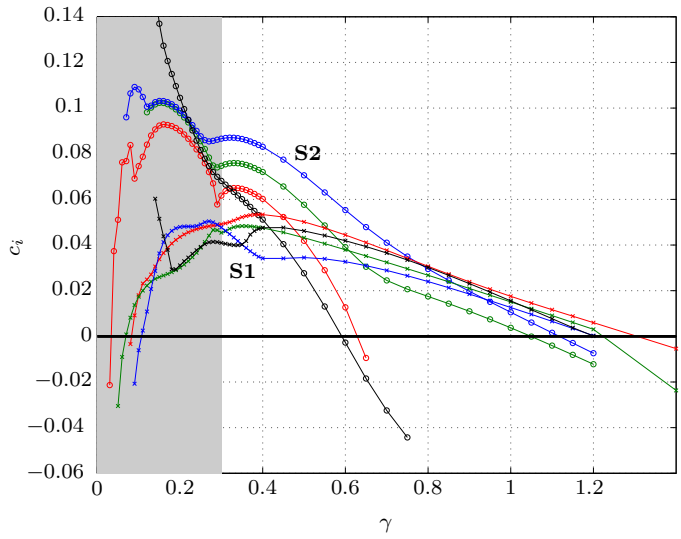

(a)

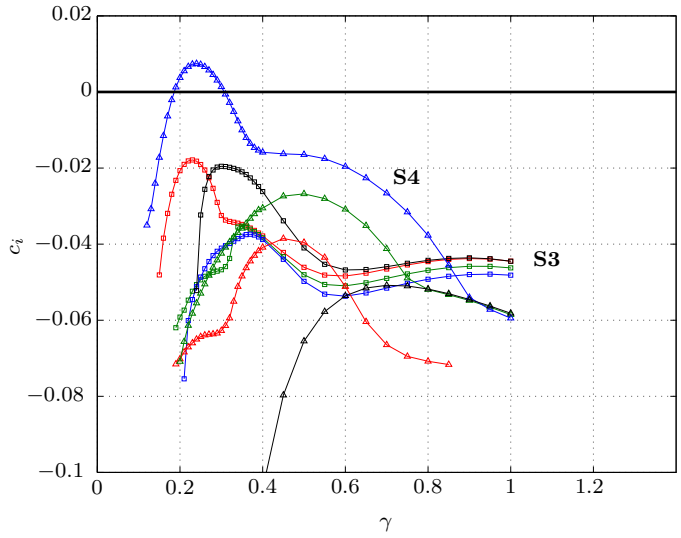

(b)

Figure 5.17.: Recovered eigenmodes' growth rates vs. γ for Re $= 300$ at $z_{extr} = 159$ for parameters $L_x = 20$, $L_y = 15$, $N_x = 147$, $N_y = 120$ (**S1**, **S2**), $N_x = 154$, $N_y = 130$ (**S3**, **S4**) and $x_{\text{half}} = L_x/3$, $y_{\text{half}} = L_y/3$ and BC $\hat{u}(x = 0, y) = 0$. The colors represent: —Ψ_U, —Ψ_{U+V}, —Ψ_V, —unrelaxed.

5.3. The Discrete Eigenfunctions

5.3.1. The Influence of the Streamfunction Ψ

Figure 5.18 shows the four symmetric eigenmodes recovered for boundary conditions $\hat{u}(x = 0, y) = 0$. For each mode the four distinct solutions that emerge from the different base flow relaxations are presented. The data is taken at the same wave number $\gamma = 0.6$ for all modes and the figures show all velocity components for a certain Ψ. The eigenfunctions $|\hat{u}|$, $|\hat{v}|$ and $|\hat{w}|$ are normalized with respect to the maximum of a local vector norm $\phi = \max||(|\hat{u}(x,y)|, |\hat{v}(x,y)|, |\hat{w}(x,y)|)^T||$ and plotted through their respective maximum to yield a relative comparison between them. The x coordinate of the maximum of each component is annotated in the plots.
It is apparent that the most prominent velocity component is the spanwise $|\hat{w}|$ followed by $|\hat{u}|$ and $|\hat{v}|$ in that order. The influence of the streamfunction Ψ shows that for decreasing weight χ (increasing amount of Ψ_V) all modes' but **S4**'s maxima move up towards the boundary layer edge. Simultaneously, for the same trend of χ the maxima tend to shift to lower x. Some of the solutions feature outliers in terms of their maximum location, where the base flow was altered in the extent to where that location would shift. These outliers are $\max|\hat{v}(x,y)|$ of mode **S1** for Ψ_U or $\max|\hat{u}(x,y)|$ of mode **S4** for Ψ_V or $\max|\hat{v}(x,y)|$ of mode **S4** for the *unrelaxed* case. These nuances can also be looked up in Figures 5.4-5.7 which are presented for the same parameters.

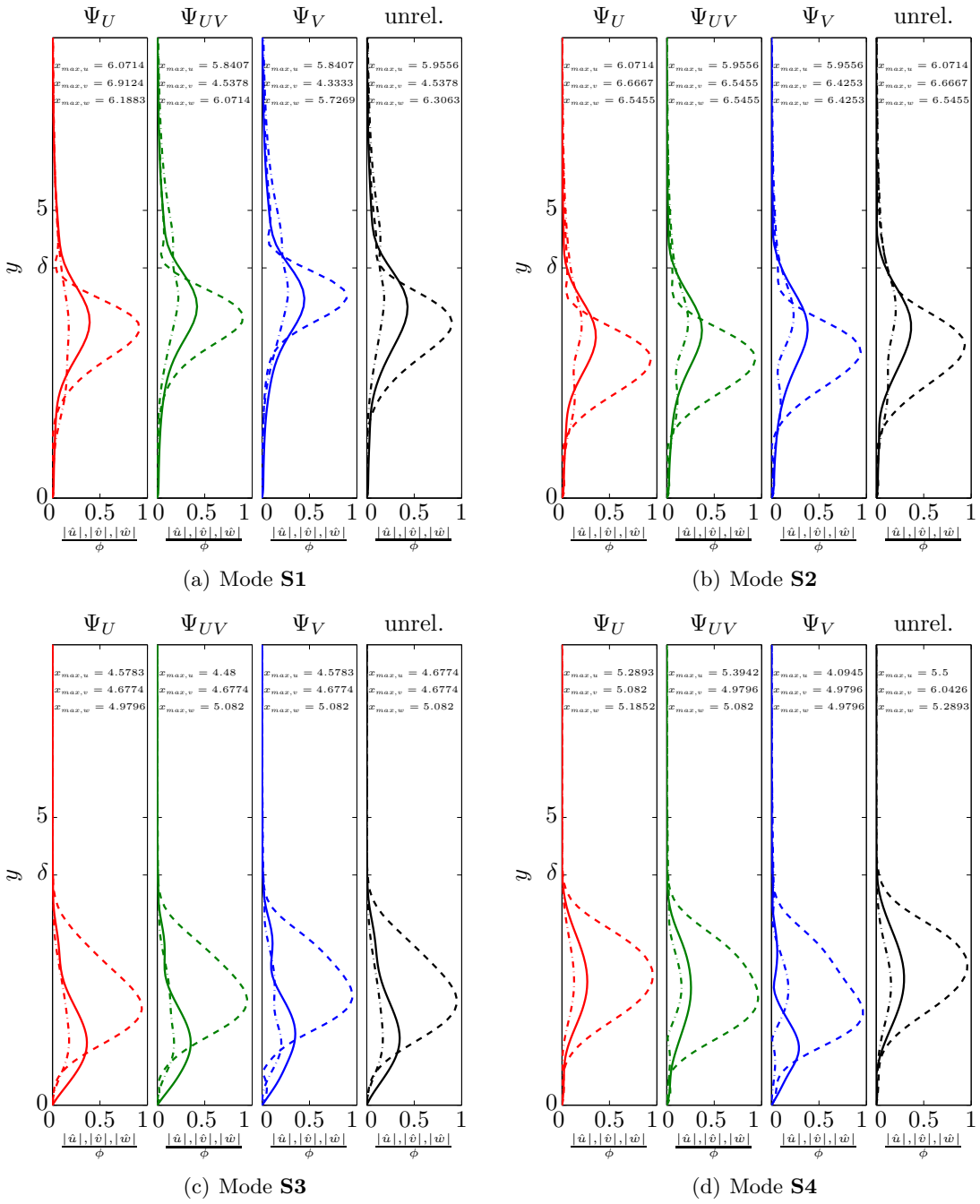

(a) Mode **S1**

(b) Mode **S2**

(c) Mode **S3**

(d) Mode **S4**

Figure 5.18.: Symmetric eigenmodes' velocity profiles over y for different Ψ. The velocities are normalized with $\phi = \max||(\hat{u}, \hat{v}, \hat{w})||$ and plotted through their respective maxima. Parameters hereof are $\mathrm{Re} = 300$, $\gamma = 0.6$ at $z_{extr} = 94$, $L_x = 20$, $L_y = 15$, $N_x = 147$, $N_y = 120$ (**S1**, **S2**), $N_x = 154$, $N_y = 130$ (**S3**, **S4**) and $x_{\mathrm{half}} = L_x/3$, $y_{\mathrm{half}} = L_y/3$ and BC $\hat{u}(x = 0, y) = 0$.The colors represent: —Ψ_U, —Ψ_{U+V}, —Ψ_V, — unrelaxed. Solid line: $|\hat{u}|$, dashed-dotted line: $|\hat{v}|$, dashed line: $|\hat{w}|$.

5.3.2. The Influence of the Wave Number γ

Figure 5.19 illustrates how the symmetric eigenfunctions' velocities **S1**-**S4** shift in dependence of γ. The plots feature data from three different wave numbers in equal steps. Modes **S1**-**S3** are shown for $\gamma = \{0.4, 0.6, 0.8\}$ and mode **S4** for $\gamma = \{0.6, 0.8, 1.0\}$ the modes are again plotted through their respective maxima and normalized with the same maximum vector norm ϕ. Mode **S1** travels towards the edge of the boundary layer for increasing wavenumbers. At the same time, component $|\hat{w}|$ loses in amplitude while $|\hat{u}|$ and $|\hat{v}|$ gain somewhat. $|\hat{v}|$ develops a second peak below its original maximum that eventually also replaces the latter. $|\hat{w}|$ also develops a new feature in form of a little peak just above the boundary layer edge. Mode **S2** has the same tendency of travelling to the boundary layer edge for increasing γ, however its qualitative shape remains the same. The velocity components show the same behaviour, shifting amplitude from $|\hat{w}|$ to the components $|\hat{u}|$ and $|\hat{v}|$. Mode **S3** moves its maxima closer to the boundary as γ increases, manifesting an opposite behavior to the two unstable symmetric modes. Very prominent is the fact, that $|\hat{u}|$ has a strong increase in amplitude, about doubling its value and showing a very distinct peak close to the boundary for higher γ. Mode **S4** shows similar behavior to that of mode **S3**. The above descriptions while only presented for $\Psi = \Psi_U$ hold for all χ and can be looked up in Appendix C for the other scenarios. The qualitative tracks of the $|\hat{w}|$-maxima under a γ variation with respect to the base flow can be examined in Figure 5.20 for all relaxation scenarios. The arrows follow the streamlines of the base flow vortex which has its center at around ($x \approx 3, y \approx 2.5$). It can be generally remarked that the unstable modes **S1** and **S2** show greater variation of their maximum loci by travelling a longer distance upwards. The stable modes on the other hand seem more stationary with the tendency of moving downward. In any case, the agreement of the solution for different relaxations is very good.

At this point a remark on the numerical convergence for $\gamma \leq 0.3$ is in order. A limiting factor for the solution of the eigenvalue problem for small γ was the location of the quasi-infinite boundary $x = L_x$. For the modes lying on the outer flank of the vortex the value of L_x proved to be too small and hence the boundary forcing influenced the solution inside the domain by a considerable amount. To illustrate this, modes' **S1** and **S2** $|\hat{u}|$ component is averaged over y inside the boundary layer and logarithmically plotted in Figure 5.21. Clearly it is visible that for wave numbers $\gamma \lesssim 0.3$ the solution bulges out close to the boundary $x = L_x$. For the lowest γ the influence is noticeable even further inside the boundary. Mode **S4** is affected by this problem as well. As one can see in Figure 5.22, there is alarge change in the exponential decay rate between $\gamma = 0.8$ and $\gamma = 0.7$. While this may be of physical nature, the fact that reducing γ further to the value of 0.6 leads to irregularities inside the domain, most likely signals a domain that is too small. Figures 5.21 and 5.22 show an average of $|\hat{u}|$ divided by $\max|\hat{u}|$ derived with a relaxation with Ψ_U, it is however representative for all Ψ since these effects held true.

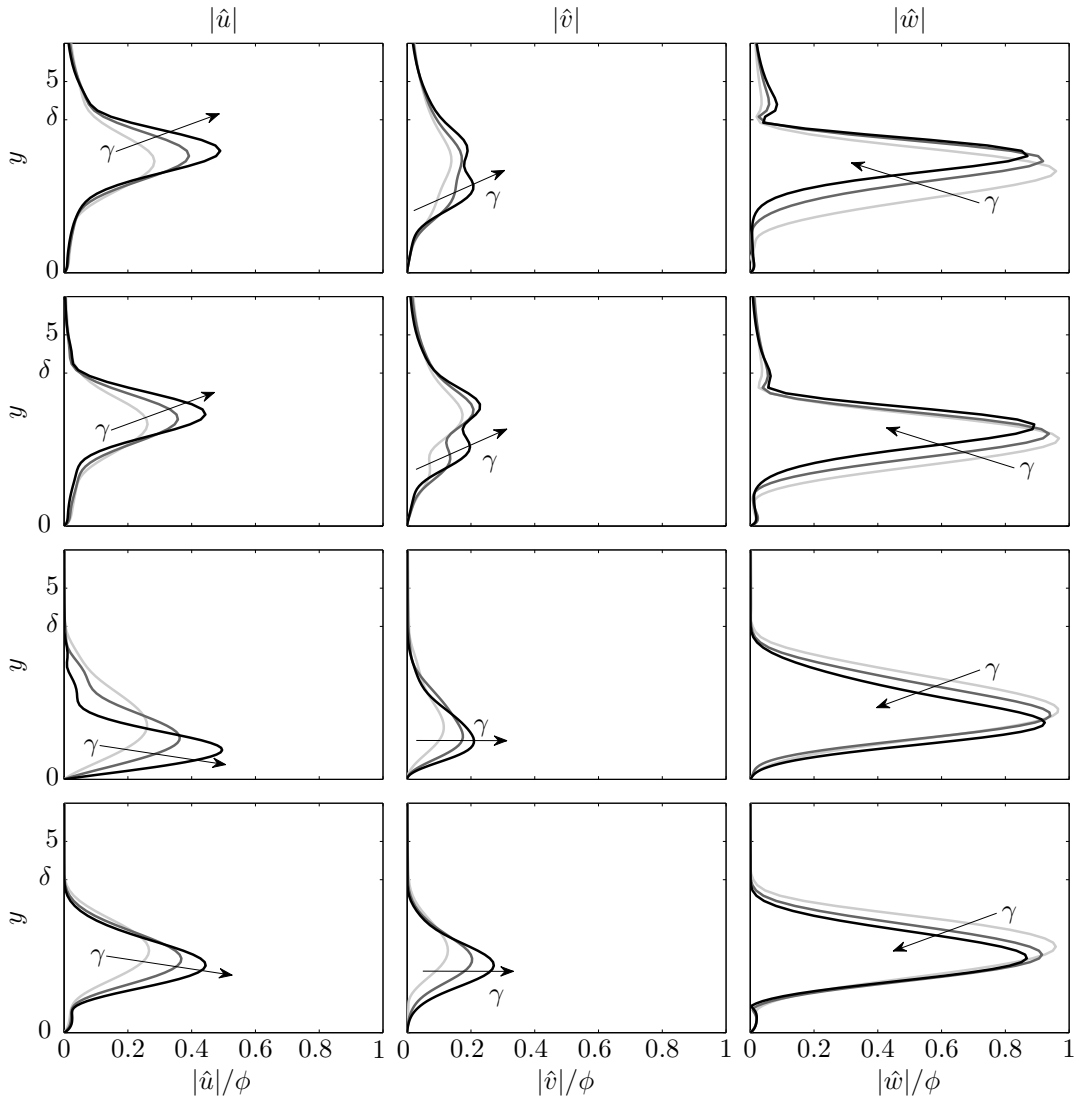

Figure 5.19.: Symmetric eigenmodes' velocity profiles over y for varying γ and a relaxation with Ψ_U ($\chi = 1$). The velocities are normalized with $\phi = \max||(\hat{u}, \hat{v}, \hat{w})||$ and plotted through their respective maxima. Parameters hereof are Re = 300 at $z_{extr} = 94$, $L_x = 20$, $L_y = 15$, $N_x = 147$, $N_y = 120$ (**S1**, **S2**), $N_x = 154$, $N_y = 130$ (**S3**, **S4**) and $x_{\text{half}} = L_x/3$, $y_{\text{half}} = L_y/3$ and BC $\hat{u}(x = 0, y) = 0$. Top: **S1**, second row: **S2**, third row: **S3**, bottom: **S4**.

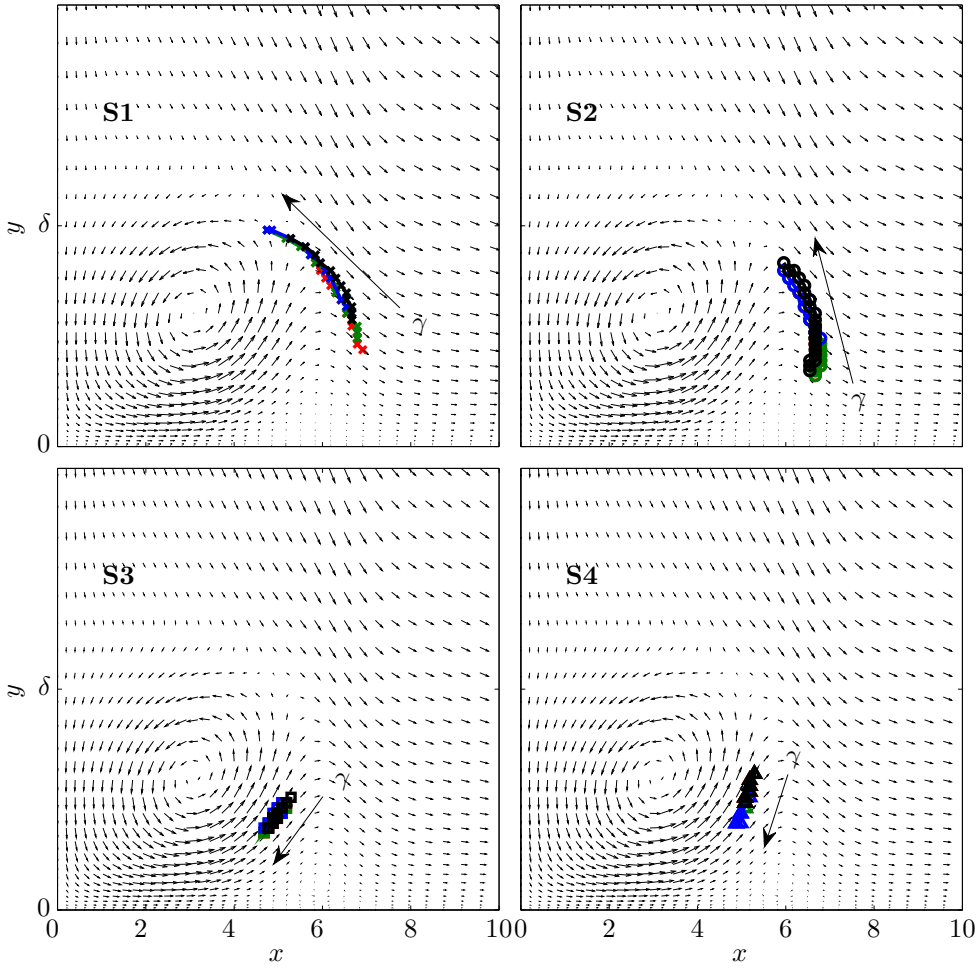

Figure 5.20.: Tracks of the maximum values of $|\hat{w}|$ of the symmetric eigenmodes under varying γ for different relaxations. Parameters were set to Re = 300 at $z_{extr} = 94$, $L_x = 20$, $L_y = 15$, $N_x = 147$, $N_y = 120$ (**S1**, **S2**), $N_x = 154$, $N_y = 130$ (**S3**, **S4**) and $x_{\text{half}} = L_x/3$, $y_{\text{half}} = L_y/3$ and BC $\hat{u}(x = 0, y) = 0$. The colors represent: —Ψ_U, —Ψ_{U+V}, —Ψ_V, —unrelaxed.

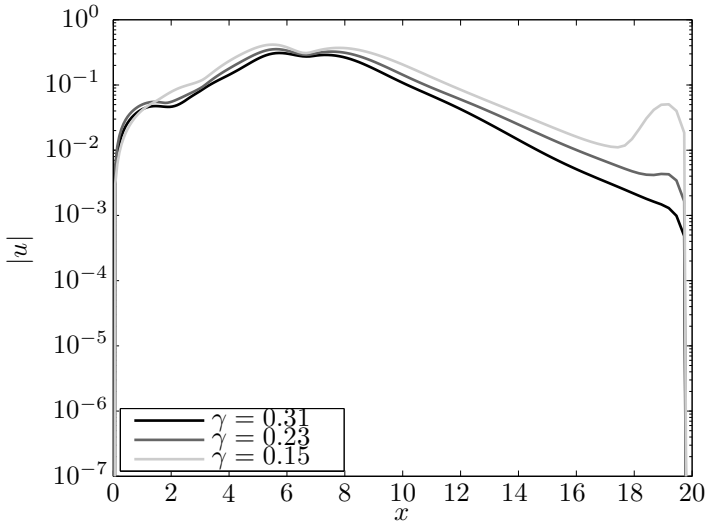

(a) Mode **S1** averaged over $0 \leq y \leq 3.5$

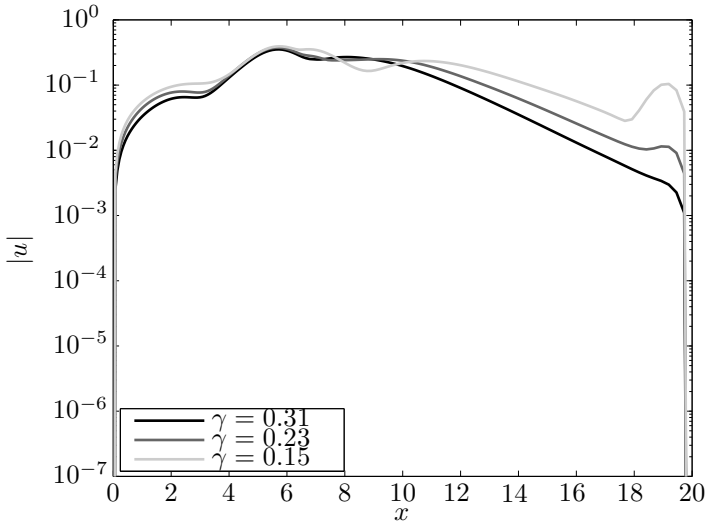

(b) Mode **S2** averaged over $0 \leq y \leq 3.5$

Figure 5.21.: The unstable modes' **S1** and **S2** decay along x is influenced at the far-field boundary as γ approaches smaller values. There is a noticeable overshoot at the domain edge for $\gamma \lesssim 0.3$. These simulations were run for parameters Re $= 300$ at $z_{extr} = 94$, $\Psi = \Psi_U$ ($\chi = 1$), $L_x = 20$, $L_y = 15$, $N_x = 147$, $N_y = 120$ and $x_{\text{half}} = L_x/3$, $y_{\text{half}} = L_y/3$ and BC $\hat{u}(x = 0, y) = 0$.

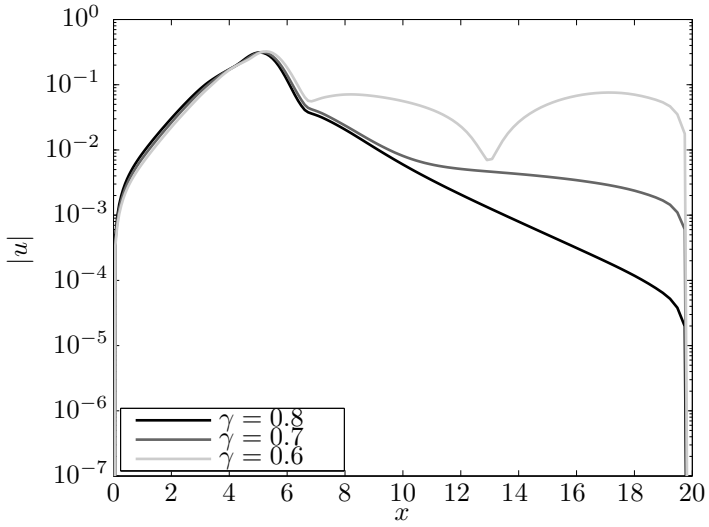

Figure 5.22.: Mode **S4** averaged over $y \in [0, 3.5]$. The stable mode **S4**'s decay along x is influenced at the far-field boundary as γ approaches smaller values. There is a noticeable overshoot at the domain edge for $\gamma \lesssim 0.7$. These simulations were run for parameters $\mathrm{Re} = 300$ at $z_{extr} = 94$, $\Psi = \Psi_U$ ($\chi = 1$), $L_x = 20$, $L_y = 15$, $N_x = 154$, $N_y = 130$ and $x_{\mathrm{half}} = L_x/3$, $y_{\mathrm{half}} = L_y/3$ and BC $\hat{u}(x = 0, y) = 0$.

5.3.3. The Influence of the BCs for $\hat{u}(x = 0, y)$

By changing the boundary condition at $x = 0$ from $\hat{u}(x = 0, y) = 0$ to $\partial^2\hat{u}/\partial x^2(x = 0, y) = 0$ a new antisymmetric mode was recovered that is herein referred to as **A1**. The symmetric modes from Section 5.3.1 have also been analysed under these new boundary conditions and their response to the various parameters did not differ significantly from the already presented results. The plots for them are attached in Appendix C.
The shapes of the **A1** eigenfunctions $|\hat{u}|$, $|\hat{v}|$ and $|\hat{w}|$ are shown in Figure 5.23. They are again normalized by the maximum vector norm ϕ so that relative proportions are visible. Unlike with the symmetric eigenmodes, where the most prominent velocity component was the spanwise $|\hat{w}|$, eigenmode **A1** exhibits a stronger $|\hat{u}|$ component. However, both $|\hat{u}|$ and $|\hat{w}|$ lie in a comparable order of magnitude, only $|\hat{v}|$ shows a much smaller amplitude. Out of all recovered modes, **A1**'s $|\hat{u}|$ and $|\hat{w}|$ clearly peak at the lowest y values. The velocity component $|\hat{v}|$ seems to reach its maximum right around the boundary layer edge. In fact, all velocity components peak in the symmetry plane right in front of the attachment line at $x = 0$. In Figure 5.24 the profiles for different γ are portrayed. All velocity components are plotted for parameter $\gamma = \{0.6, 0.8, 1.0\}$. The components $\hat{u}$ and $\hat{w}$ both have their peaks lifted from the wall as γ increases. $\hat{u}$ additionally develops its second peak to a higher magnitude. The normal component has a tendency to lose some of its energy to the other two components. Those get more concentrated inside the boundary layer with decreasing wavelength. Although there is some movement of the velocities' peaks when altering γ it is bounded relatively well as can be observed in Figure 5.25. Here, the influence of the different base flows is exceptionally small.

To complete the picture of the eigenmodes' characteristics they are presented in a logarithmic plot in Figure 5.26 as a function of x and y. The illustration shows the exponentially decaying nature of the individual modes, which was one of the criterions for identifying a discrete mode. It further highlights the good agreement between the two boundary conditions. Irrespective of the boundary conditions the modes feature the same decay rates and characteristics. Only do they deviate at the location of the boundary where the boundary condition was altered ($x = 0$). One solution is forced to zero, while the other accepts an arbitrary constant value. It is important to point out that there is a small exception where eigenmode **S3** displays a slightly different decay rate in y for the different boundary conditions above $y \approx 5$. This phenomenon has been observed for certain parameter configurations with the remaining modes, too. It is thus not justified to say that changing the boundary condition at $x = 0$ for $\hat{u}(x = 0, y)$ would leave the solution completely unaltered. Still, qualitatively the two configurations preserve the characteristic features of the solutions. Regardless of the BCs at $x = 0$, symmetric modes with almost identical shapes, phase speeds and growth rates could be observed.

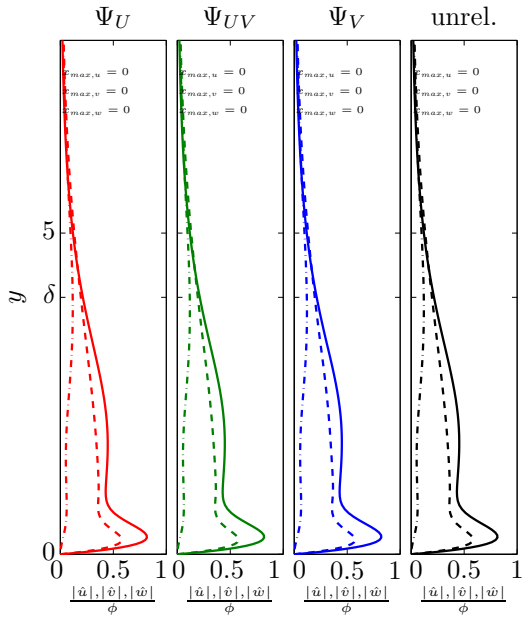

Figure 5.23.: Antisymmetric eigenmode's velocity profiles over y for different Ψ. The velocities are normalized with $\phi = \max||(\hat{u}, \hat{v}, \hat{w})||$ and plotted through their respective maxima. Parameters hereof are Re $= 300$, $\gamma = 0.6$ at $z_{extr} = 94$, $L_x = 20$, $L_y = 15$, $N_x = 147$, $N_y = 120$ and $x_{\text{half}} = L_x/3$, $y_{\text{half}} = L_y/3$ and BC $\partial^2/\partial x^2 \hat{u}(x = 0, y) = 0$.The colors represent: —$\Psi_U$, —$\Psi_{U+V}$, —$\Psi_V$, —unrelaxed. Solid line: $|\hat{u}|$, dashed-dotted line: $|\hat{v}|$, dashed line: $|\hat{w}|$.

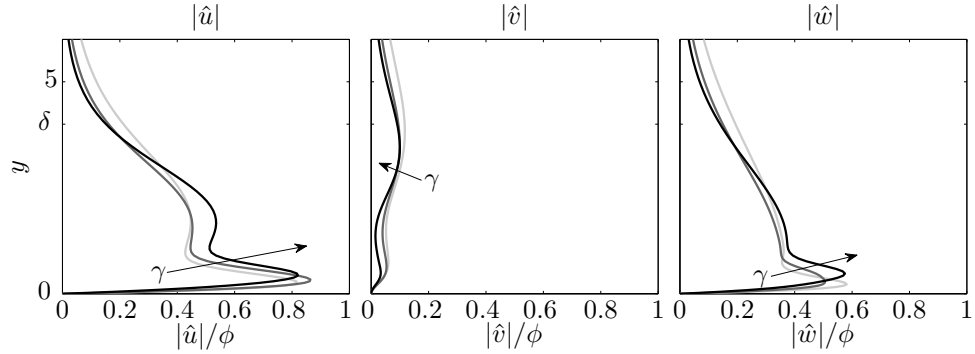

Figure 5.24.: Antisymmetric eigenmode's velocity profiles over y for varying γ and a relaxation with Ψ_U ($\chi = 1$). The velocities are normalized with $\phi = \max||(\hat{u}, \hat{v}, \hat{w})||$ and plotted through their respective maxima. Parameters hereof are Re $= 300$ at $z_{extr} = 94$, $L_x = 20$, $L_y = 15$, $N_x = 147$, $N_y = 120$ and $x_{\text{half}} = L_x/3$, $y_{\text{half}} = L_y/3$ and BC $\partial^2/\partial x^2 \hat{u}(x = 0, y) = 0$.

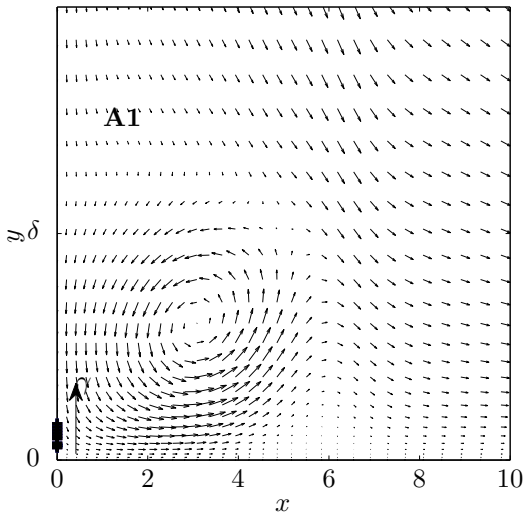

Figure 5.25.: Tracks of the maximum values of $|\hat{w}|$ of the antisymmetric eigenmode under varying γ for different relaxations. Parameters were set to Re = 300 at $z_{extr} = 94$, $L_x = 20$, $L_y = 15$, $N_x = 147$, $N_y = 120$ and $x_{\text{half}} = L_x/3$, $y_{\text{half}} = L_y/3$ and BC $\hat{u}(x = 0, y) = 0$. The colors represent: —Ψ_U, —Ψ_{U+V}, —Ψ_V, —unrelaxed.

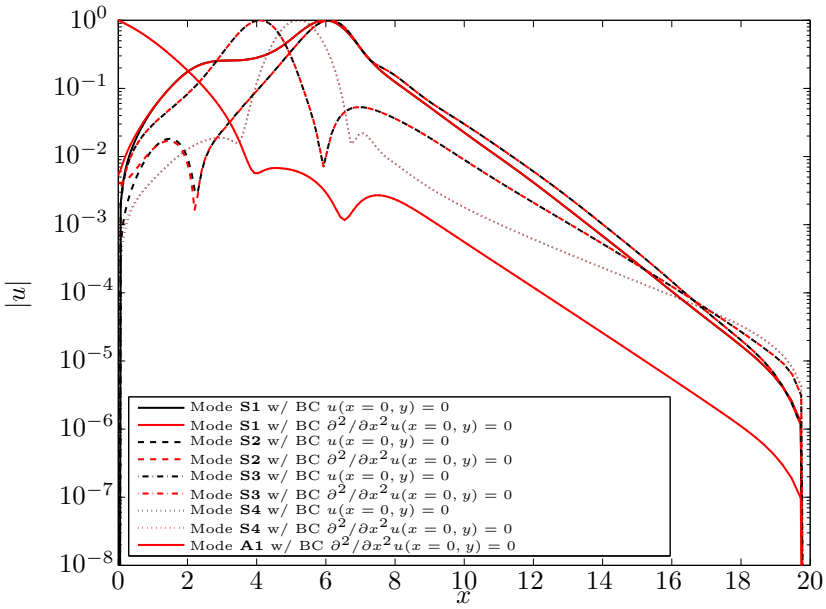

(a)

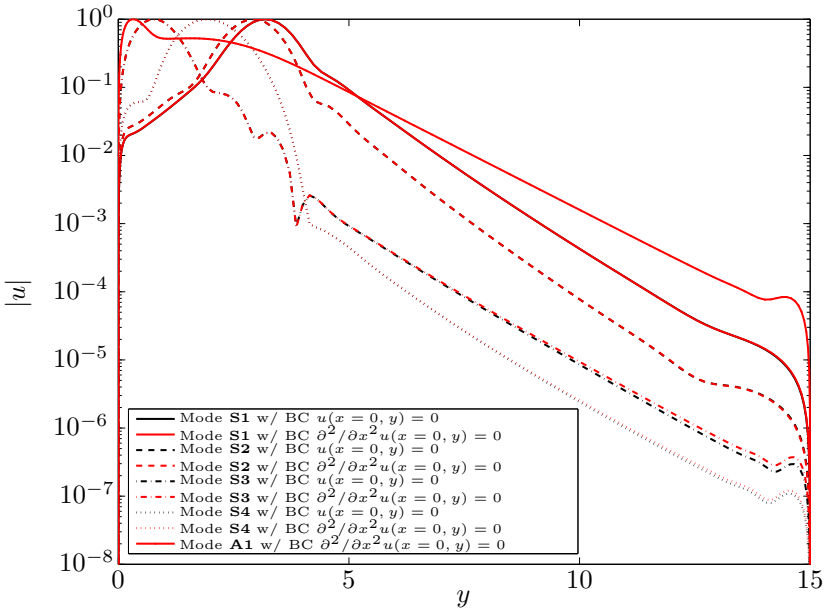

(b)

Figure 5.26.: Logarithmic Plots showing the exponential decay of all modes at $z_{extr} = 94$ for two different boundary conditions and $\gamma = 0.8$. The modes generally agree very well whether $\hat{u}$ is forced to zero or not.

5.3.4. The Influence of the Extraction Location z_{extr}

As mentioned above, the symmetric eigenmodes **S1**-**S4** were recovered further downstream at $z_{extr} = 159$. Looking at their velocity components in Figure 5.27 the differences to the upstream location $z_{extr} = 94$ become evident. Mode **S1** has moved to greater y and now peaks just around δ. The same can be stated about mode **S2** that now has its peak just below the boundary layer edge. The stable modes stay at comparable locations but still have a slight tendency of having moved to higher y compared to the upstream location. Comparable conclusions can also be drawn by looking at the maxima loci in Figure 5.30. Eigenmode **S3**'s $|\hat{u}|$ has moreover developed quite a prominent peak feature closer to the wall.
The results for the upstream location (see Section 5.3.1) regarding the base flow still remain valid. As χ decreases ($\Psi_U \rightarrow \Psi_V$), the maximas tend towards lower x and higher y, except, like above, those of **S4**.
In a general comparison between locations $z_{extr} = 94$ and $z_{extr} = 159$, it seems as though the normal components amplitude slightly rises in expense of the span-wise component's as can be read from Figure 5.28. The dependence on γ seems only to coincide with the upstream location's results for Modes **S2** and **S3**. Although slightly different in shape, their behavior remains practically unchanged. Modes **S1** and **S4**, however, show different tendencies as depicted in Figure 5.29. The former's maximum now seems to drift very little, with the most movement noticeabel in $|\hat{u}|$ and the latter, whereas before it was moving closer to the wall with increasing γ, it now shifts the opposite way, i.e. to higher y values.

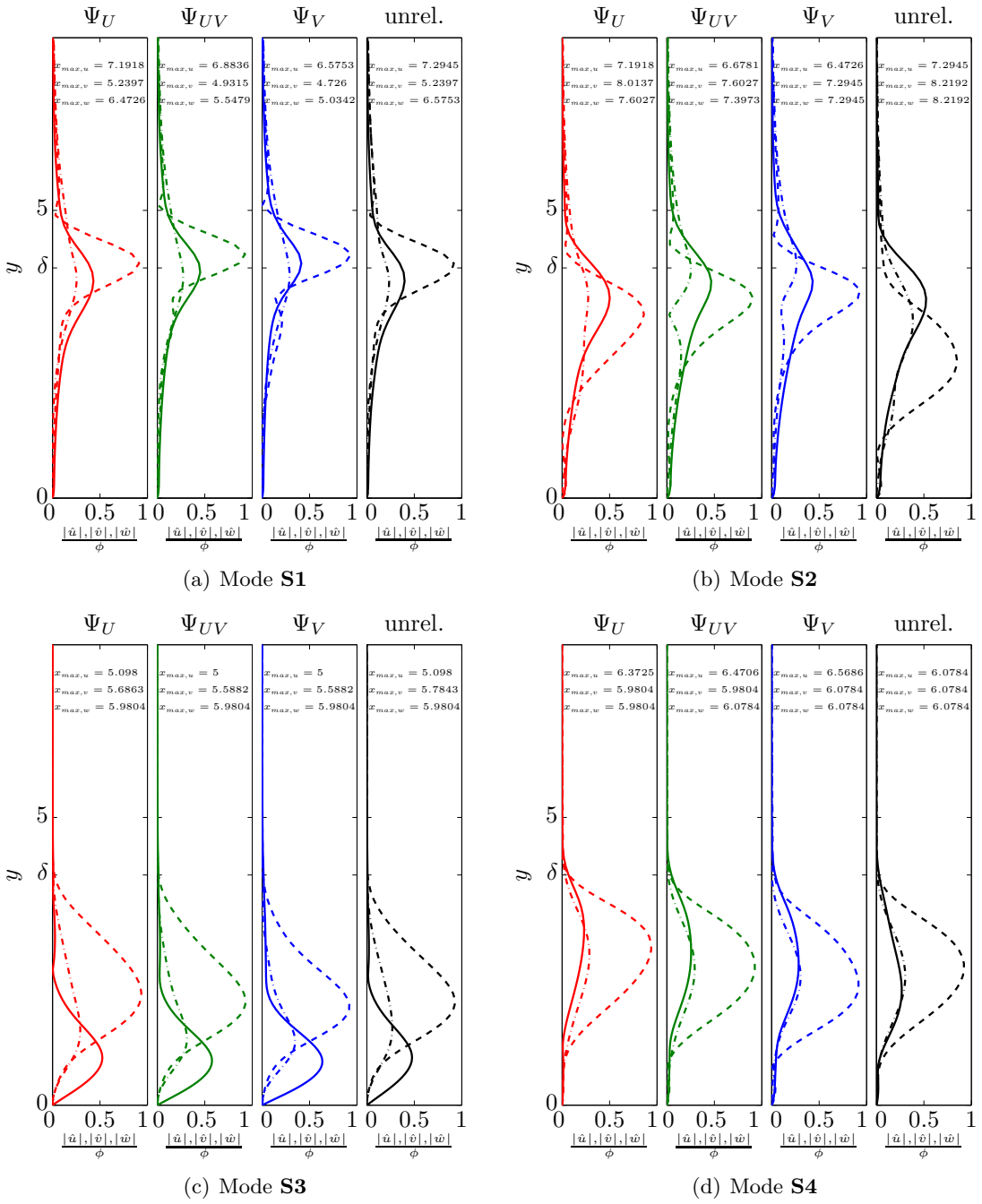

(a) Mode **S1**

(b) Mode **S2**

(c) Mode **S3**

(d) Mode **S4**

Figure 5.27.: Symmetric eigenmodes' velocity profiles over y for different Ψ. The velocities are normalized with $\phi = \max||(\hat{u}, \hat{v}, \hat{w})||$ and plotted through their respective maxima. Parameters hereof are Re $= 300$, $\gamma = 0.6$ at $z_{extr} = 159$, $L_x = 20$, $L_y = 15$, $N_x = 147$, $N_y = 120$ (**S1**, **S2**), $N_x = 154$, $N_y = 130$ (**S3**, **S4**) and $x_{\text{half}} = L_x/3$, $y_{\text{half}} = L_y/3$ and BC $\hat{u}(x = 0, y) = 0$.The colors represent: —Ψ_U, —Ψ_{U+V}, —Ψ_V, —unrelaxed. Solid line: $|\hat{u}|$, dashed-dotted line: $|\hat{v}|$, dashed line: $|\hat{w}|$.

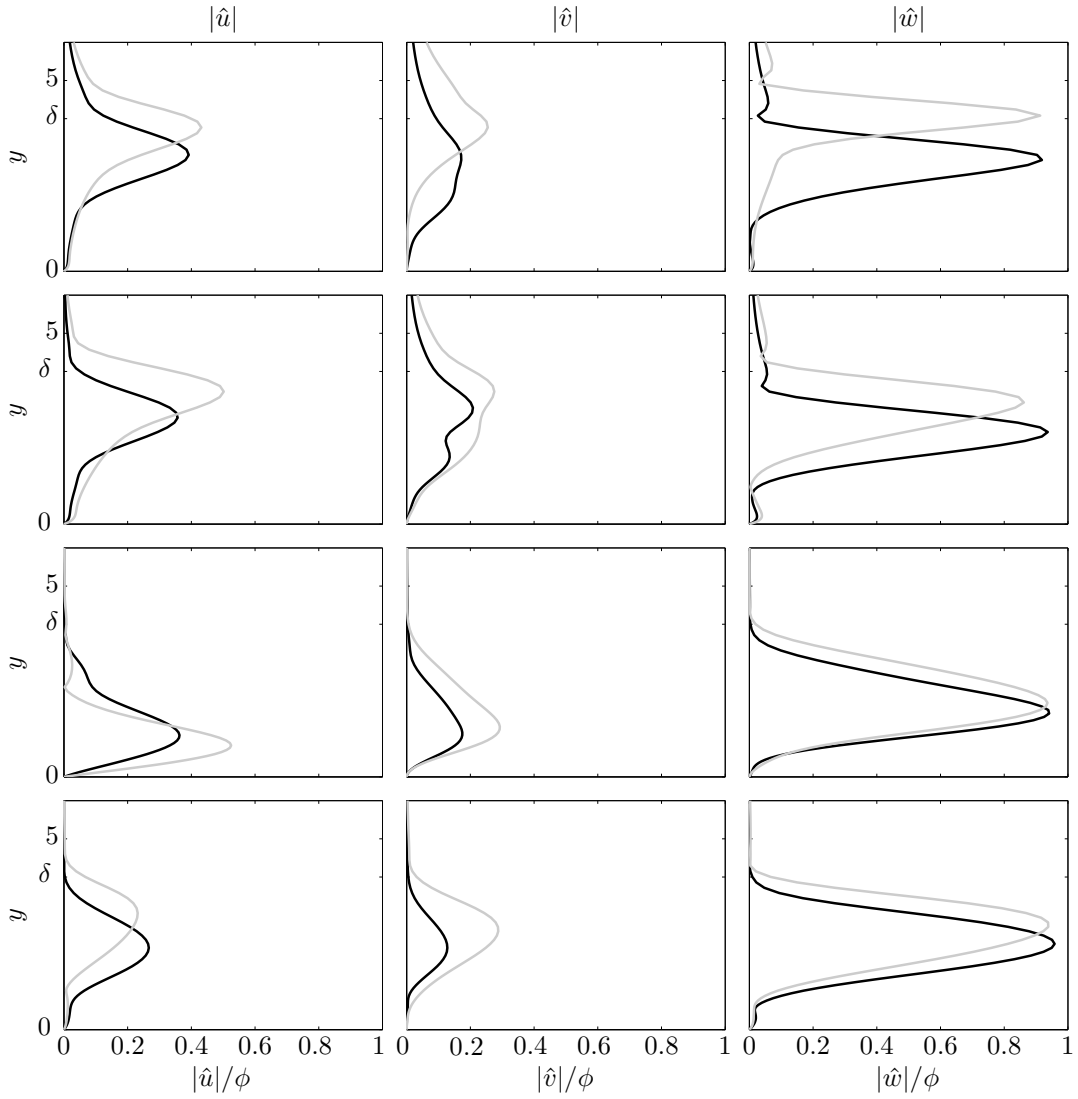

Figure 5.28.: Symmetric eigenmodes' velocity profiles for different z_{extr}. The dark profile represents the location $z_{extr} = 94$, the light profile is further downstream at $z_{extr} = 159$. The velocities are normalized with $\phi = \max||(\hat{u}, \hat{v}, \hat{w})||$ and plotted through their respective maxima. Parameters hereof are Re = 300, Ψ_U, $\gamma = 0.6$, $L_x = 20$, $L_y = 15$, $N_x = 147$, $N_y = 120$ (**S1**, **S2**), $N_x = 154$, $N_y = 130$ (**S3**, **S4**) and $x_{\text{half}} = L_x/3$, $y_{\text{half}} = L_y/3$ and BC $\hat{u}(x = 0, y) = 0$.

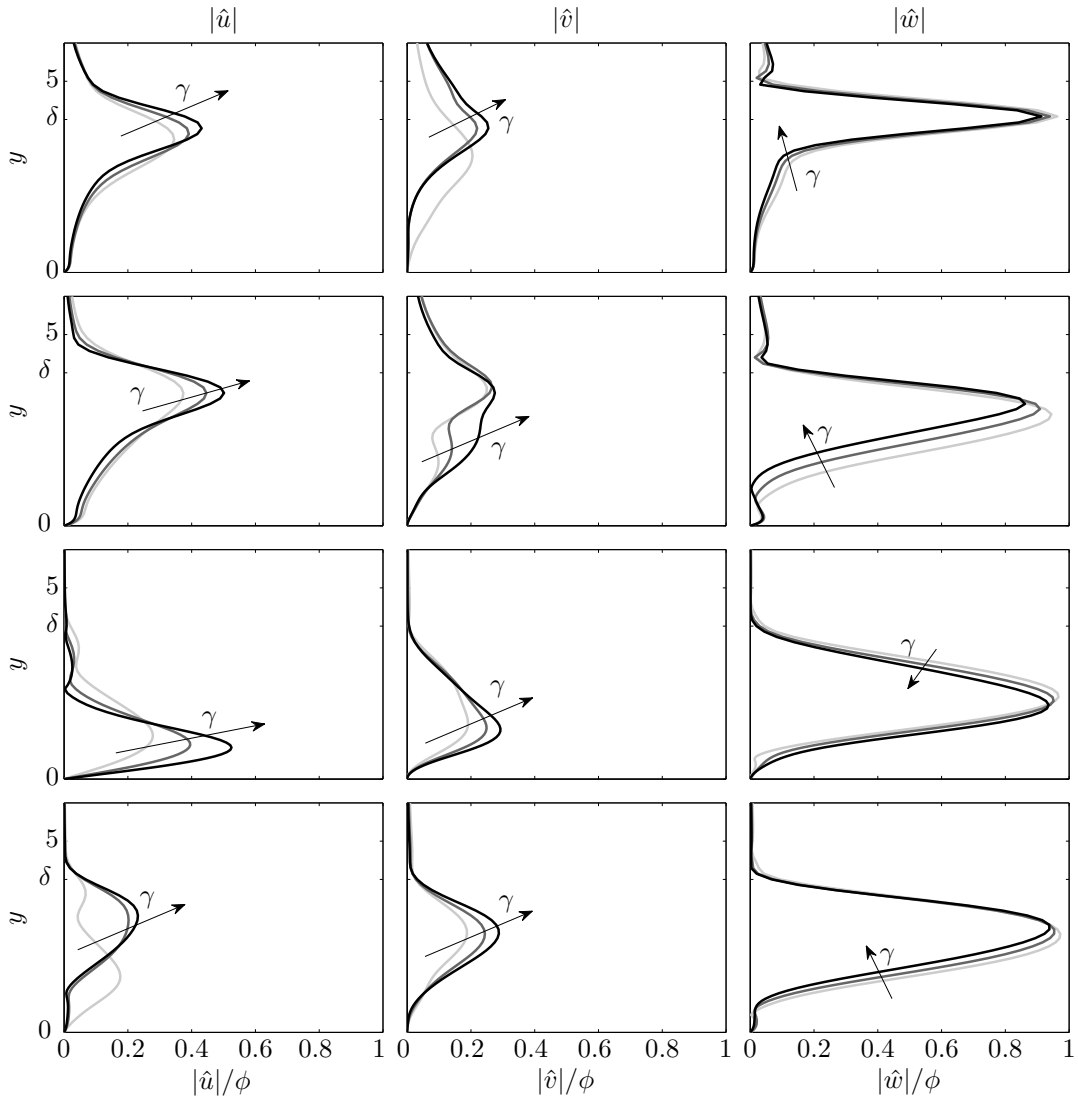

Figure 5.29.: Symmetric eigenmodes' velocity profiles over y for varying γ and a relaxation with Ψ_U ($\chi = 1$). The velocities are normalized with $\phi = \max||(\hat{u}, \hat{v}, \hat{w})||$ and plotted through their respective maxima. Parameters hereof are Re = 300 at $z_{extr} = 159$, $L_x = 20$, $L_y = 15$, $N_x = 147$, $N_y = 120$ (**S1**, **S2**), $N_x = 154$, $N_y = 130$ (**S3**, **S4**) and $x_{\text{half}} = L_x/3$, $y_{\text{half}} = L_y/3$ and BC $\hat{u}(x = 0, y) = 0$.

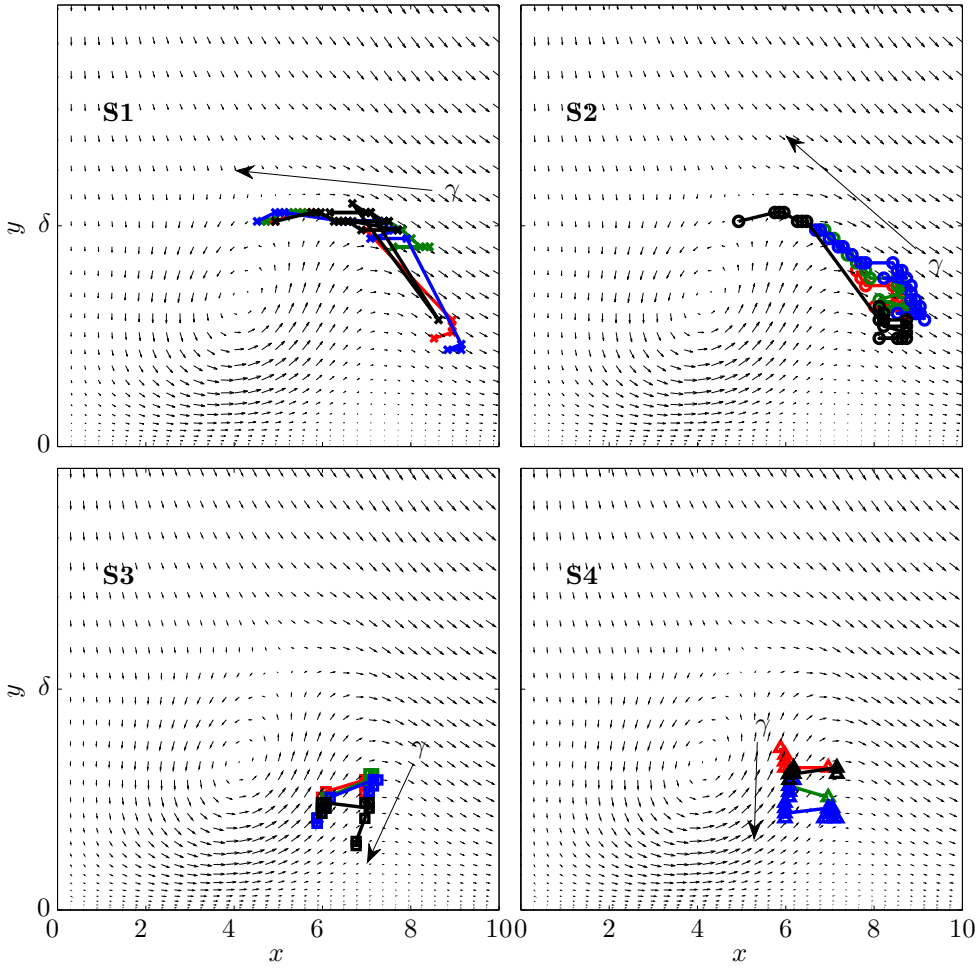

Figure 5.30.: Tracks of the maximum values of the w component of the symmetric eigenmodes under varying γ for different relaxations. Parameters were set to Re = 300 at z_{extr} = 159, $L_x = 20$, $L_y = 15$, $N_x = 147$, $N_y = 120$ (**S1**, **S2**), $N_x = 154$, $N_y = 130$ (**S3**, **S4**) and $x_{\text{half}} = L_x/3$, $y_{\text{half}} = L_y/3$ and BC $\hat{u}(x = 0, y) = 0$. The colors represent: —Ψ_U, —Ψ_{U+V}, —Ψ_V, —unrelaxed.

5.4. Three-Dimensional Illustrations and λ_2 Isosurfaces

For better visualization of the eigenmodes they are shown in a three-dimensional illustration in this section. Each mode is presented in Figures 5.31-5.35 where its velocity components' real parts are displayed over two periods alongside the base flow vortex core which is identified with the λ_2-eigenvalues of the flow (see Appendix A). Additionally there are figures for each mode that display the λ_2 eigenvalue isosurfaces of the base flow with the superimposed respective mode. The λ_2 eigenvalues were computed according to Appendix A. The eigenvalue isosurfaces are colored with the local velocity field. For the unstable modes **A1**, **S1** and **S2** three different amounts of disturbance A are shown. The smallest amount lies in the range in which the disturbance shows itself in the DNS. The two greater values are attached to provide an idea of the disturbance growth over time. The two unstable symmetric modes (Figures 5.37 and 5.38) eventually develop vortices that close on top of the base flow vortex, which itself has broken up. The unstable antisymmetric mode in Figure 5.36 also breaks up the base flow vortex but develops vortices on the outer flank of that original vortex. It also features alternating patched of fast and slow fluid in the symmetry plane above the attachment line. The illustrations of high amplitude $A = 25$ are per se not physically correct because under usual circumstances non-linear effect would have started affecting the flow, creating a different image. They are simply presented to give an idea of what the disturbances themselves look like. Modes **S3** (Figure 5.39) and **S4** (Figure 5.40) since they are of damped nature are only presented here superimposed on the base flow with $A = 0.01$. Blue always corresponds to the respective minimum velocity and red to the respective maximum. In case of the unstable modes these colors do not relate the velocity field over the different amplitude isosurfaces. In fact, the minimum normalized velocity for both $A = 0.01$ and $A = 0.1$ lies around zero, whereas for $A = 25$ it lies near -1. The coloring was chosen this way because the difference in velocity magnitude is in fact three orders of magnitude which does not allow for fine enough gradients at low amplitudes A.

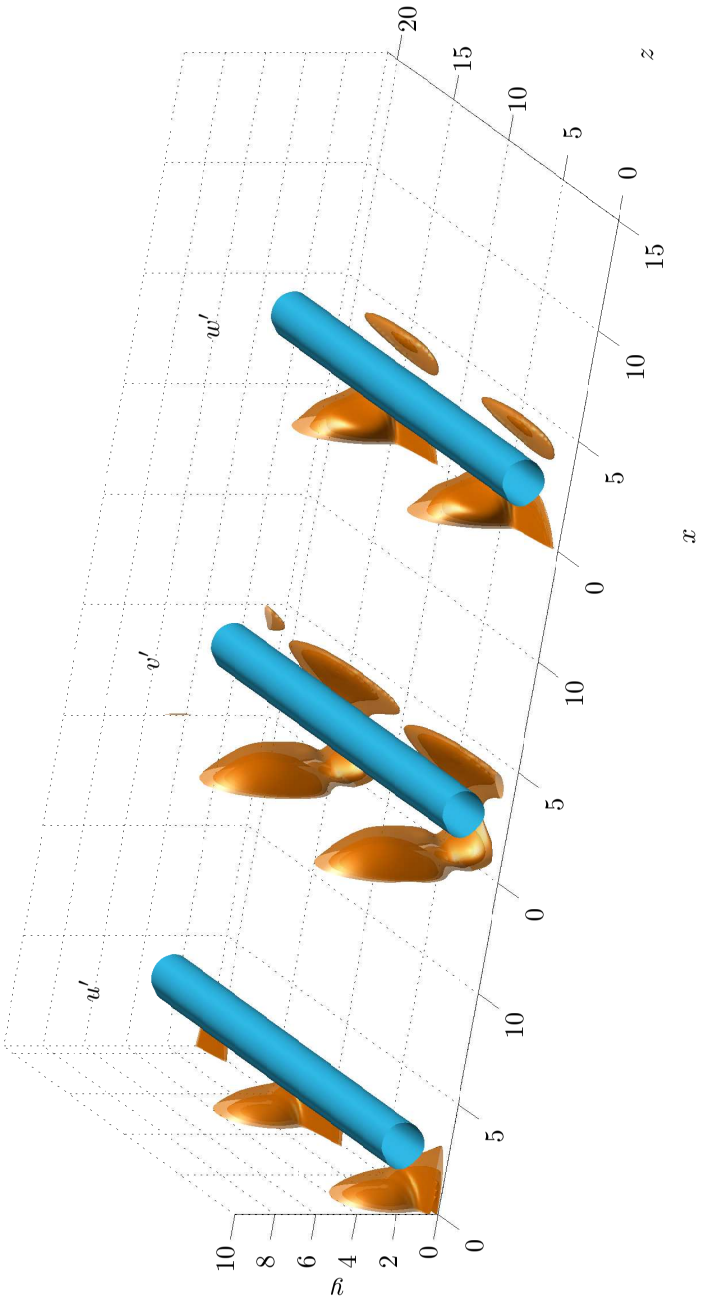

Figure 5.31.: Three-dimensional illustration of the asymmetric mode's **A1** velocity components for a wavenumber of $\gamma = 0.6$. They are individually normalized and isosurface of $\{0.25, 0.35, 0.45, 0.55, 0.65\}$ are shown. The baseflow vortex $\lambda_2 = -0.001$ isosurface is shown in blue. Parameters are $\mathrm{Re} = 300$ at $z_{extr} = 94$, $L_x = 20$, $L_y = 15$, $N_x = 147$, $N_y = 120$ and $x_{\mathrm{half}} = L_x/3$, $y_{\mathrm{half}} = L_y/3$ and BC $\partial^2/\partial x^2 \hat{u}(x = 0, y) = 0$.

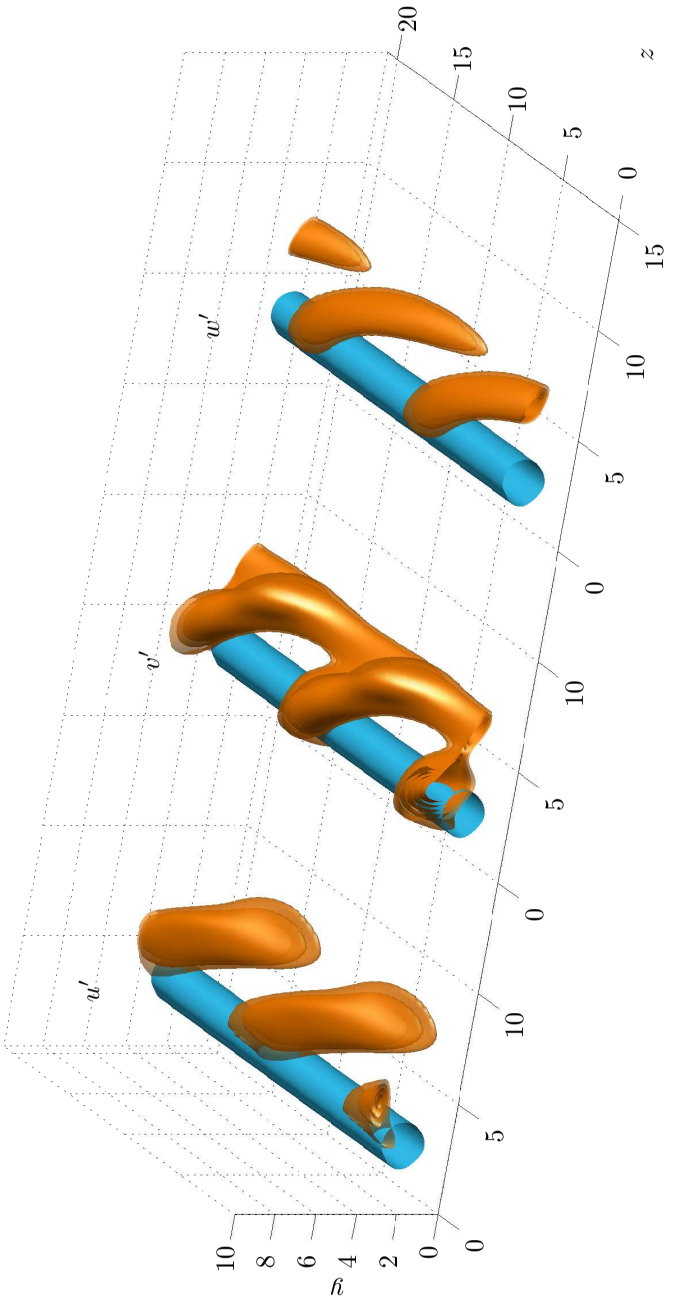

Figure 5.32.: Three-dimensional illustration of the symmetric mode's **S1** velocity components for a wavenumber of $\gamma = 0.6$. They are individually normalized and isosurface of $\{0.25, 0.35, 0.45, 0.55, 0.65\}$ are shown. The baseflow vortex $\lambda_2 = -0.001$ isosurface is shown in blue. Parameters are $\mathrm{Re} = 300$ at $z_{extr} = 94$, $L_x = 20$, $L_y = 15$, $N_x = 147$, $N_y = 120$ and $x_{\mathrm{half}} = L_x/3$, $y_{\mathrm{half}} = L_y/3$ and BC $\hat{u}(x = 0, y) = 0$.

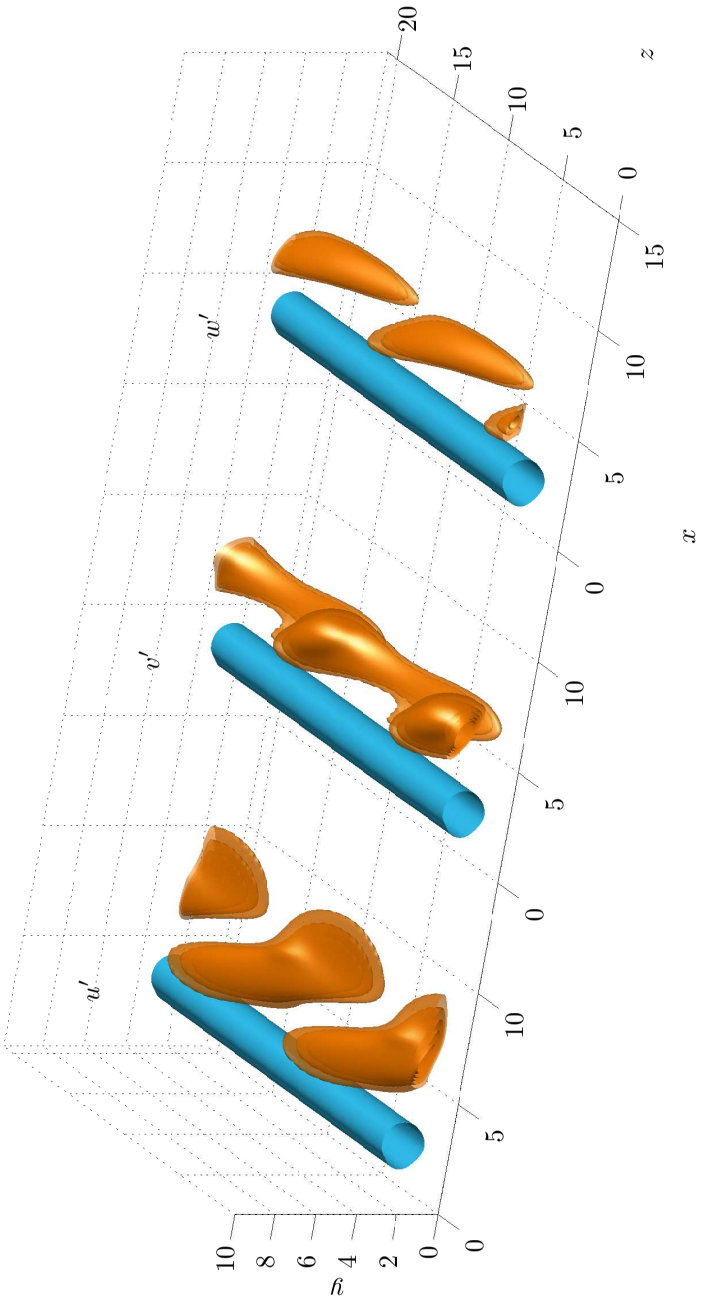

Figure 5.33.: Three-dimensional illustration of the symmetric mode's **S2** velocity components for a wavenumber of $\gamma = 0.6$. They are individually normalized and isosurface of $\{0.25, 0.35, 0.45, 0.55, 0.65\}$ are shown. The baseflow vortex $\lambda_2 = -0.001$ isosurface is shown in blue. Parameters are $\mathrm{Re} = 300$ at $z_{extr} = 94$, $L_x = 20$, $L_y = 15$, $N_x = 147$, $N_y = 120$ and $x_{\mathrm{half}} = L_x/3$, $y_{\mathrm{half}} = L_y/3$ and BC $\hat{u}(x = 0, y) = 0$.

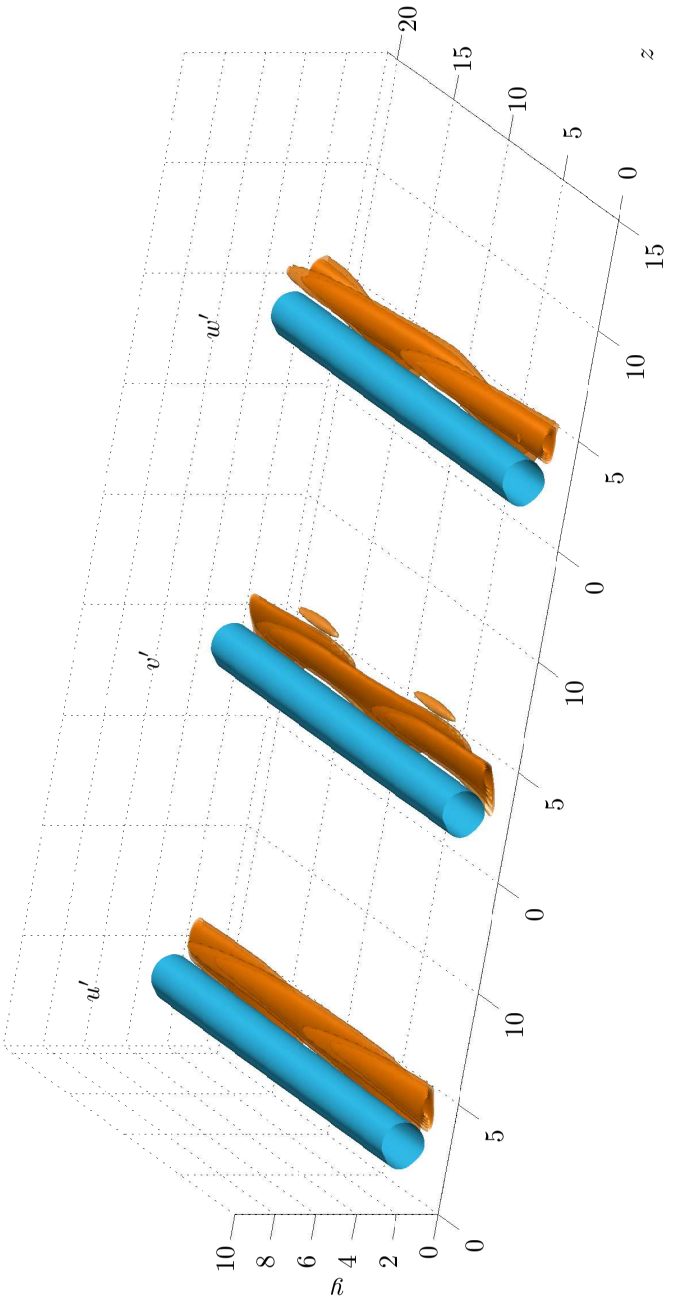

Figure 5.34.: Three-dimensional illustration of the symmetric mode's **S3** velocity components for a wavenumber of $\gamma = 0.6$. They are individually normalized and isosurface of $\{0.25, 0.35, 0.45, 0.55, 0.65\}$ are shown. The baseflow vortex $\lambda_2 = -0.001$ isosurface is shown in blue. Parameters are $\mathrm{Re} = 300$ at $z_{extr} = 94$, $L_x = 20$, $L_y = 15$, $N_x = 147$, $N_y = 120$ and $x_{\mathrm{half}} = L_x/3$, $y_{\mathrm{half}} = L_y/3$ and BC $\hat{u}(x = 0, y) = 0$.

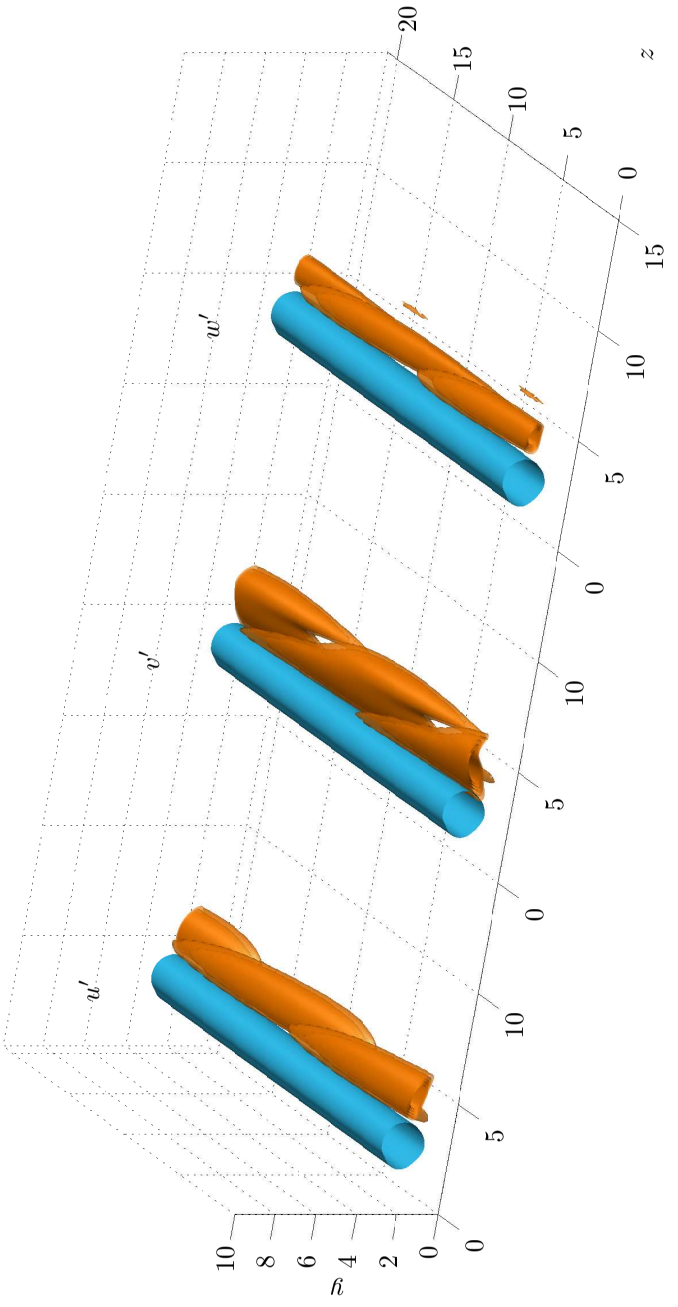

Figure 5.35.: Three-dimensional illustration of the symmetric mode's **S4** velocity components for a wavenumber of $\gamma = 0.6$. They are individually normalized and isosurface of $\{0.25, 0.35, 0.45, 0.55, 0.65\}$ are shown. The baseflow vortex $\lambda_2 = -0.001$ isosurface is shown in blue. Parameters are $\mathrm{Re} = 300$ at $z_{extr} = 94$, $L_x = 20$, $L_y = 15$, $N_x = 147$, $N_y = 120$ and $x_{\mathrm{half}} = L_x/3$, $y_{\mathrm{half}} = L_y/3$ and BC $\hat{u}(x = 0, y) = 0$.

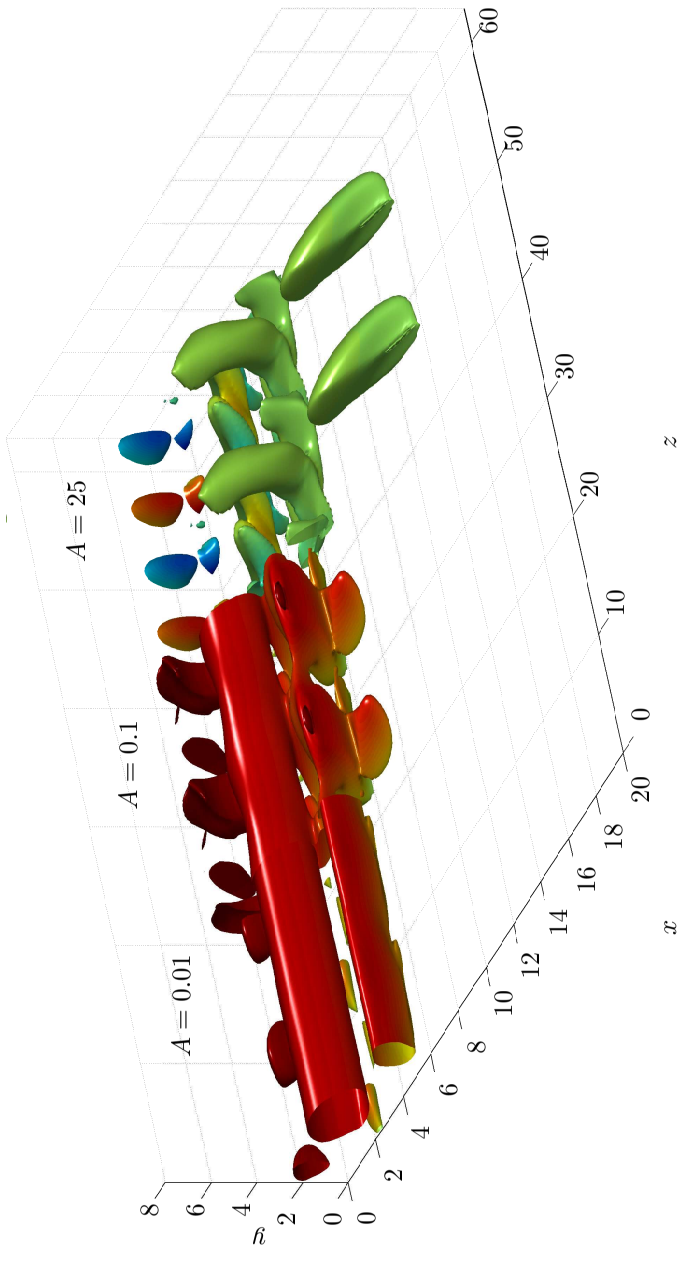

Figure 5.36.: $\lambda_2 = -0.0002$ eigenvalue isosurfaces of the base flow with superimposed disturbance **A1** for different amounts A of disturbance over a total of six periods. Parameters are $\gamma = 0.6$, $\mathrm{Re} = 300$ at $z_{extr} = 94$, $L_x = 20$, $L_y = 15$, $N_x = 147$, $N_y = 120$ and $x_{\mathrm{half}} = L_x/3$, $y_{\mathrm{half}} = L_y/3$ and BC $\partial^2/\partial x^2 \hat{u}(x = 0, y) = 0$.

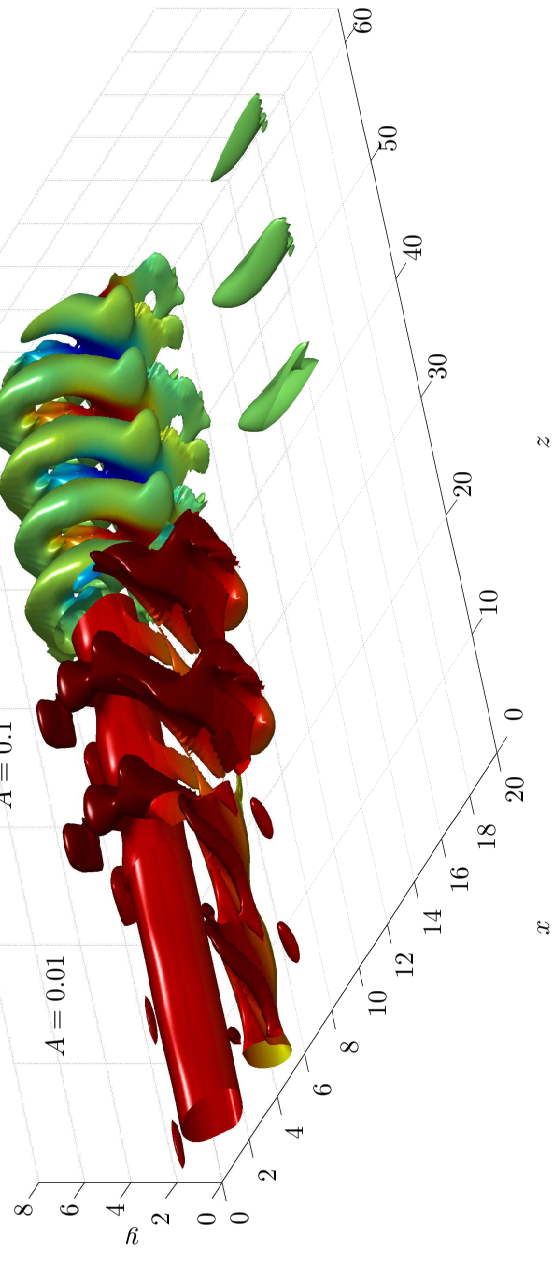

Figure 5.37.: $\lambda_2 = -0.0002$ eigenvalue isosurfaces of the base flow with superimposed disturbance **S1** for different amounts A of disturbance over a total of six periods. Parameters are $\gamma = 0.6$, $\mathrm{Re} = 300$ at $z_{extr} = 94$, $L_x = 20$, $L_y = 15$, $N_x = 147$, $N_y = 120$ and $x_{\mathrm{half}} = L_x/3$, $y_{\mathrm{half}} = L_y/3$ and BC $\hat{u}(x = 0, y) = 0$.

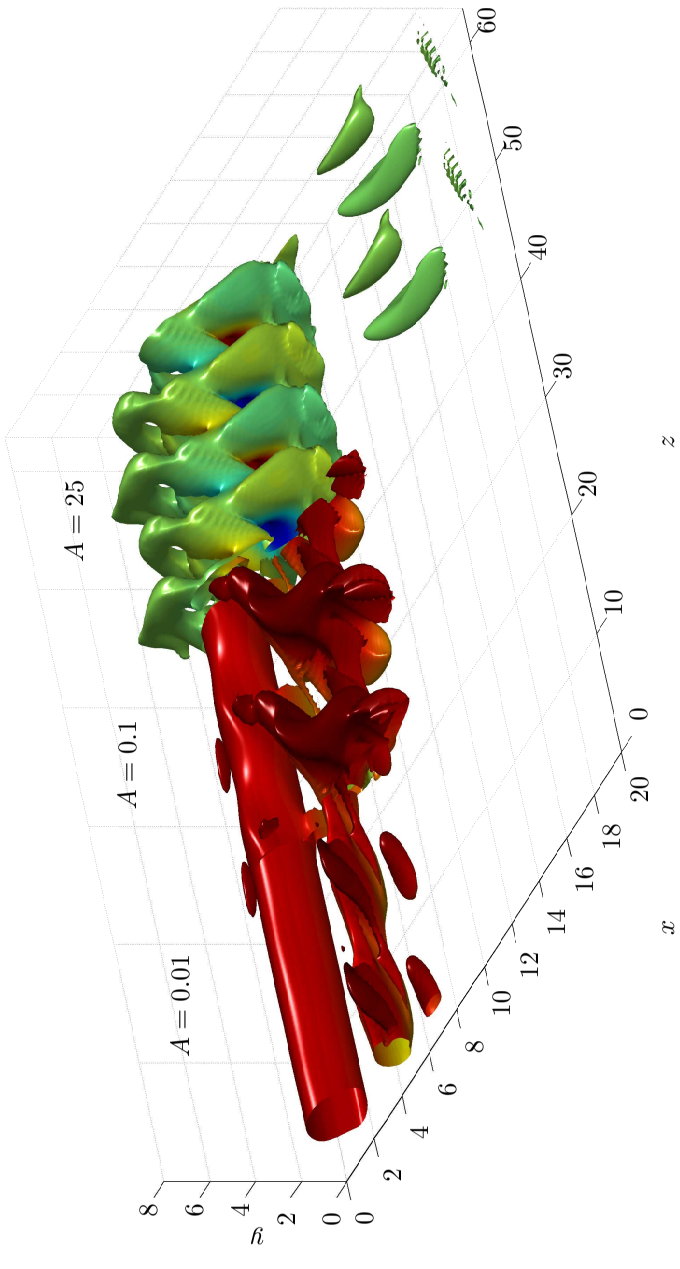

Figure 5.38.: $\lambda_2 = -0.0002$ eigenvalue isosurfaces of the base flow with superimposed disturbance **S2** for different amounts A of disturbance over a total of six periods. Parameters are $\gamma = 0.6$, $\mathrm{Re} = 300$ at $z_{extr} = 94$, $L_x = 20$, $L_y = 15$, $N_x = 147$, $N_y = 120$ and $x_{\mathrm{half}} = L_x/3$, $y_{\mathrm{half}} = L_y/3$ and BC $\hat{u}(x = 0, y) = 0$.

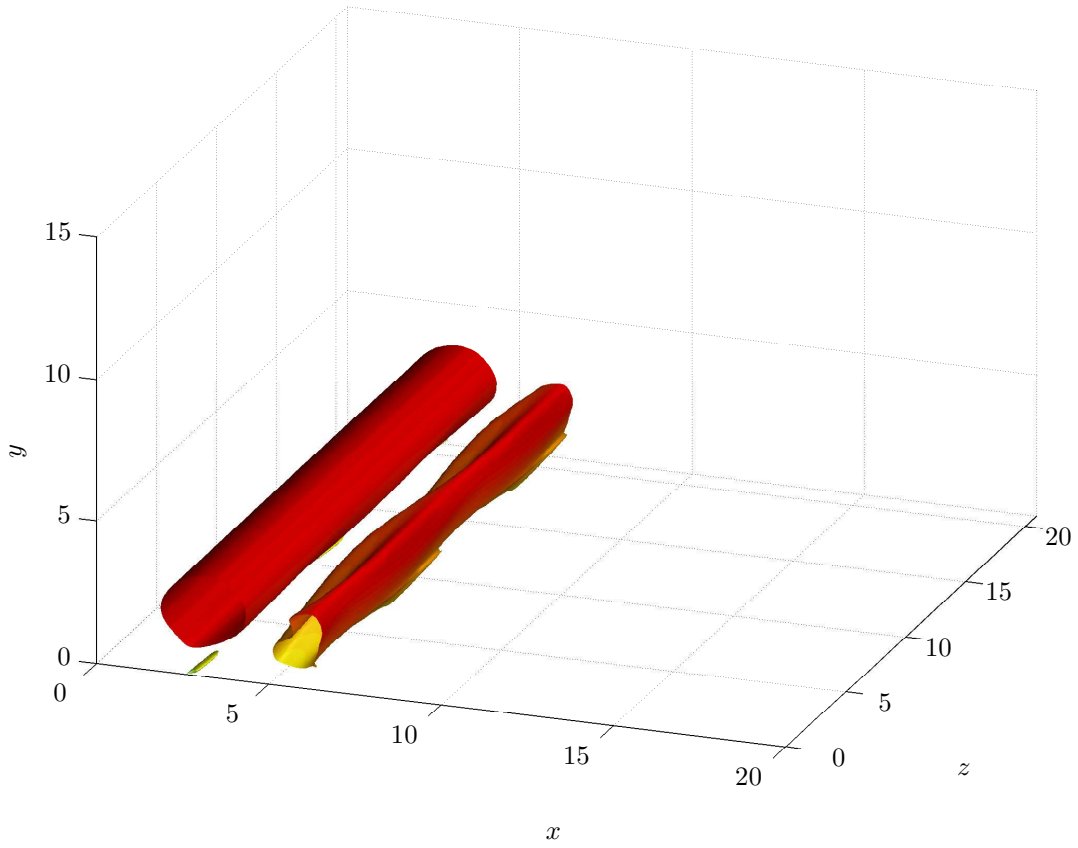

Figure 5.39.: $\lambda_2 = -0.0002$ eigenvalue isosurfaces of the base flow with superimposed disturbance **S3** ($A = 0.01$) over two periods. Parameters are $\gamma = 0.6$, Re $= 300$ at $z_{extr} = 94$, $L_x = 20$, $L_y = 15$, $N_x = 147$, $N_y = 120$ and $x_{\text{half}} = L_x/3$, $y_{\text{half}} = L_y/3$ and BC $\hat{u}(x = 0, y) = 0$.

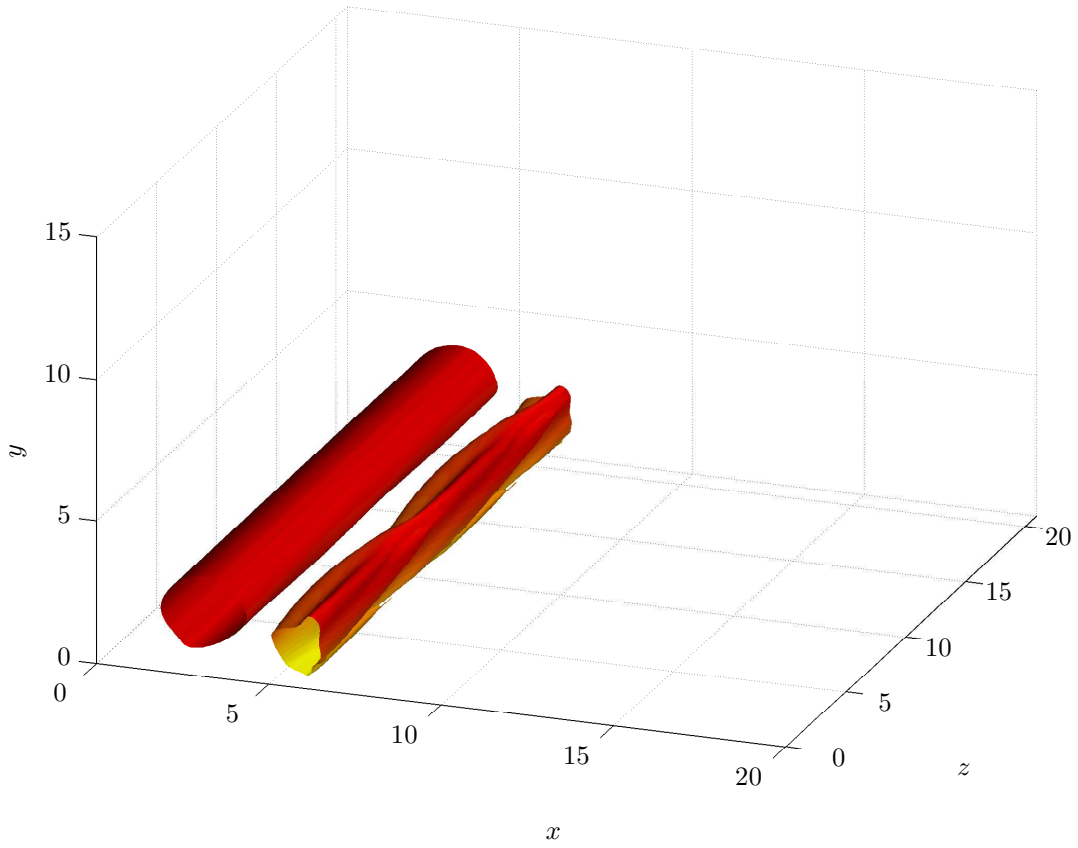

Figure 5.40.: $\lambda_2 = -0.0002$ eigenvalue isosurfaces of the base flow with superimposed disturbance **S4** ($A = 0.01$) over two periods. Parameters are $\gamma = 0.6$, Re $= 300$ at $z_{extr} = 94$, $L_x = 20$, $L_y = 15$, $N_x = 147$, $N_y = 120$ and $x_{\text{half}} = L_x/3$, $y_{\text{half}} = L_y/3$ and BC $\hat{u}(x = 0, y) = 0$.

5.5. Comparison with Wintergerste [39]

This chapter compares the results of this thesis by results previously acquired in literature. In particular, it gives a comparison to the eigenmodes derived in the dissertation by T. Wintergerste [39].

In his work he solved a bi-global stability problem for the late states of transition of a three-dimensional boundary layer. His base flow consisted of co-rotating crossflow vortices with a small disturbance. In his results he identified three distinct unstable modes, which he could track in the spectrum. He more thoroughly described the two most unstable ones shown in Figure 5.41, which were labeled Mode I and Mode II. While his initial problem is not the same as the one dealt with in this present thesis, it is still apparent that the two solution show some similarities. Wintergerste's Mode I shows a qualitatively similar shape as does Mode **S1** herein. Moreover, Wintergerste's Mode II shows an even closer resemblance to damped Mode **S3**. Evidently, the circumstances of the two sources are not in any way directly comparable as none of the parameters agree and neither do the coordinate system orientations. However, it would be interesting to qualitatively compare the two results, since the flow in any case originates in front of the attachment line from where it travels along the streamlines onto the wing surface. Given a small enough disturbance at the attachment line, the flow might stay laminar or in transition until it reaches that downstream location and perhaps preserve its modal growth. Such a detailed analysis will not be conducted here, since it would exceed the scope of the thesis, rather this chapter should serve as a motivation for further investigation.

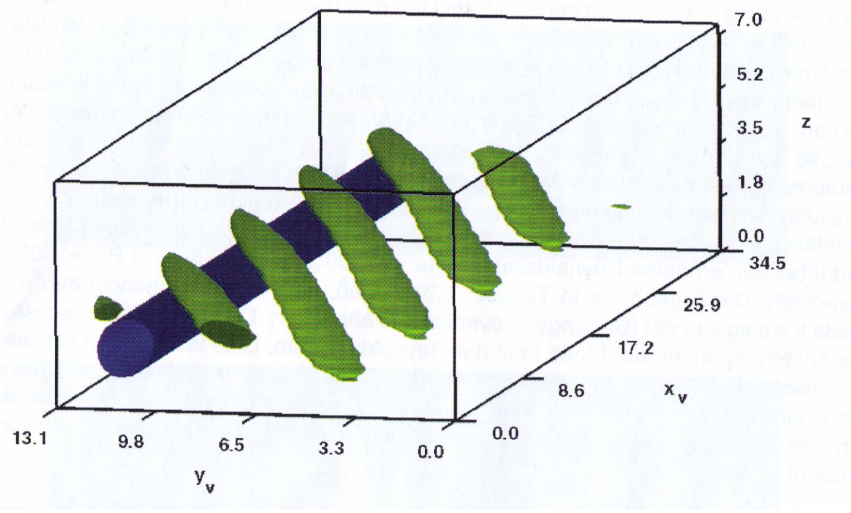

(a) Mode I

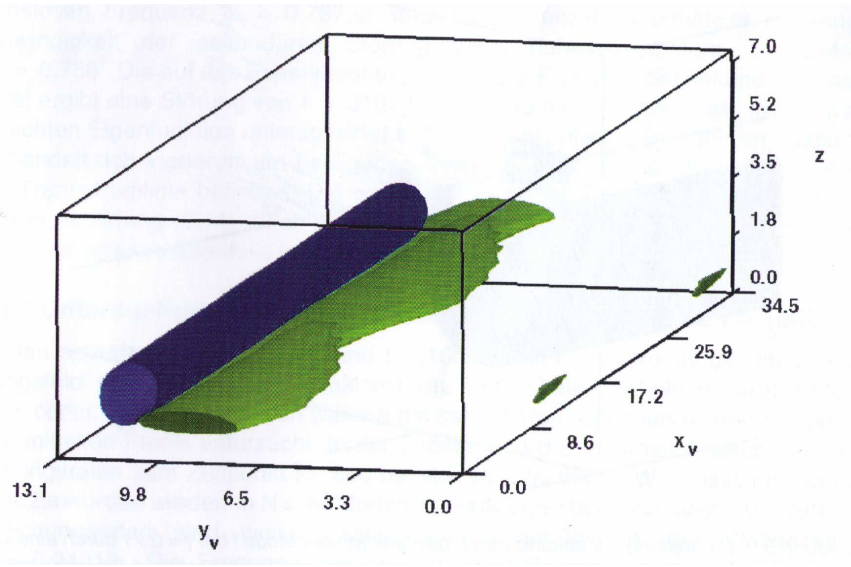

(b) Mode II

Figure 5.41.: Modes identified by Wintergerste, 2002 [39] from a bi-global stability problem of the crossflow region on a wing.

6. Conclusion and Outlook

6.1. Summary and Discussion

In this thesis the attachment line (in-)stability of the swept Hiemenz boundary-layer on swept wings was analyzed at a Reynolds number of $\mathrm{Re} = 300$, which exhibits breakdown to turbulence through modal growth in DNS. The boundary layer is known to be linearly critically stable at $\mathrm{Re}_{\mathrm{lin,crit}} = 583.1$ and it has been shown to break down for $\mathrm{Re} \approx 250$ in experiments.

From the DNS a base flow $\underline{U} = \underline{U}(x, y)$ was extracted. The SHBL, classically independent of the span-wise coordinate z, is superimposed with primary counter-rotating vortices upon which secondary modal growth occurs, invalidating that independence. New stability equations were derived under the assumption of span-wise independence for the new DNS base flow which has a new global dependence on x. Treatment of the base flow was done in two ways. Its span-wise gradient was either neglected in a "weakly non-parallel" assumption or it was eliminated by modifying (relaxing) the base flow. The stability equations were then reformulated into a secondary two-dimensional eigenvalue problem and implemented into the already existing code framework.

The code was optimized in terms of a new differentiation scheme which now is compatible with non-equidistant grids. The implementation of the boundary conditions into the eigenvalue problem matrices was changed from element-wise accessing to a multiplication by and addition of stencils. The code benefited from these changes with a speed-up of 30 percent. Additionally, eight recurring variables in the stability equations can be either globally stored in memory or locally recomputed, depending on the desired performance of the code.

The secondary eigenvalue problem's convergence with respect to the numerical parameters N_x, N_y and L_x showed that while it converges monotonically in y it exhibits an optimal number of grid points in x above which the solution diverges. The optimal resolution for a domain size of $L_x = 15 \times L_y = 15$ was found to be $N_x = 150 \times N_y = 150$. The solution's dependence on the domain size L_x showed very little variance in terms of the eigenvalues, which for values of $L_x \in [15, 25]$ agreed up to four decimal points. Also, the velocity profiles showed good agreement for the different L_x. Only where the gradients were high, was the effect of the ratio N_x/L_x visible. A final $L_x = 20$ was chosen to prevent a forcing of the boundary condition upon the velocities and allow for a natural decay. The eigenvalue problem was found to be a memory-limited problem and thus the resolutions had to be set to $N_x = 154 \times N_y = 130$ on a 64GB cluster (VENANT) and to $N_x = 147 \times N_y = 120$ on a 46GB cluster (EIGER) for a final domain size of $L_x = 20 \times L_y = 15$.

The solution of the secondary EVP identified five distinct discrete modes. Four of those modes are of symmetric and one is of anti-symmetric type. All of the modes feature exponential decay

of the velocities in both x and y. The recovered modes are qualitatively independent of the base flow treatment (parameter Ψ). Whether the employed base flow was previously relaxed or unprocessed, the same modes were able to be identified. Generally, the solutions obtained from a base flow derived from Ψ_U agrees best with the unrelaxed base flow.
The symmetric modes showed no dependence of the boundary conditions at $x = 0$, while the anti-symmetric mode **A1** was only retrieved for BCs $\partial^2\hat{u}/\partial x^2(x = 0, y)$.
The symmetric modes were also recovered at two locations, one location at $z = 94$ and one downstream at $z = 159$. The modes showed a tendency of being located at higher x and y at the downstream location. While upstream mode **S1** showed the highest growth rates of the symmetric modes, at the downstream location **S2** now features the highest growth rates for certain parameter configurations.
In the range of $\gamma \in [0.1, 1.2]$ at least one of the modes **S1**, **S2** and **A1** shows unstable behavior (positive growth rates). **A1** shows the highest growth rate of all at around $\gamma = 0.5$. While modes **S3**, **S4** and **A1** do not change location much for different γ, modes **S1** and **S2** travel a significant distance from the outer flank of the base flow vortex to its top. This behavior was also responsible for the bad numerical convergence of the solution for $\gamma \leq 0.3$ for which the domain size $L_x = 20$ proved to be too small.
The complete dependence on physical parameters of the modes is also summarized in Table 6.1.

The modes were then compared to modes found in the later stages of crossflow instability on the swept wing by Wintergerste [39], who identified two modes I and II which share similar characteristics with the symmetric modes derive in this thesis.

The goal of explaining the breakdown of the streaks in the SHBL at Re= 300 as seen in DNS was thus reached. By finding three solutions that provide proof of unstable modal growth within the flow also the experimental critical Reynolds number $\mathrm{Re}_{\mathrm{exp,crit}} \approx 250$ has been significantly approached.

Table 6.1.: Summary of the results. The dependence of the solutions on the various physical parameters is summarized.

	Mode	Ψ (χ)	γ	BCs $\hat{u}(x=0,y)$	z_{extr}
Spectrum	**S1**	$c_r \approx$ constant, $c_i \downarrow$ as $\chi \uparrow$	c_r constant for $\gamma > 0.3$, soln. diverges below $\gamma \approx 0.3$	not significantly affected in converged part	c_r comparable (slighty less), $c_i \downarrow$ as $z \uparrow$
	S2	$c_r \uparrow$ as $\chi \uparrow$, $c_i \downarrow$ as $\chi \uparrow$	$c_r \uparrow$ as $\gamma \uparrow$, c_i peaks at $\gamma \approx 0.35$, soln. diverges below $\gamma \approx 0.3$	not significantly affected in converged part	c_r comparable (slightly less), $c_i \uparrow$ as $z \uparrow$
	S3	$c_r \downarrow$ as $\chi \uparrow$, $c_i \downarrow$ as $\chi \uparrow$	$c_r \uparrow$ as $\gamma \uparrow$, c_i peaks at $\gamma \approx 0.35$	not significantly affected in converged part	no significant changes
	S4	$c_r \approx$ constant, $c_i \downarrow$ as $\chi \uparrow$	$c_r \uparrow$ as $\gamma \uparrow$, c_i peaks at $\gamma \in [0.8, 1.0]$ (dep. on Ψ), soln. diverges below $\gamma \approx 0.6$	not significantly affected in converged part	shifts peak c_i to lower γ for $\chi = 0$
	A1	c_r and c_i match for all Ψ for $\gamma > 0.5$, all Ψ deviate from unrel. BF	$c_r \uparrow$ as $\gamma \uparrow$, c_i peaks at $\gamma \approx 0.5$, $c_r < 0$ for $\gamma < 0.4$	only present for $\partial^2/\partial x^2 \hat{u}(x=0,y)$	N/A
Eigenfunctions	**S1**	maxima move towards BL edge and symmetry plane as $\chi \downarrow$	$\lvert\hat{w}\rvert \downarrow$ and $\lvert\hat{u}\rvert \uparrow$, $\lvert\hat{v}\rvert \uparrow$ as $\gamma \uparrow$, travels towards BL edge and to lower x as $\gamma \uparrow$	not significantly affected in converged part	peaks shift to higher y as $z \uparrow$, almost constant y loc. for diff. γ and $\lvert\hat{w}\rvert \downarrow$ and $\lvert\hat{u}\rvert \uparrow$, $\lvert\hat{v}\rvert \uparrow$ as $z \uparrow$
	S2	maxima move towards BL edge and symmetry plane as $\chi \downarrow$	$\lvert\hat{w}\rvert \downarrow$ and $\lvert\hat{u}\rvert \uparrow$, $\lvert\hat{v}\rvert \uparrow$ as $\gamma \uparrow$, travels towards BL edge and to lower x as $\gamma \uparrow$	not significantly affected in converged part	peaks shift to higher y and $\lvert\hat{u}\rvert \uparrow$, $\lvert\hat{v}\rvert \uparrow$ as $z \uparrow$
	S3	maxima move towards BL edge and symmetry plane as $\chi \downarrow$	$\lvert\hat{w}\rvert \downarrow$ and $\lvert\hat{u}\rvert \uparrow$, $\lvert\hat{v}\rvert \uparrow$ as $\gamma \uparrow$, travels towards wall and to lower x as $\gamma \uparrow$	not significantly affected in converged part	comparable with tendency to peak at higher y and $\lvert\hat{u}\rvert \uparrow$, $\lvert\hat{v}\rvert \uparrow$ as $z \uparrow$, $\lvert\hat{u}\rvert$ peak closer at wall
	S4	maxima move towards wall and symmetry plane as $\chi \downarrow$	$\lvert\hat{w}\rvert \downarrow$ and $\lvert\hat{u}\rvert \uparrow$, $\lvert\hat{v}\rvert \uparrow$ as $\gamma \uparrow$, travels towards wall and to lower x as $\gamma \uparrow$	not significantly affected in converged part	comparable with tendency to peak at higher y as $z \uparrow$ and almost constant y loc. for diff. γ and $\lvert\hat{u}\rvert \uparrow$, $\lvert\hat{v}\rvert \uparrow$ as $z \uparrow$
	A1	maxima always at $x = 0$ no significant dependence on Ψ	more concentrated inside BL as $\gamma \uparrow$, maxima shift towards BL edge as $\gamma \uparrow$	only present for $\partial^2/\partial x^2 \hat{u}(x=0,y)$	N/A

6.2. Outlook and Future Work

With the obtained results a foundation was laid for the characterization of bi-global secondary stability theory. However, there remain some improvements that need closer attention. For example, the limited domain size distorted some of the results for low wavenumbers γ. For completing the results in that parameter range simulations would need re-running on an adequate domain with adequate discretization in consideration, of course, of memory.

The work can be extended to include a broader parameter study that includes additional values such as a range of Reynolds numbers above and below the value of Re= 300 in this thesis. This would provide the possibility of constructing a bi-global stability map for secondary instability of the SHBL. Another extension, that was only briefly touched herein, provides itself through a possible application of wall-normal suction described by the parameter κ that would alter the breakdown process.

Despite careful investigation there remains the question of additional solutions which have not been uncovered over the span of the present work. Undiscovered solutions in the present flow may potentially show a prevailing role in the secondary (in)stability of the swept Hiemenz boundary layer for other parameters (e.g. higher Re numbers) as they emerge from the spectrum.

Short reference was made to [39] in Section 5.5 in which the idea was brought up of comparing those solutions to the present ones. Possible analysis that can be conducted is the transformation of the coordinate systems and comparison of the reference values to be able to perform a comparative transformation of the two results. This provides an additional way to proceed with the evaluation of the obtained data.

Finally, the obtained results should be fed back into DNS to see whether similar results to the initial DNS data can be derived.

Bibliography

[1] Peter Arbenz. *Lecture Notes on Solving Large Scale Eigenvalue Problems*. ETH, Spring 2012.

[2] Masahito Asai, Masayuki Minagawa, and Michio Nishioka. The instability and breakdown of a near-wall low-speed streak. *J. Fluid Mech.*, 455:289–314, 2002.

[3] Frederick W. Boltz, George C. Kenyon, and Clyde Q. Allen. Effects of sweep angle on the boundary-layer stability, characteristics of an untapered wing at low speeds. Technical Report D-338, NASA, October 1960.

[4] Luca Brandt. Numerical studies of the instability and breakdown of a boundary-layer low-speed streak. *European Journal of Mechanics B/Fluids*, 26:64–82, 2007.

[5] Luca Brandt and Dan S. Henningson. Transition of streamwise streaks in zero-pressure-gradient boundary layers. *J. Fluid Mech.*, 472:229–262, 2002.

[6] W. O. Criminale, T. L. Jackson, and R. D. Joslin. *Theory and Computation in Hydrodynamic Stability*. Cambridge University Press, 2003.

[7] Pascal Diggelmann. Investigation of the linear global instability of the attachment-line boundary layer, 2013.

[8] Brian F. Farrell and Petros J. Ioannou. Dynamics of streamwise rolls and streaks in turbulent wall-bounded shear flows. *J. Fluid Mech.*, 708:149–196, August 2012.

[9] M. Gaster. On the flow along swept leading edges. *The Aeronautical Quarterly*, 18:165–184, May 1967.

[10] Henry Görtler. *Dreidimensionale Instabilität der ebenen Staupunkt-Strömung gegenüber wirbelartigen Strukturen*. Fünfzig Jahre Grenzschichtforschung, 304–314. Vieweg und Sohn, 1955.

[11] W. E. Gray. The nature of the boundary layer flow at the nose of a swept wing. Technical Report Aero 256, Royal Aircraft Establishment, Farnborough, June 1952.

[12] Alan Guégan, Peter J. Schmid, and Patrick Huerre. Spatial optimal disturbances in swept attachment-line boundary layers. *J. Fluid Mech.*, 603:179–188, 2008.

[13] P. Hall, M. R. Malik, and D. I. A. Poll. On the stability of an infinite swept attachment line boundary layer. *Proc. R. Soc. Lond. A*, 395:229–245, 1984.

[14] P. Hall and Sharon O. Seddougui. Wave interactions in a three-dimensional attachment-line boundary layer. *J. Fluid Mech.*, 217:367–390, 1990.

[15] Günther Hämmerlin. *Zur Instabilitätstheorie der ebenen Staupunktströmung.* Fünfzig Jahre Grenzschichtforschung, 315–327. Vieweg und Sohn, 1955.

[16] K. Hiemenz. *Die Grenzschicht an einem in den gleichförmigen Flüssigkeitsstrom eingetauchten geraden Kreiszylinder.* PhD thesis, Göttingen, 1911.

[17] Jérôme Hœpffner, Luca Brandt, and Dan S. Henningson. Transient growth on boundary layer streaks. *J. Fluid Mech.*, 537:91–100, 2005.

[18] Julian Hügl. Visualisierung der transition einer dreidimensionalen plattengrenzschicht. Master's thesis, ETH Zürich, Seminararbeit, IFD, 2013.

[19] P. Jenny. *Lecture on Turbulent Flows.* ETH, 2012.

[20] Jinhee Jeong and Fazle Hussain. On the identification of a vortex. *J. Fluid Mech.*, 285:69–94, 1995.

[21] Michael O. John, Dominik Obrist, and Leonhard Kleiser. A class of exact navier-stokes similarity solutions for flat plate boundary layers with one homogeneous direction. *PAMM*, 2012.

[22] Michael O. John, Dominik Obrist, and Leonhard Kleiser. Stabilization of subcritical bypass transition in the leading-edge boundary layer by suction. *J. of Turb.*, to appear.

[23] Leonhard Kleiser and Dominik Obrist. *Lecture Notes on Hydrodynamic Stability and Transition.* ETH, 2013.

[24] Y. Kohama. Some expectation on the mechanism of cross-flow instability in a swept wing flow. *Acta Mechanica*, 66:21–38, 1987.

[25] Jr. Laurence K. Loftin. Quest for performance: The evolution of modern aircraft, part ii: The jet age, http://www.hq.nasa.gov/pao/history/sp-468/ch13-3.htm.

[26] Ray-Sing Lin and Mujeeb R. Malik. On the stability of attachment-line boundary layers. part 1. the incompressible swept hiemenz flow. *J. Fluid Mech.*, 311:239–255, 1996.

[27] M. R. Malik, F. Li, and C.-L. Chang. Crossflow disturbances in three-dimensional boundary layers: nonlinear development, wave interaction and secondary instability. *J. Fluid Mech.*, 268:1–36, 1994.

[28] Dominik Obrist. *On the stability of the swept leading-edge boundary layer.* PhD thesis, University of Washington, 2000.

[29] Dominik Obrist, Rolf Henniger, and Leonhard Kleiser. Subcritical spatial transition of swept hiemenz flow. *International Journal of Heat and Fluid Flow*, 35:61–67, 2012.

[30] Dominik Obrist and Peter J. Schmid. On the linear stability of swept attachment-line boundary layer flow. part 1. spectrum and asymptotic behaviour. *J. Fluid Mech.*, 493:1–29, 2003.

[31] José Miguel Pérez, Daniel Rodríguez, and Vassilis Theofilis. Linear global instability of non-orthogonal incompressible swept attachment-line boundary-layer flow. *J. Fluid Mech.*, 710:131–153, 2012.

[32] W. Pfenninger. Laminar flow control, laminarization. Technical Report 654, AGARD, 1977.

[33] D. I. A. Poll. Some aspects of the flow near a swept attachment line with particular reference to boundary layer transition. Technical Report 7805, Cranfield College of Aeronautics, August 1978.

[34] J. H. Preston. The boundary-layer flow over a permeable surface through which suction is applied. Reports and Memoranda 2244, Aeronautical Research Council, February 1946.

[35] Cécilia Robitaillié-Montané. *Une approche non locale pour l'étude des instabilités linéaires. Application à l'écoulement de couche limite compressible le long d'une ligne de partage.* PhD thesis, L'école Nationale Supérieure de L'aéronautique et de L'espace, 2005.

[36] Hermann Schlichting and Klaus Gersten. *Grenzschicht-Theorie.* Springer, 7 edition, 1951.

[37] Philippe R. Spalart. Direct numerical study of leading-edge contamination. *AGARD-CP*, (438), 1988.

[38] Fabian Waleffe. On a self-sustaining process in shear flows. *Physics of Fluids*, 9(4):883–900, 1997.

[39] Torsten Wintergerste. *Numerische Untersuchung der Spätstadien der Transition in einer dreidimensionalen Grenzschicht.* PhD thesis, ETH Zürich, 2002.

A. λ_2 Vortex Identification

This section is to shortly summarize the method employed in Section 5.4 to identify a vortex. Jeong and Hussain [20] have proposed a criterion for vortex identification which has become a sort of standard procedure. They start out by taking the divergence ("gradient") of the Navier-Stokes equations (2.2a) and deriving an expression for the acceleration gradient

$$a_{i,j} = -\frac{1}{\rho}p_{,ij} + \nu u_{i,jkk}. \tag{A.1}$$

Then the left-hand-side of (A.1) can be decomposed into a symmetric and anti-symmetric part,

$$a_{i,j} = \underbrace{\left[\frac{\mathrm{D}S_{ij}}{\mathrm{D}t} + \Omega_{ik}\Omega_{kj} + S_{ik}S_{kj}\right]}_{\text{symmetric}} + \underbrace{\left[\frac{\mathrm{D}\Omega_{ij}}{\mathrm{D}t} + \Omega_{ik}S_{kj} + S_{ik}\Omega_{kj}\right]}_{\text{antisymmetric}}, \tag{A.2}$$

where the antisymmetric part is the vorticity equation and the symmetric part:

$$\frac{\mathrm{D}S_{ij}}{\mathrm{D}t} - \nu S_{ij,kk} + \Omega_{ik}\Omega_{kj} + S_{ik}S_{kj} = -\frac{1}{\rho}p_{,ij}. \tag{A.3}$$

S and Ω represent the symmetric and antisymmetric components of the gradient ∇u, respectively:

$$S_{ij} = \frac{1}{2}(u_{i,j} + u_{j,i}) \tag{A.4}$$

$$\Omega_{ij} = \frac{1}{2}(u_{i,j} - u_{j,i}). \tag{A.5}$$

In order for the right-hand-side of Equation (A.3) to have a minimum it needs to have two negative eigenvalues. They neglect irrotational strain and viscous effects by dropping the first two terms on the left of Equation (A.3). Thus they find the eigenvalues of $S^2+\Omega^2$. The negative real eigenvalue λ_2 of smaller absolute value then defines the vortex core.

Within this report, the λ_2 eigenvalue isosurfaces were computed by superimposing eigenmodes onto the base flow. The eigenvalues were normalized with

$$\phi = \max||(|\hat{u}|, |\hat{v}|, |\hat{w}|)^T|| \tag{A.6}$$

and added to the base flow with a fraction A:

$$u = U + \frac{A}{\phi}u' \tag{A.7}$$

$$v = V + \frac{A}{\phi}v' \tag{A.8}$$

$$w = W + \frac{A}{\phi}w'. \tag{A.9}$$

B. Base Flows

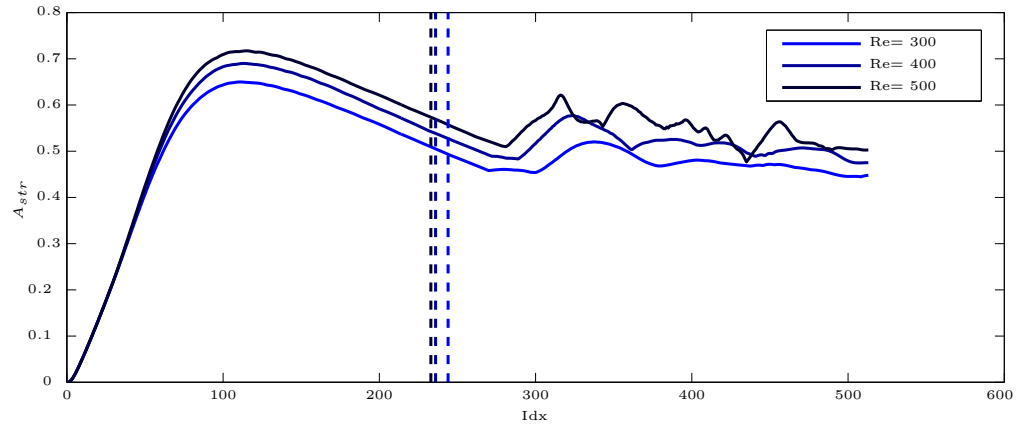

(a)

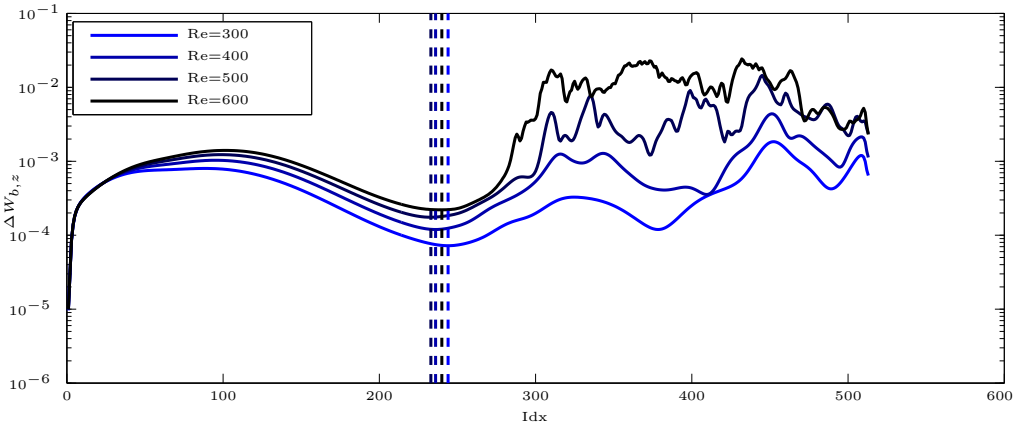

(b)

Figure B.1.: Top: Streak amplitude of the base flows without secondary amplitude A_2. Bottom: $\frac{\partial}{\partial z}W_b$ of the same base flows. In both figures the extraction locations are marked.

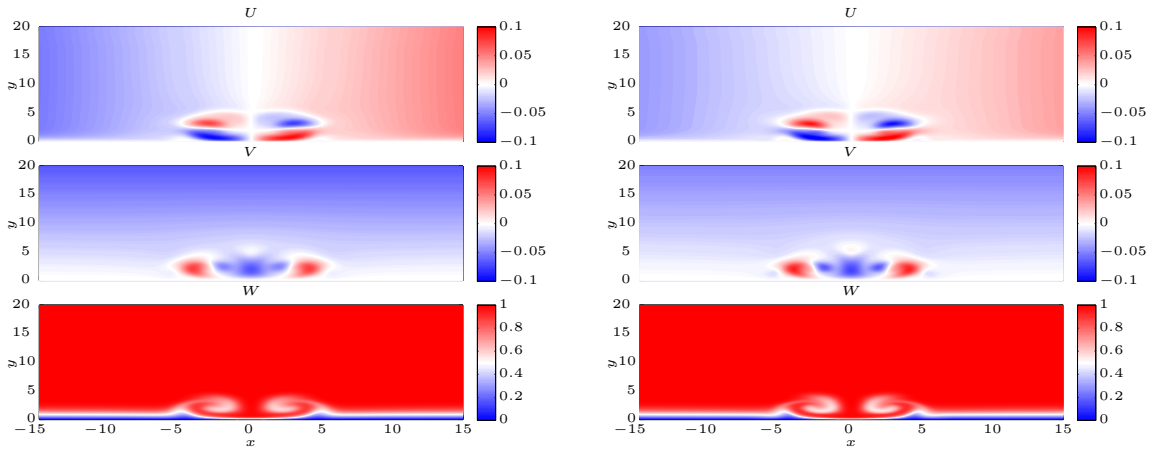

(a) Re= 300

(b) Re= 400

(c) Re= 500

(d) Re= 600

Figure B.2.: Base flow profiles of the different base flows without secondary amplitude A_2 at the extraction locations.

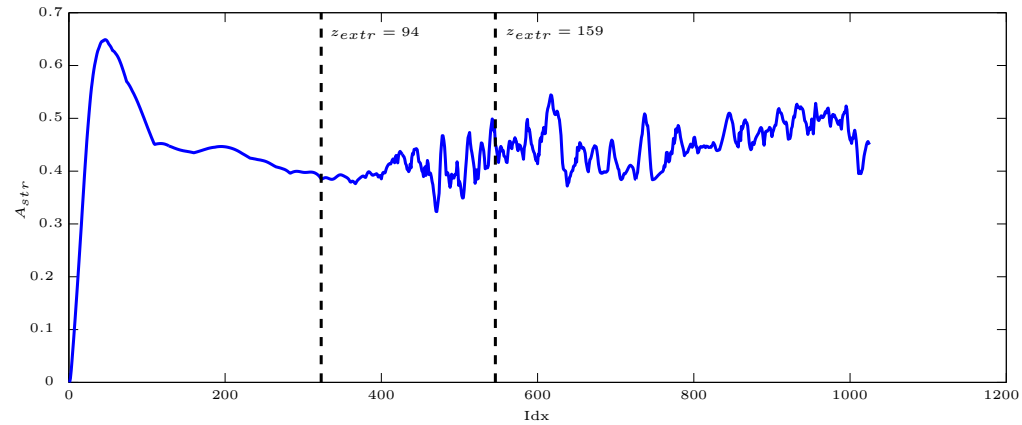

(a)

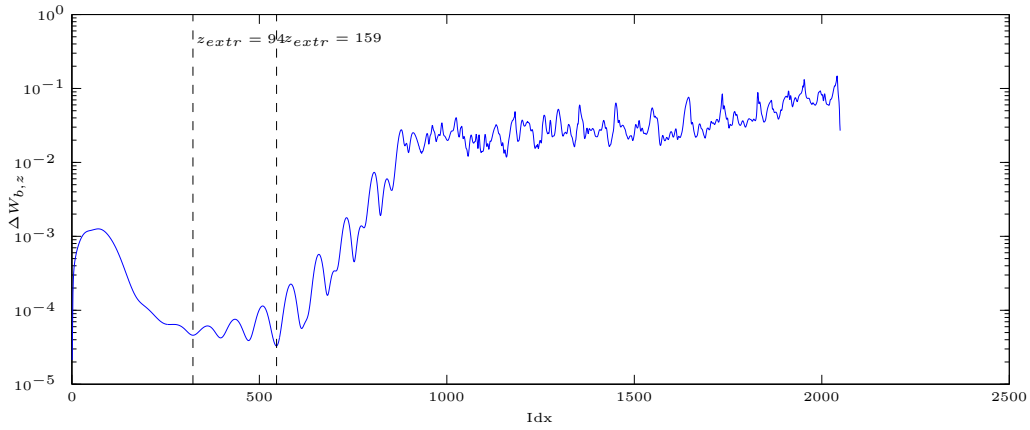

(b)

Figure B.3.: Top: Streak amplitude of the base flow with secondary amplitude A_2. Bottom: $\frac{\partial}{\partial z} W_b$ of the same base flow. In both figures the extraction locations are marked.

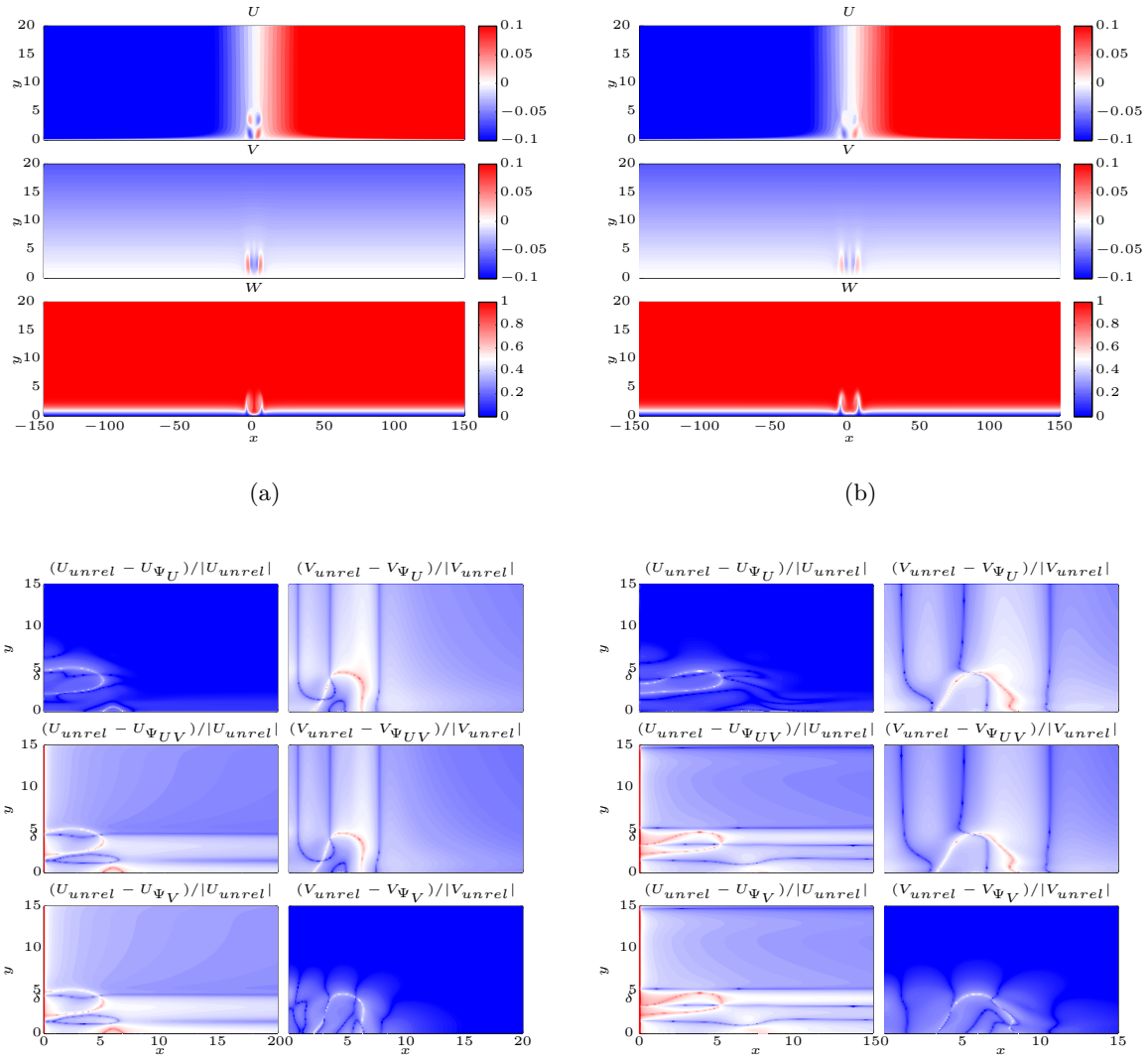

Figure B.4.: Base flow profiles of the base flow with secondary amplitude A_2 at the extraction locations $z_{extr} = 94$ (left) and $z_{extr} = 159$ (right). Top: Unrelaxed base flow profiles. Bottom: Errors resulting from relaxation.

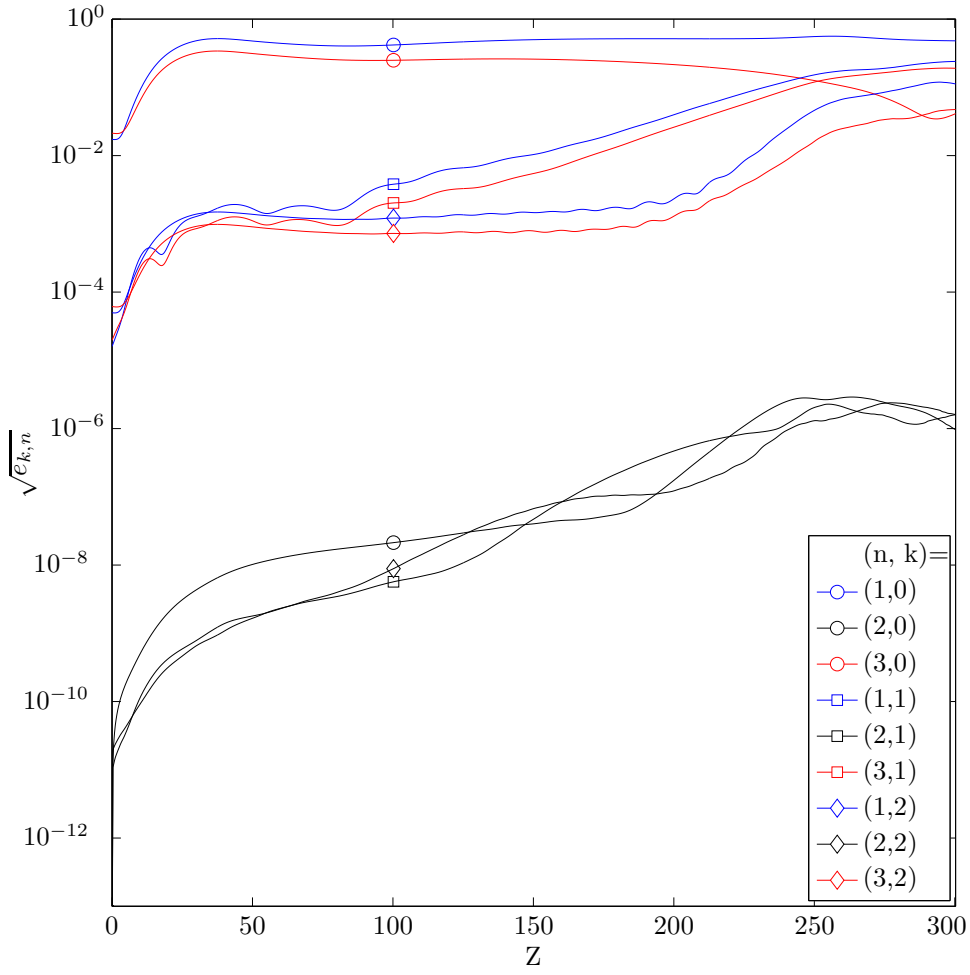

Figure B.5.: Fourier-Hermite Spectral energy density decomposition of the base flow with secondary amplitude A_2 with chordwise Hermite-polynomial order n and temporal harmonic k. Their is visible evidence of secondary ($k = 1$) modal growth of symmetric modes (n odd) between $z = 100$ and $z = 250$.

C. Eigenmodes

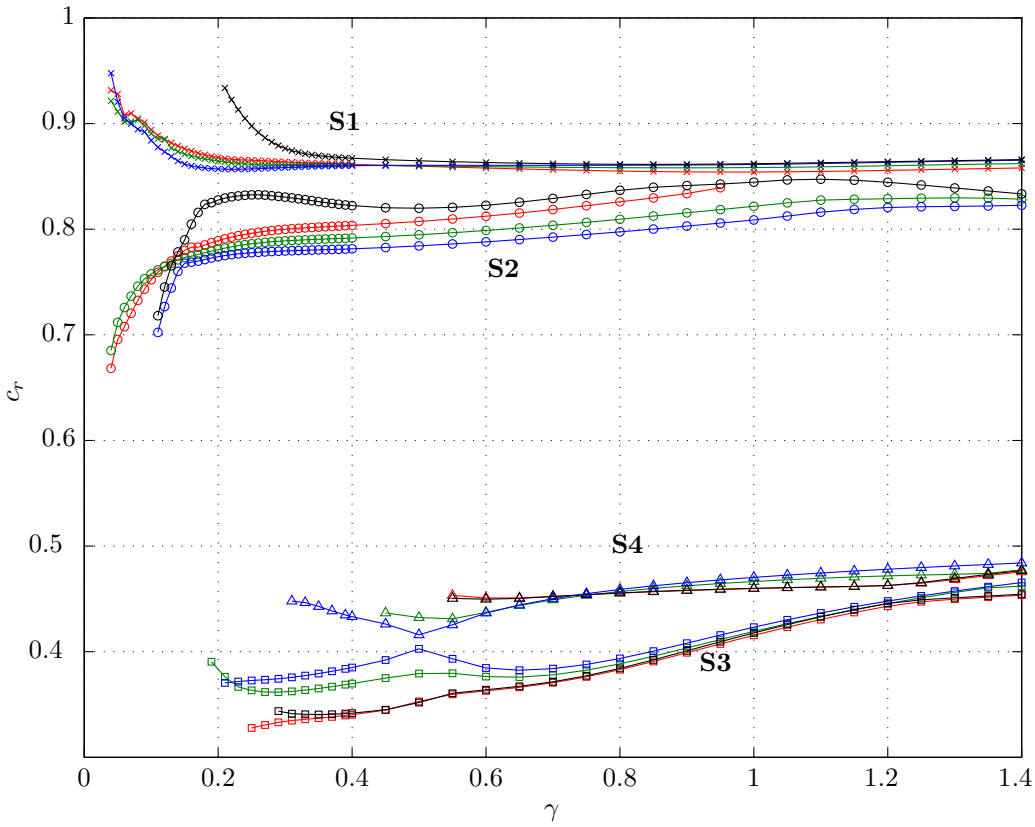

Figure C.1.: Eigenmodes' phase speeds vs. γ at $z_{extr} = 94$ for parameters $L_x = 20$, $L_y = 15$, $N_x = 147$, $N_y = 120$ (**S1**, **S2**), $N_x = 154$, $N_y = 130$ (**S3**, **S4**) and $x_{\text{half}} = L_x/3$, $y_{\text{half}} = L_y/3$ and BC $\hat{u}(x = 0, y) = 0$. The colors represent: —Ψ_U, —Ψ_{U+V}, —Ψ_V, —unrelaxed.

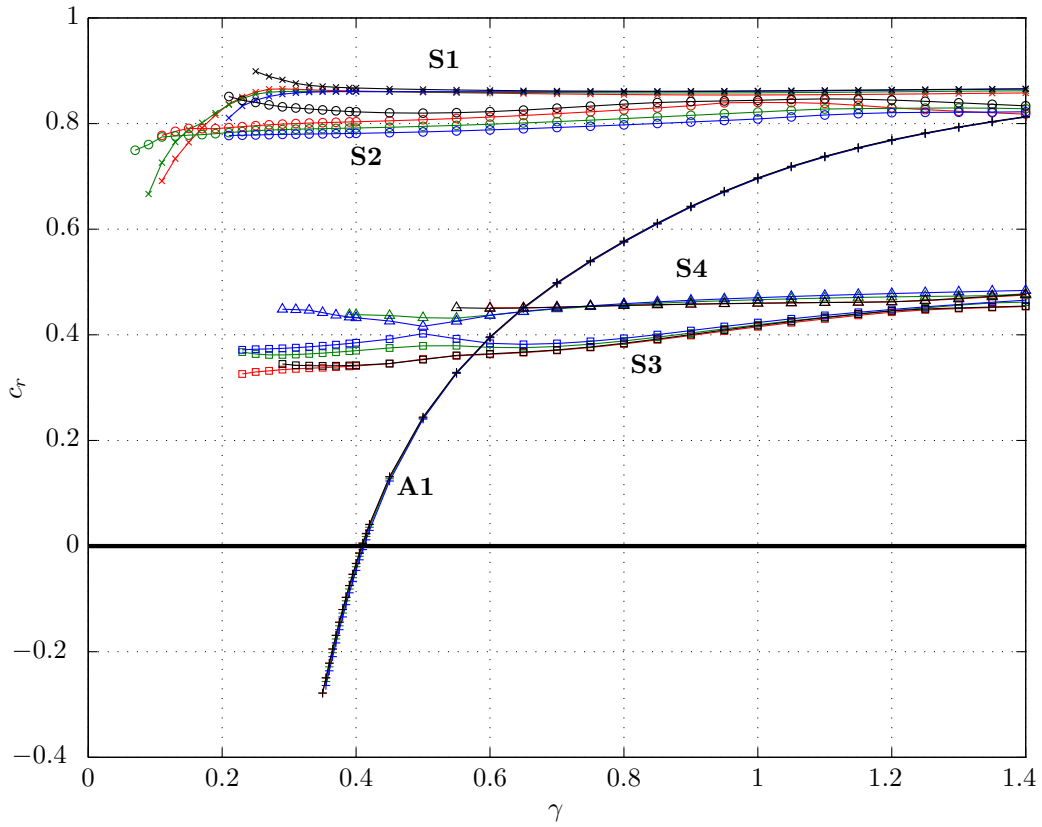

Figure C.2.: Eigenmodes' phase speeds vs. γ at $z_{extr} = 94$ for parameters $L_x = 20$, $L_y = 15$, $N_x = 147$, $N_y = 120$ (**S1**, **S2**), $N_x = 154$, $N_y = 130$ (**S3**, **S4**) and $x_{\text{half}} = L_x/3$, $y_{\text{half}} = L_y/3$ and BC $\partial^2/\partial x^2 \hat{u}(x = 0, y) = 0$. The colors represent: —Ψ_U, —Ψ_{U+V}, —Ψ_V, —unrelaxed.

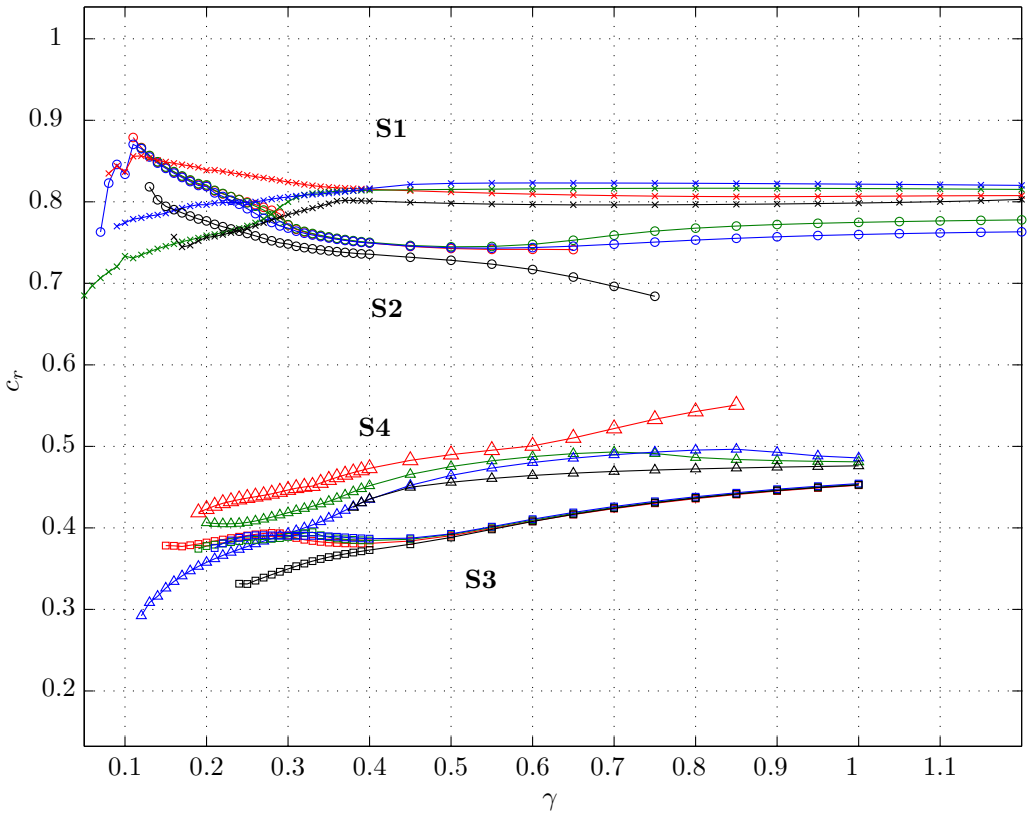

Figure C.3.: Eigenmodes' phase speeds vs. γ at $z_{extr} = 159$ for parameters $L_x = 20$, $L_y = 15$, $N_x = 147$, $N_y = 120$ (**S1**, **S2**), $N_x = 154$, $N_y = 130$ (**S3**, **S4**) and $x_{\text{half}} = L_x/3$, $y_{\text{half}} = L_y/3$ and BC $\hat{u}(x = 0, y) = 0$. The colors represent: —Ψ_U, —Ψ_{U+V}, —Ψ_V, —unrelaxed.

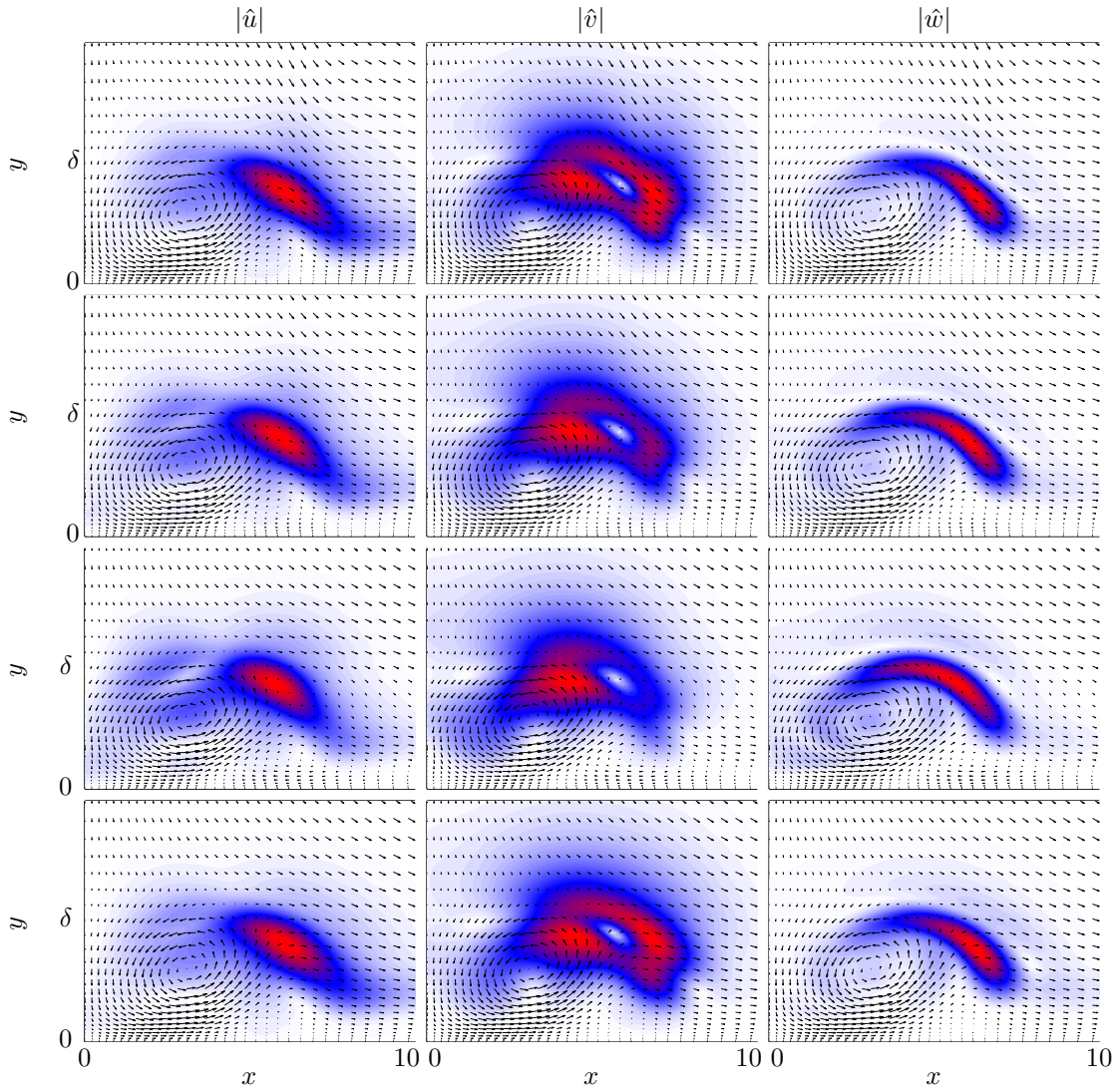

Figure C.4.: Shapes of eigenmode **S1** for various Ψ at $z_{extr} = 94$ for Re $= 300$, $\gamma = 0.6$, $L_x = 20$, $L_y = 15$, $Nx = 147$, $Ny = 120$, $x_{\text{half}} = L_x/3$, $y_{\text{half}} = L_y/3$ and BC $\partial^2/\partial x^2 \hat{u}(x = 0, y) = 0$. Top: Ψ_U, Second Row: Ψ_{U+V}, Third Row: Ψ_V, Bottom: unrelaxed. White equals 0 and red equals 1.

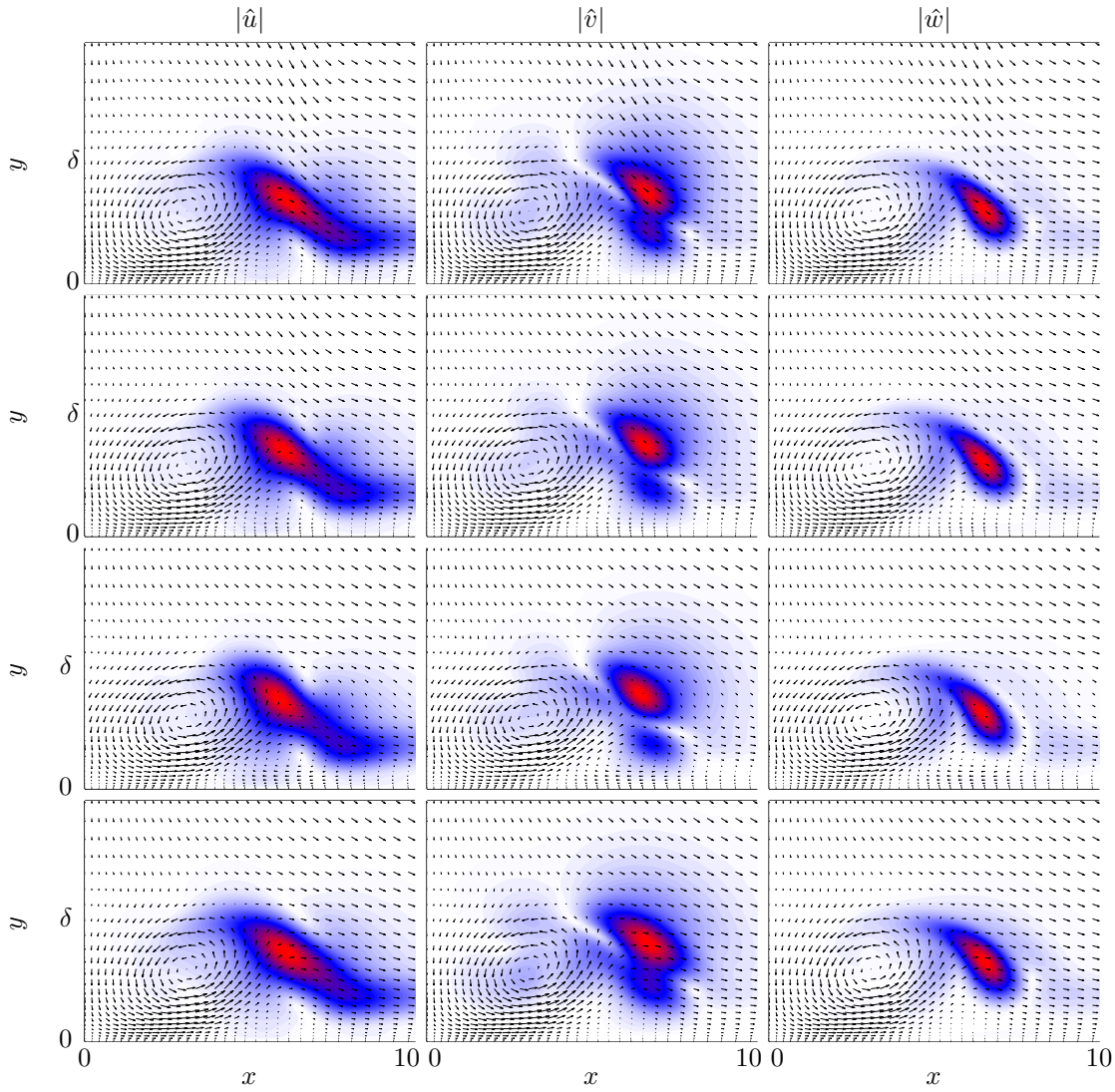

Figure C.5.: Shapes of eigenmode **S2** for various Ψ at $z_{extr} = 94$ for Re $= 300$, $\gamma = 0.6$, $L_x = 20$, $L_y = 15$, $Nx = 147$, $Ny = 120$, $x_{\text{half}} = L_x/3$, $y_{\text{half}} = L_y/3$ and BC $\partial^2/\partial x^2 \hat{u}(x = 0, y) = 0$. Top: Ψ_U, Second Row: Ψ_{U+V}, Third Row: Ψ_V, Bottom: unrelaxed. White equals 0 and red equals 1.

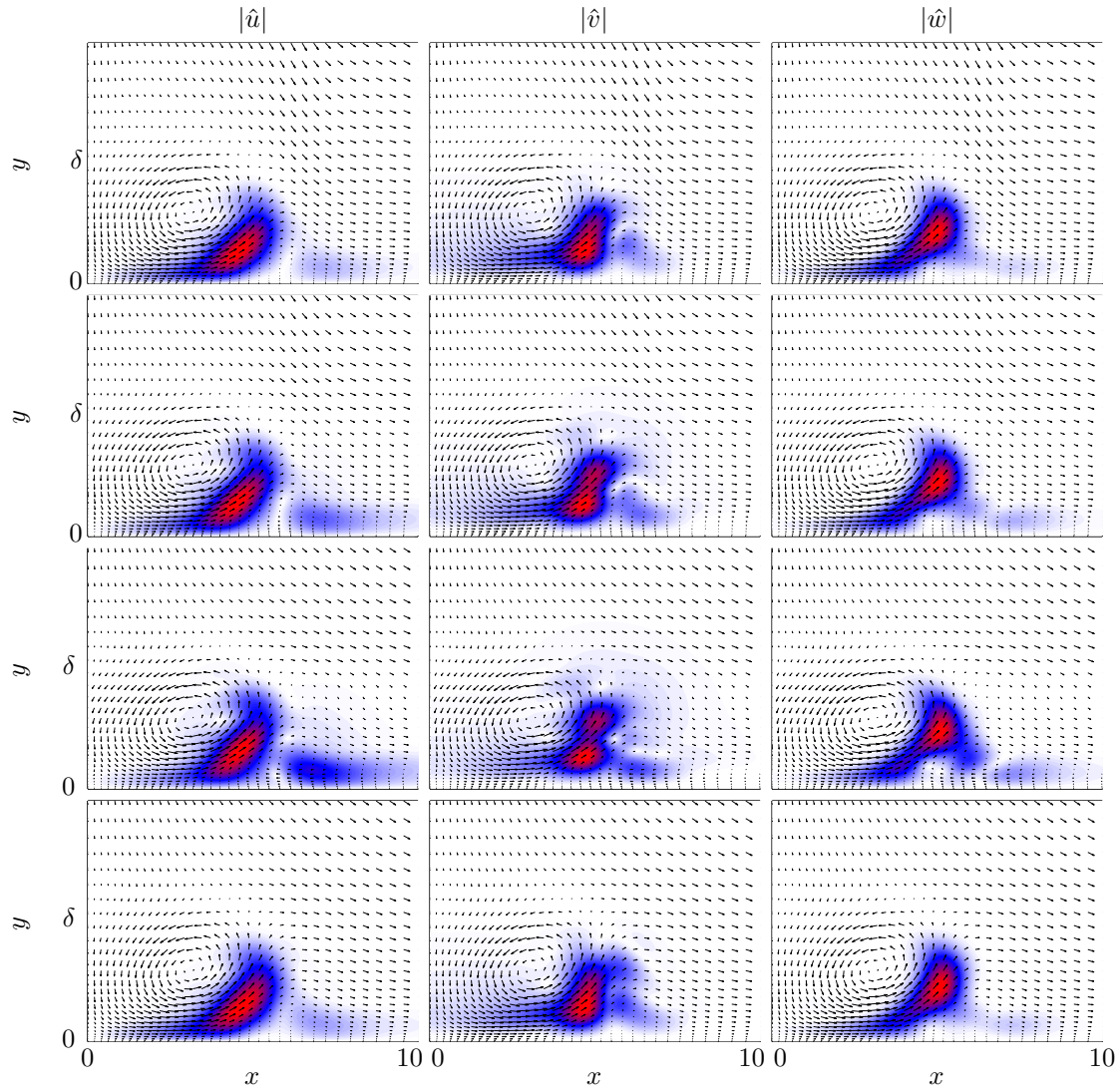

Figure C.6.: Shapes of eigenmode **S3** for various Ψ at $z_{extr} = 94$ for Re $= 300$, $\gamma = 0.6$, $L_x = 20$, $L_y = 15$, $Nx = 154$, $Ny = 130$, $x_{\text{half}} = L_x/3$, $y_{\text{half}} = L_y/3$ and BC $\partial^2/\partial x^2 \hat{u}(x = 0, y) = 0$. Top: Ψ_U, Second Row: Ψ_{U+V}, Third Row: Ψ_V, Bottom: unrelaxed. White equals 0 and red equals 1.

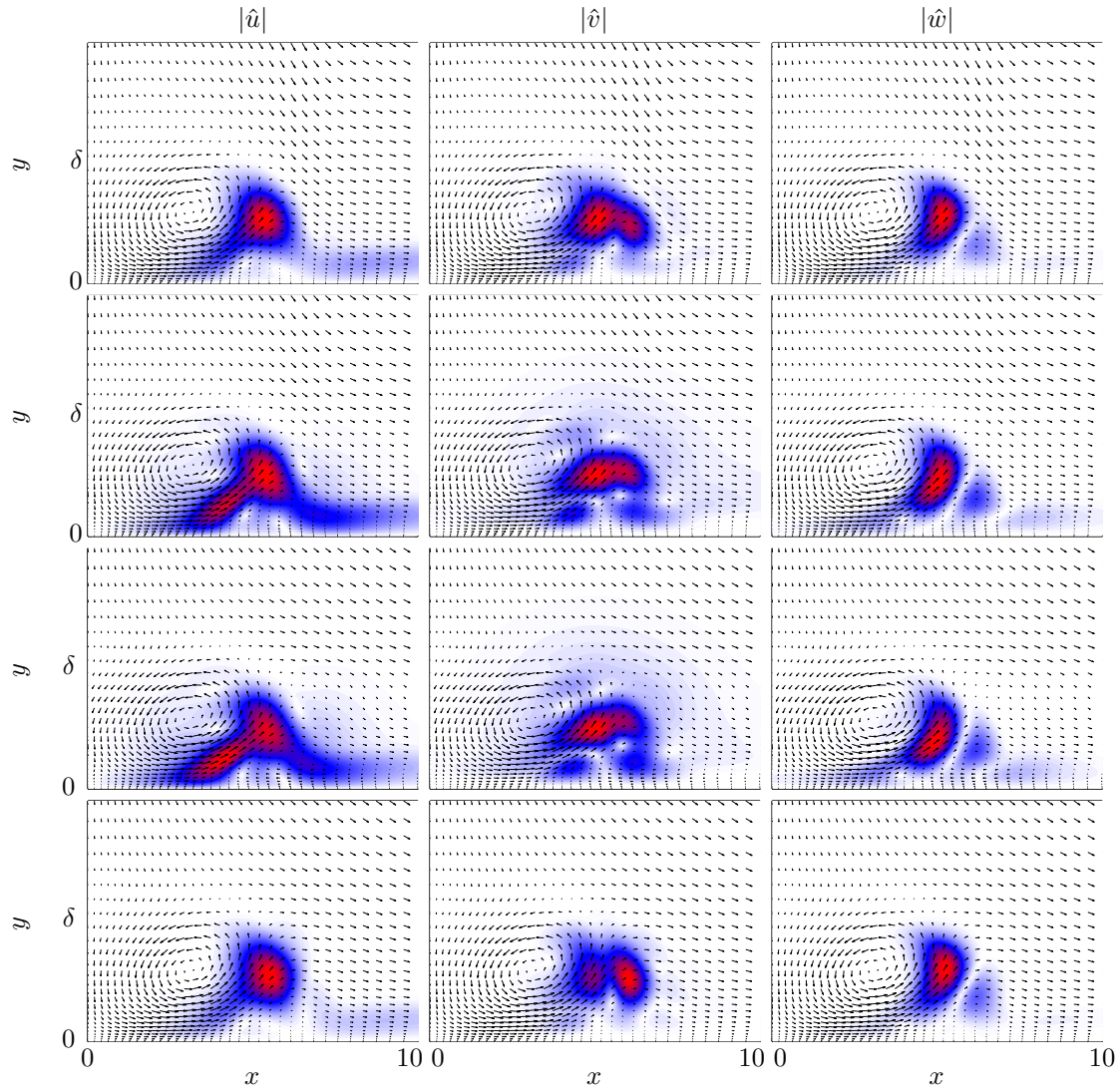

Figure C.7.: Shapes of eigenmode **S4** for various Ψ at $z_{extr} = 94$ for Re $= 300$, $\gamma = 0.6$, $L_x = 20$, $L_y = 15$, $Nx = 154$, $Ny = 130$, $x_{\text{half}} = L_x/3$, $y_{\text{half}} = L_y/3$ and BC $\partial^2/\partial x^2 \hat{u}(x = 0, y) = 0$. Top: Ψ_U, Second Row: Ψ_{U+V}, Third Row: Ψ_V, Bottom: unrelaxed. White equals 0 and red equals 1.

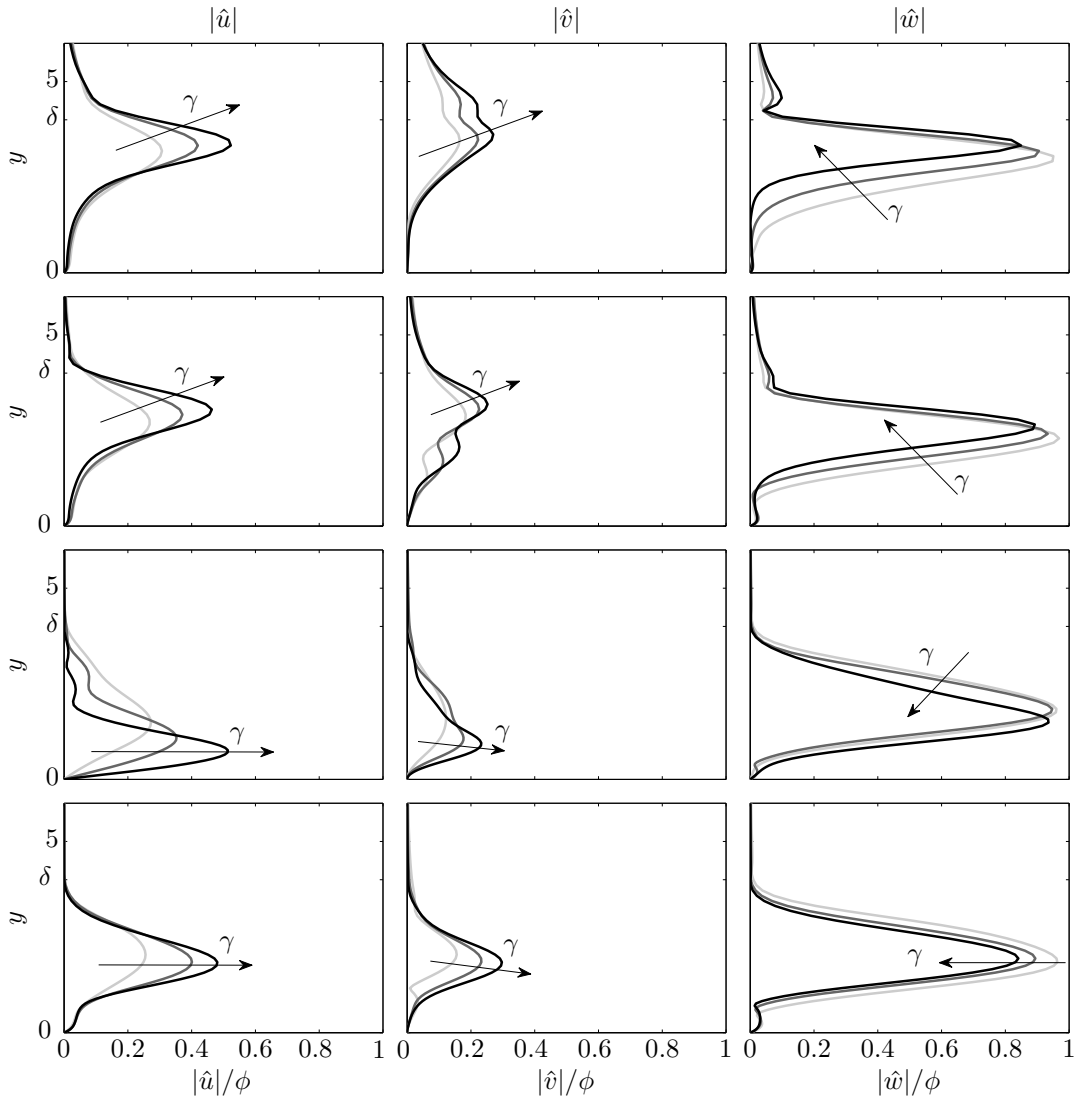

Figure C.8.: Symmetric eigenmodes' velocity profiles over y for varying γ and a relaxation with Ψ_{UV} ($\chi = 0.5$). The velocities are normalized with $\phi = \max||(\hat{u}, \hat{v}, \hat{w})||$ and plotted through their respective maxima. Parameters hereof are Re = 300 at $z_{extr} = 94$, $L_x = 20$, $L_y = 15$, $N_x = 147$, $N_y = 120$ (**S1**, **S2**), $N_x = 154$, $N_y = 130$ (**S3**, **S4**) and $x_{\text{half}} = L_x/3$, $y_{\text{half}} = L_y/3$ and BC $\hat{u}(x = 0, y) = 0$. Top: **S1**, second row: **S2**, third row: **S3**, bottom: **S4**.

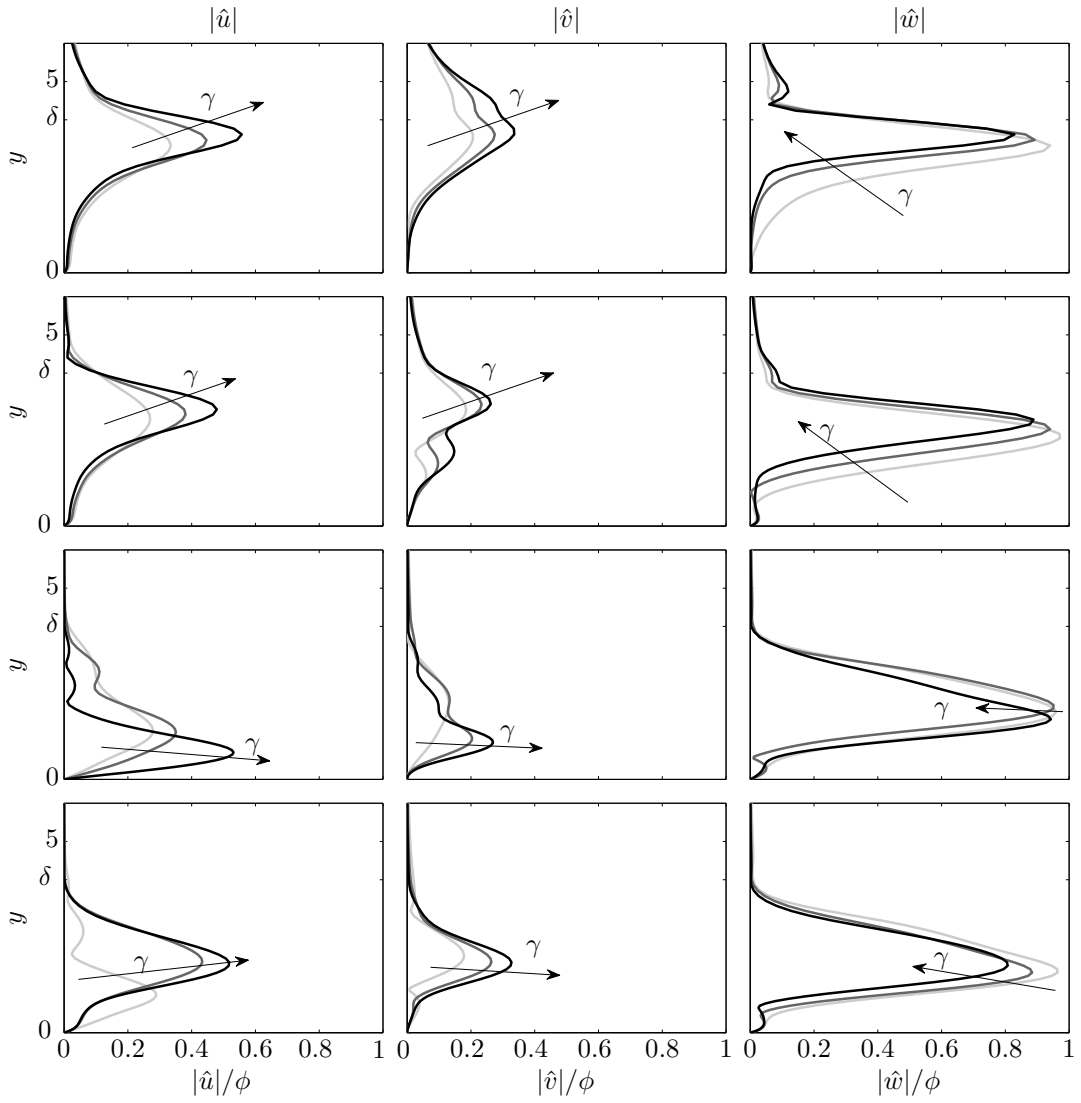

Figure C.9.: Symmetric eigenmodes' velocity profiles over y for varying γ and a relaxation with Ψ_V ($\chi = 0$). The velocities are normalized with $\phi = \max||(\hat{u}, \hat{v}, \hat{w})||$ and plotted through their respective maxima. Parameters hereof are Re $= 300$ at $z_{extr} = 94$, $L_x = 20$, $L_y = 15$, $N_x = 147$, $N_y = 120$ (**S1**, **S2**), $N_x = 154$, $N_y = 130$ (**S3**, **S4**) and $x_{\text{half}} = L_x/3$, $y_{\text{half}} = L_y/3$ and BC $\hat{u}(x = 0, y) = 0$. Top: **S1**, second row: **S2**, third row: **S3**, bottom: **S4**.

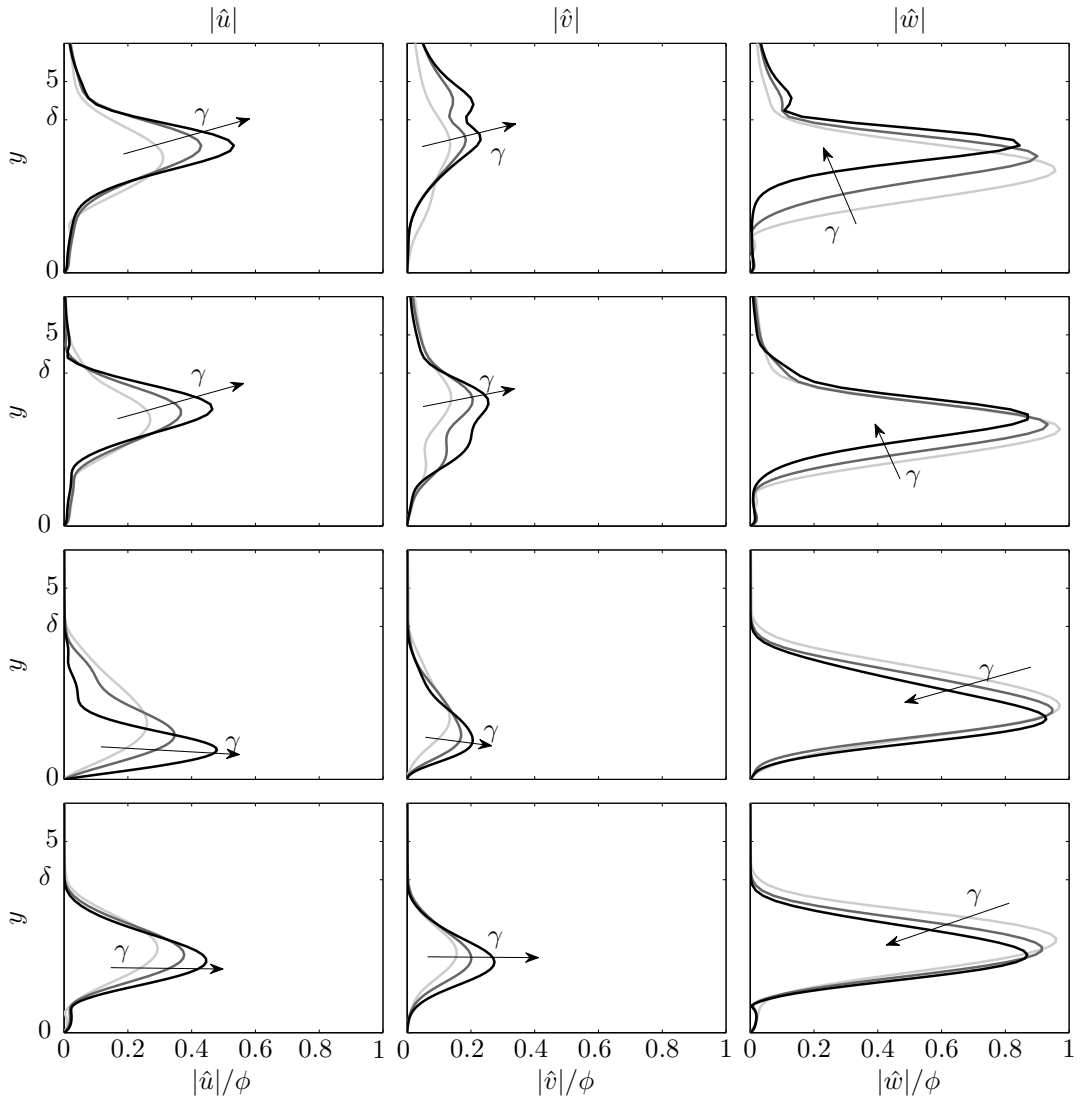

Figure C.10.: Symmetric eigenmodes' velocity profiles over y for varying γ and no relaxation. The velocities are normalized with $\phi = \max||(\hat{u}, \hat{v}, \hat{w})||$ and plotted through their respective maxima. Parameters hereof are $\mathrm{Re} = 300$ at $z_{extr} = 94$, $L_x = 20$, $L_y = 15$, $N_x = 147$, $N_y = 120$ (**S1**, **S2**), $N_x = 154$, $N_y = 130$ (**S3**, **S4**) and $x_{\mathrm{half}} = L_x/3$, $y_{\mathrm{half}} = L_y/3$ and BC $\hat{u}(x = 0, y) = 0$. Top: **S1**, second row: **S2**, third row: **S3**, bottom: **S4**.

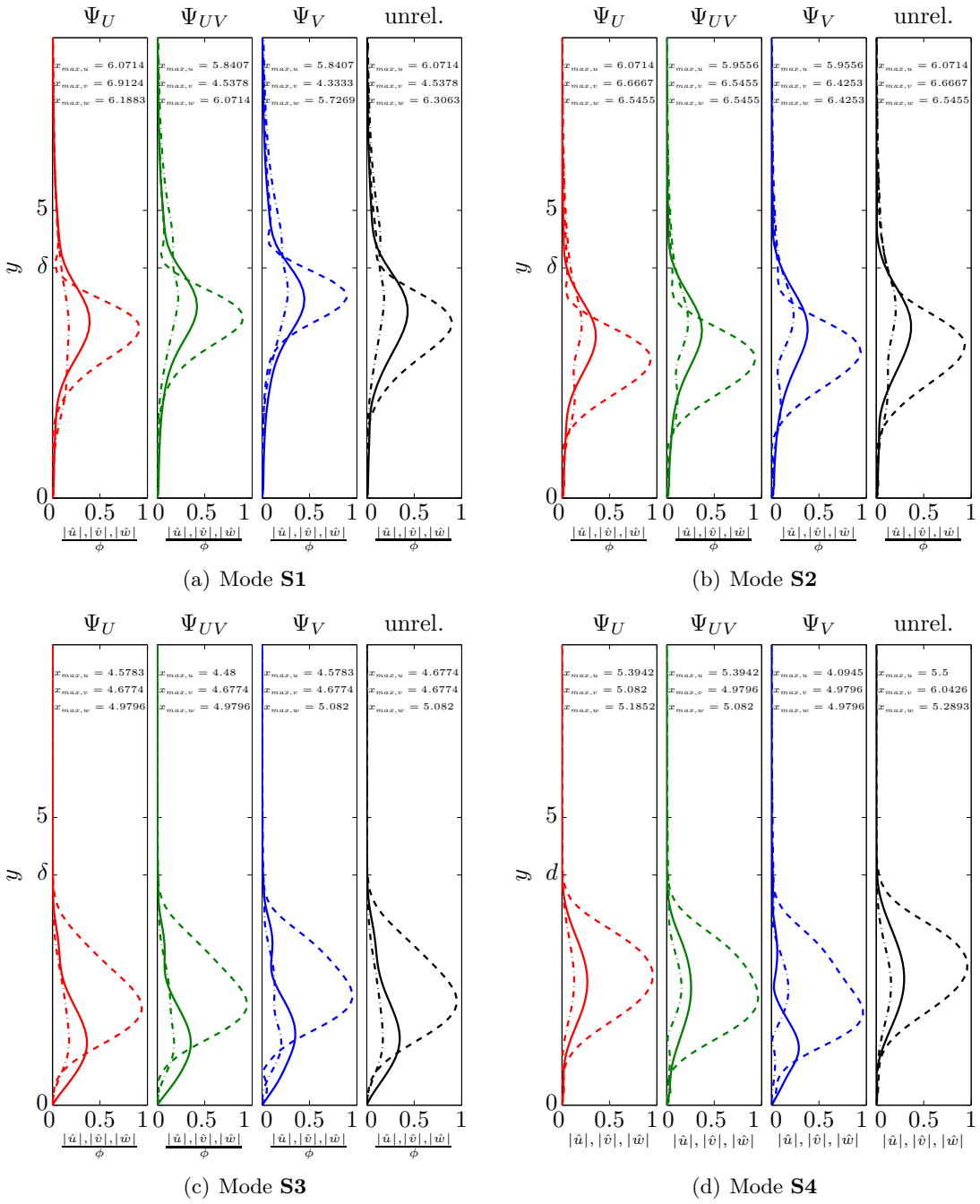

Figure C.11.: Symmetric eigenmodes' velocity profiles over y for different Ψ. The velocities are normalized with $\phi = \max||(\hat{u}, \hat{v}, \hat{w})||$ and plotted through their respective maxima. Parameters hereof are Re $= 300$, $\gamma = 0.6$ at $z_{extr} = 94$, $L_x = 20$, $L_y = 15$, $N_x = 147$, $N_y = 120$ (**S1**, **S2**), $N_x = 154$, $N_y = 130$ (**S3**, **S4**) and $x_{\text{half}} = L_x/3$, $y_{\text{half}} = L_y/3$ and BC $\partial^2/\partial x^2 \hat{u}(x = 0, y) = 0$.The colors represent: —$\Psi_U$, —$\Psi_{U+V}$, —$\Psi_V$, —unrelaxed. Solid line: $|\hat{u}|$, dashed-dotted line: $|\hat{v}|$, dashed line: $|\hat{w}|$.

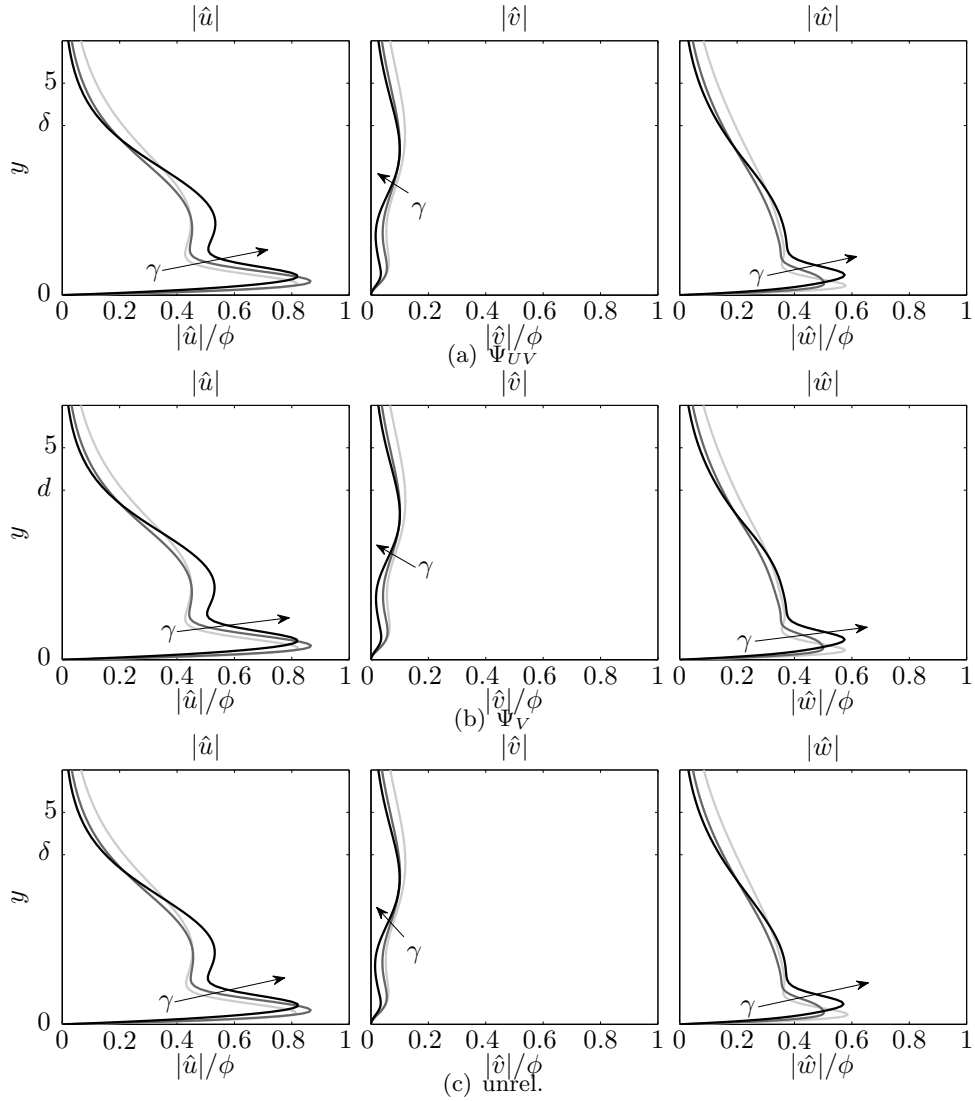

Figure C.12.: Antisymmetric eigenmode's velocity profiles over y for varying γ and different relaxations. The velocities are normalized with $\phi = \max||(\hat{u}, \hat{v}, \hat{w})||$ and plotted through their respective maxima. Parameters hereof are Re = 300 at $z_{extr} = 94$, $L_x = 20$, $L_y = 15$, $N_x = 147$, $N_y = 120$ and $x_{\text{half}} = L_x/3$, $y_{\text{half}} = L_y/3$ and BC $\partial^2/\partial x^2 \hat{u}(x = 0, y) = 0$.

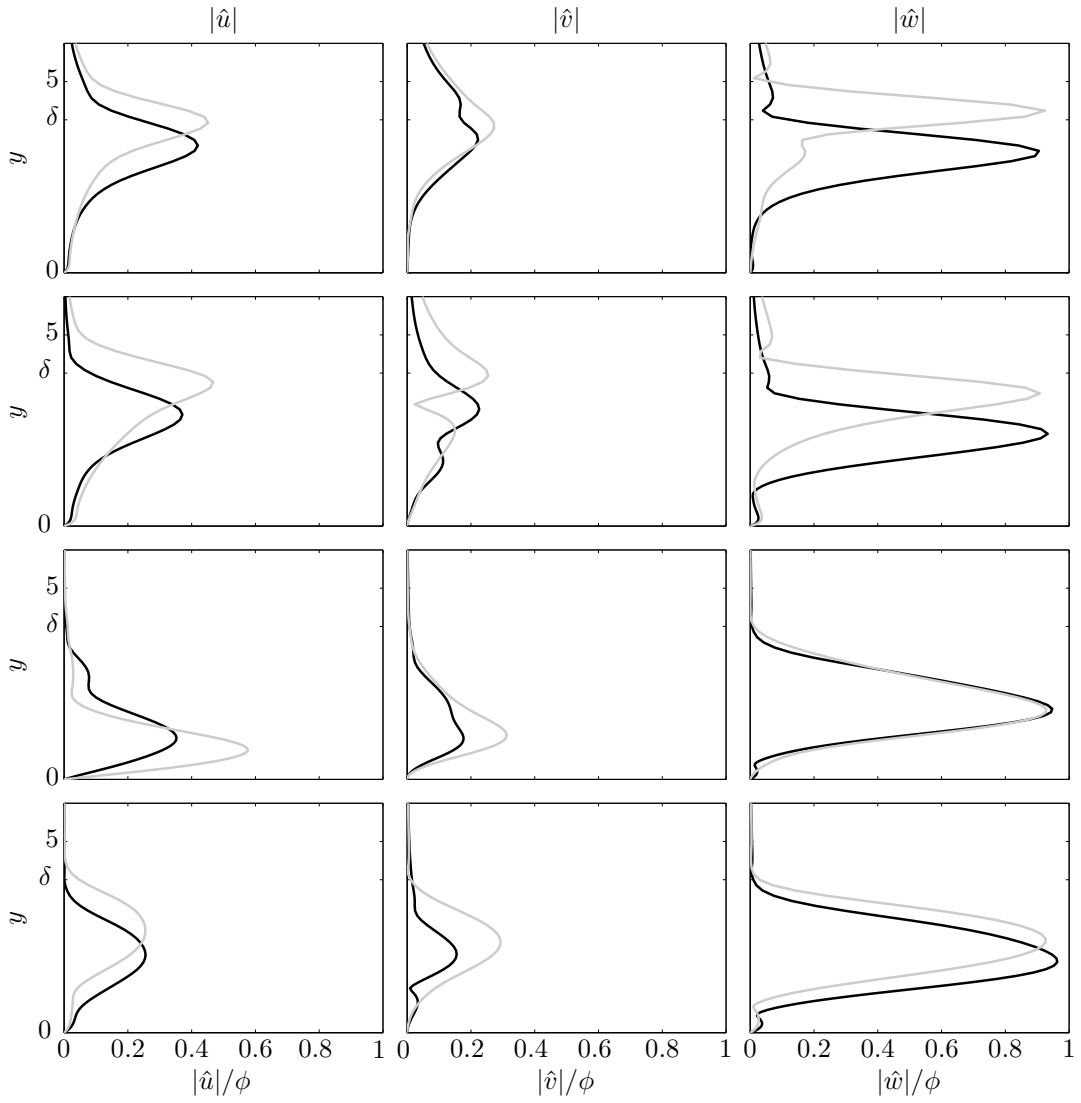

Figure C.13.: Symmetric eigenmodes' velocity profiles for different z_{extr}. The dark profile represents the location $z_{extr} = 94$, the light profile is further downstream at $z_{extr} = 159$. The velocities are normalized with $\phi = \max||(\hat{u}, \hat{v}, \hat{w})||$ and plotted through their respective maxima. Parameters hereof are Re $= 300$, Ψ_{UV}, $\gamma = 0.6$, $L_x = 20$, $L_y = 15$, $N_x = 147$, $N_y = 120$ (**S1**, **S2**), $N_x = 154$, $N_y = 130$ (**S3**, **S4**) and $x_{\text{half}} = L_x/3$, $y_{\text{half}} = L_y/3$ and BC $\hat{u}(x = 0, y) = 0$.

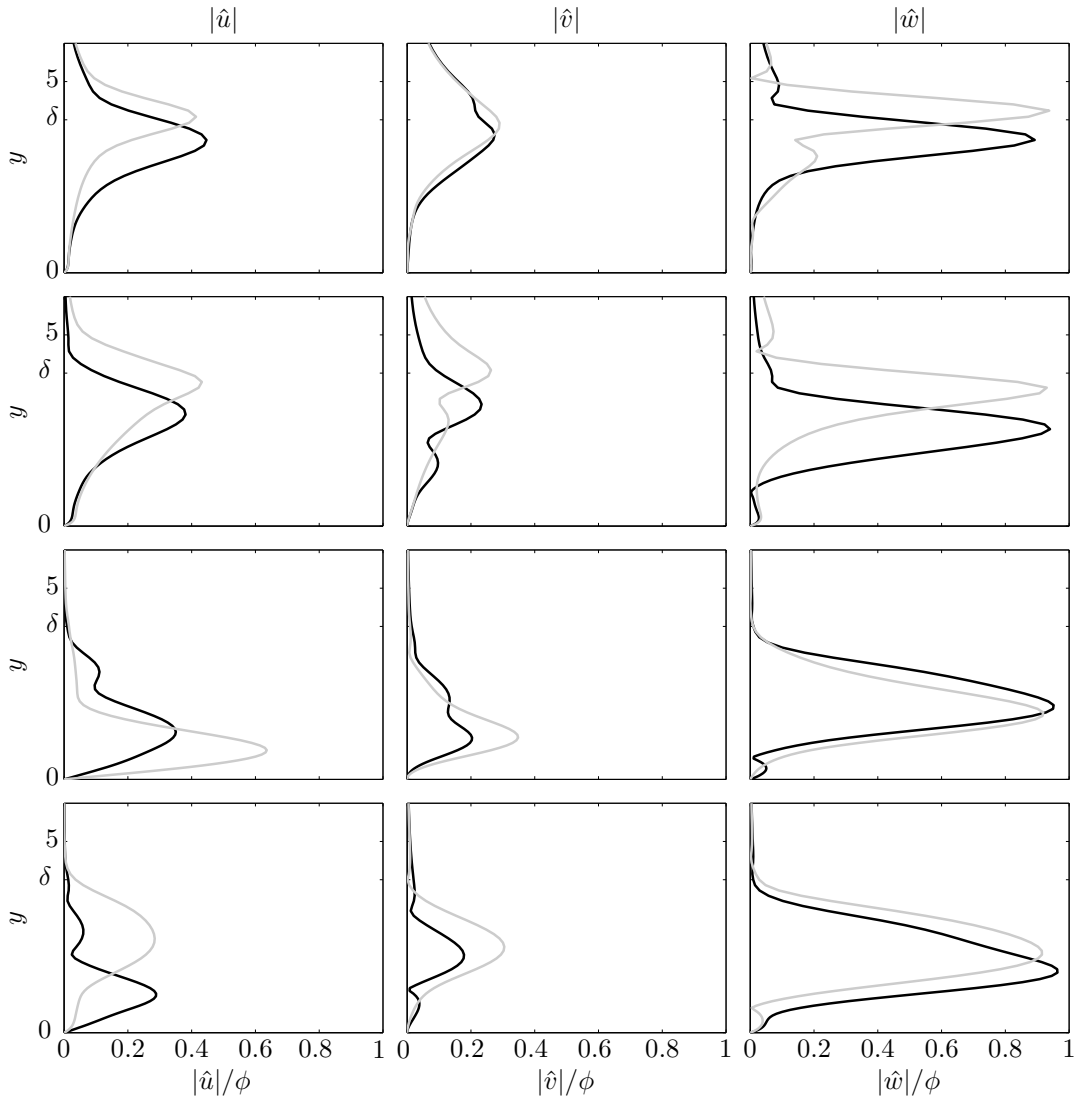

Figure C.14.: Symmetric eigenmodes' velocity profiles for different z_{extr}. The dark profile represents the location $z_{extr} = 94$, the light profile is further downstream at $z_{extr} = 159$. The velocities are normalized with $\phi = \max||(\hat{u}, \hat{v}, \hat{w})||$ and plotted through their respective maxima. Parameters hereof are Re $= 300$, Ψ_V, $\gamma = 0.6$, $L_x = 20$, $L_y = 15$, $N_x = 147$, $N_y = 120$ (**S1**, **S2**), $N_x = 154$, $N_y = 130$ (**S3**, **S4**) and $x_{\text{half}} = L_x/3$, $y_{\text{half}} = L_y/3$ and BC $\hat{u}(x = 0, y) = 0$.

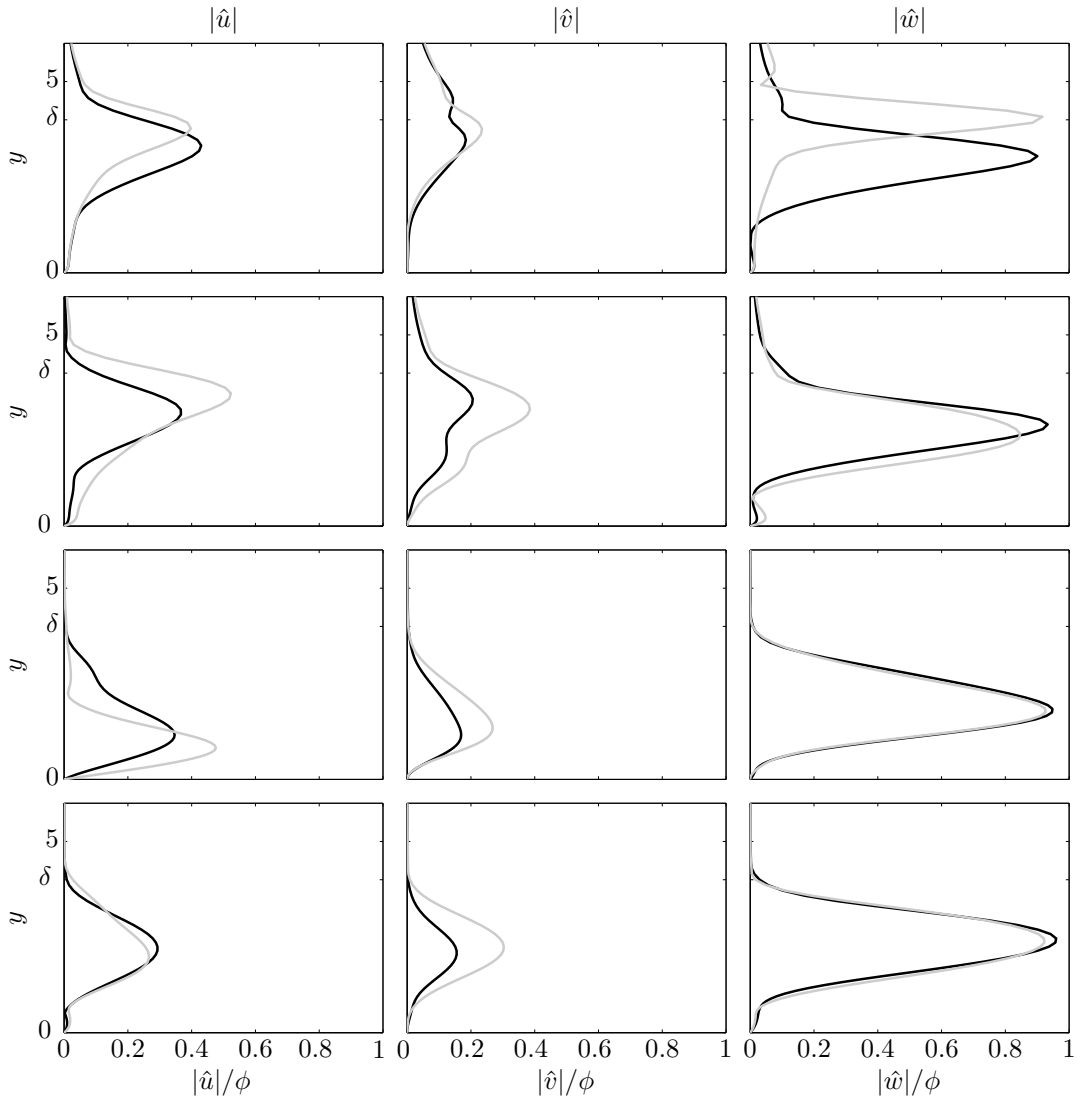

Figure C.15.: Symmetric eigenmodes' velocity profiles for different z_{extr}. The dark profile represents the location $z_{extr} = 94$, the light profile is further downstream at $z_{extr} = 159$. The velocities are normalized with $\phi = \max||(\hat{u}, \hat{v}, \hat{w})||$ and plotted through their respective maxima. Parameters hereof are Re = 300, unrelaxed, $\gamma = 0.6$, $L_x = 20$, $L_y = 15$, $N_x = 147$, $N_y = 120$ (**S1**, **S2**), $N_x = 154$, $N_y = 130$ (**S3**, **S4**) and $x_{\text{half}} = L_x/3$, $y_{\text{half}} = L_y/3$ and BC $\hat{u}(x = 0, y) = 0$.

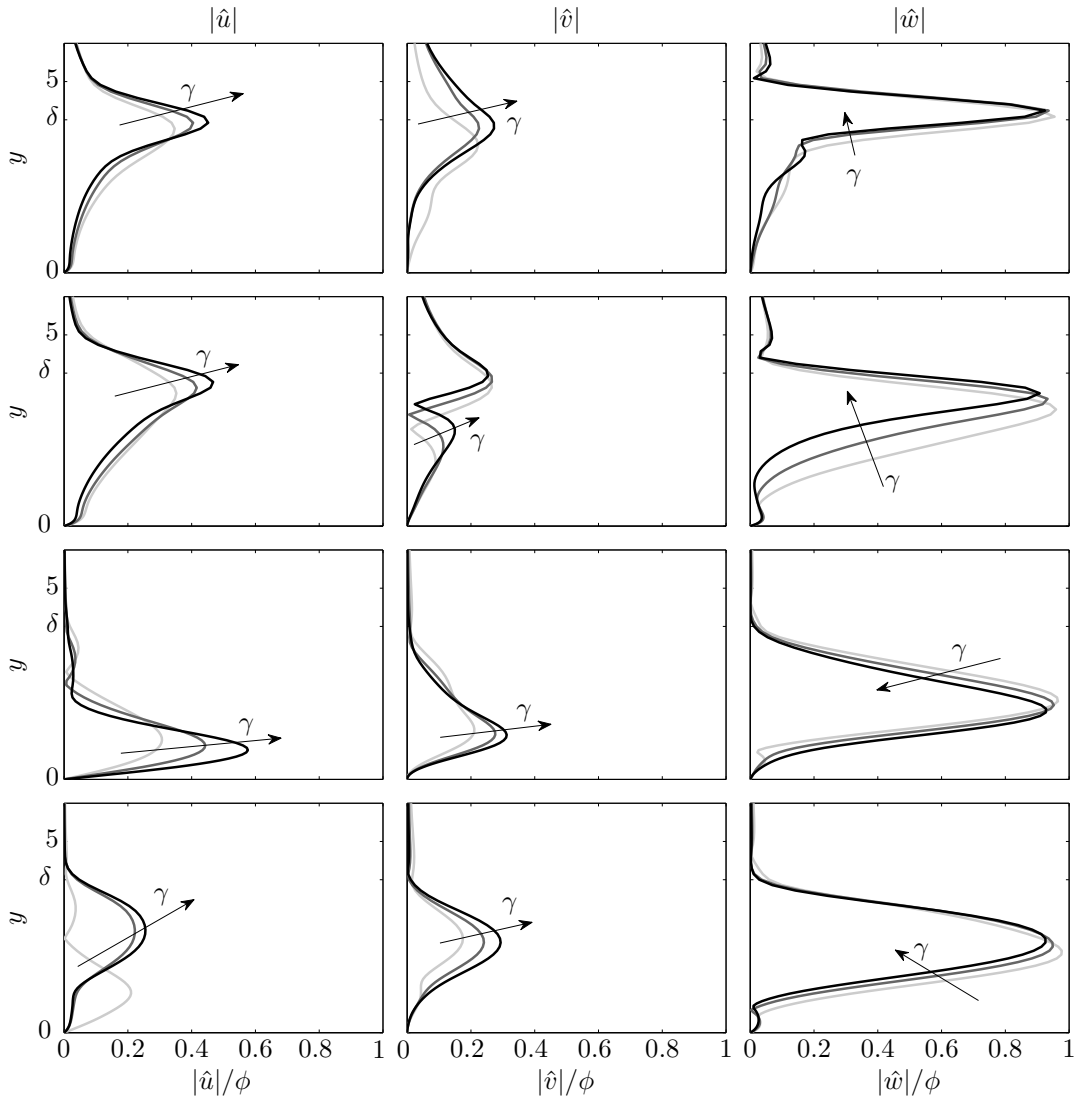

Figure C.16.: Symmetric eigenmodes' velocity profiles over y for varying γ and a relaxation with Ψ_{UV} ($\chi = 0.5$). The velocities are normalized with $\phi = \max||(\hat{u}, \hat{v}, \hat{w})||$ and plotted through their respective maxima. Parameters hereof are Re = 300 at $z_{extr} = 159$, $L_x = 20$, $L_y = 15$, $N_x = 147$, $N_y = 120$ (**S1**, **S2**), $N_x = 154$, $N_y = 130$ (**S3**, **S4**) and $x_{\text{half}} = L_x/3$, $y_{\text{half}} = L_y/3$ and BC $\hat{u}(x = 0, y) = 0$. Top: **S1**, second row: **S2**, third row: **S3**, bottom: **S4**.

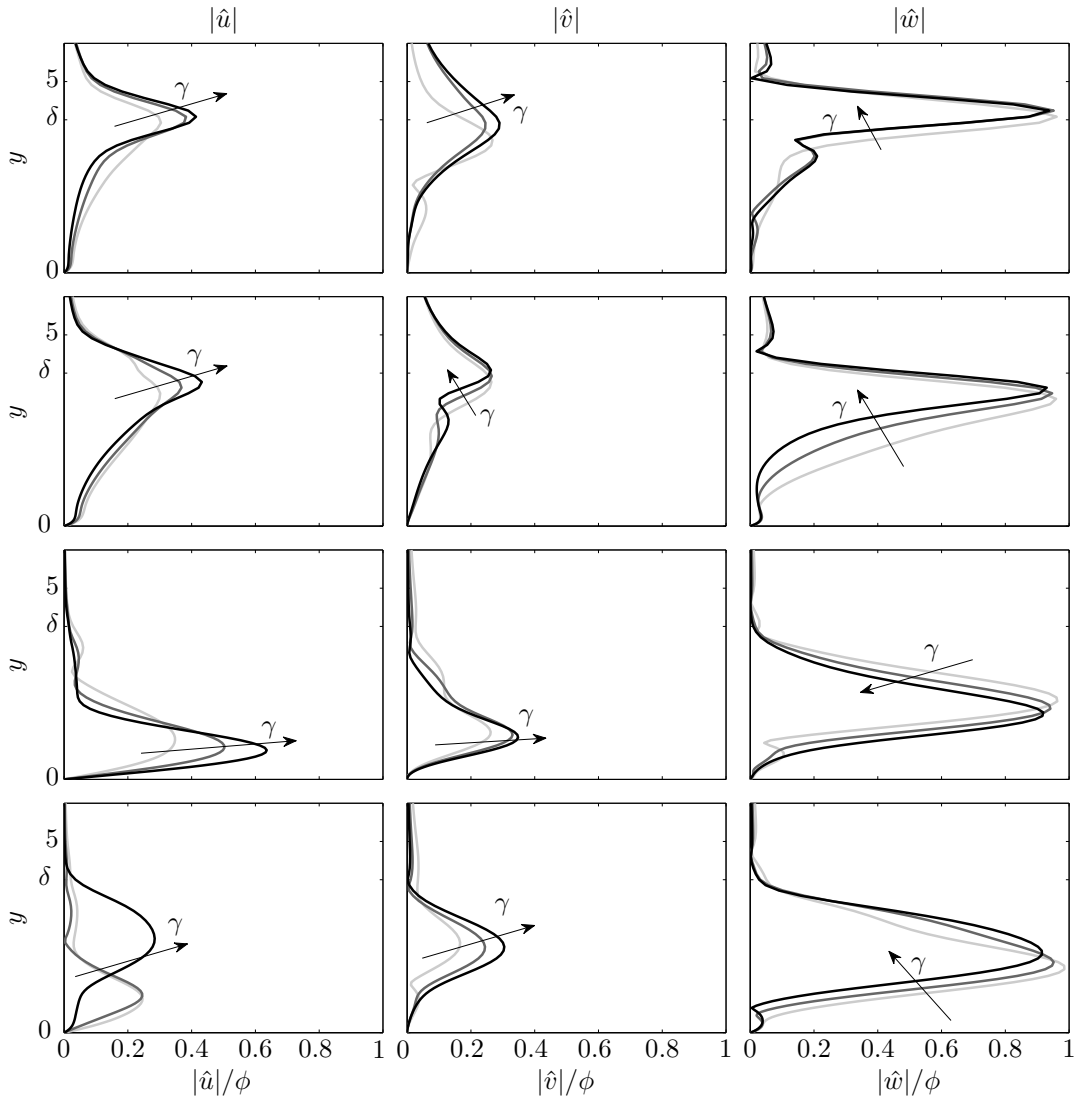

Figure C.17.: Symmetric eigenmodes' velocity profiles over y for varying γ and a relaxation with Ψ_V ($\chi = 0$). The velocities are normalized with $\phi = \max||(\hat{u}, \hat{v}, \hat{w})||$ and plotted through their respective maxima. Parameters hereof are Re = 300 at $z_{extr} = 159$, $L_x = 20$, $L_y = 15$, $N_x = 147$, $N_y = 120$ (**S1**, **S2**), $N_x = 154$, $N_y = 130$ (**S3**, **S4**) and $x_{\text{half}} = L_x/3$, $y_{\text{half}} = L_y/3$ and BC $\hat{u}(x = 0, y) = 0$. Top: **S1**, second row: **S2**, third row: **S3**, bottom: **S4**.

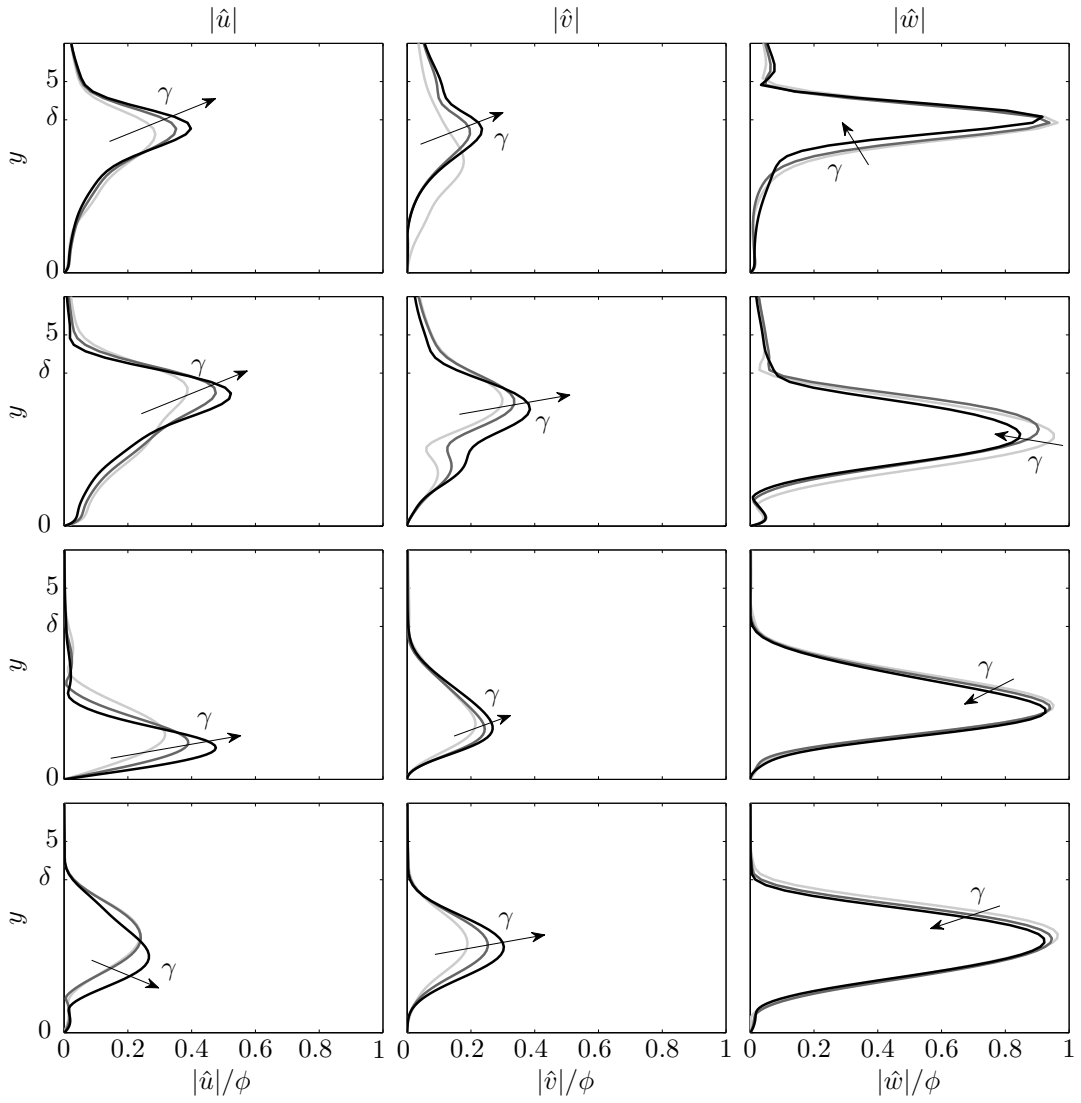

Figure C.18.: Symmetric eigenmodes' velocity profiles over y for varying γ and no relaxation. The velocities are normalized with $\phi = \max||(\hat{u}, \hat{v}, \hat{w})||$ and plotted through their respective maxima. Parameters hereof are Re = 300 at $z_{extr} = 159$, $L_x = 20$, $L_y = 15$, $N_x = 147$, $N_y = 120$ (**S1**, **S2**), $N_x = 154$, $N_y = 130$ (**S3**, **S4**) and $x_{\text{half}} = L_x/3$, $y_{\text{half}} = L_y/3$ and BC $\hat{u}(x = 0, y) = 0$. Top: **S1**, second row: **S2**, third row: **S3**, bottom: **S4**.

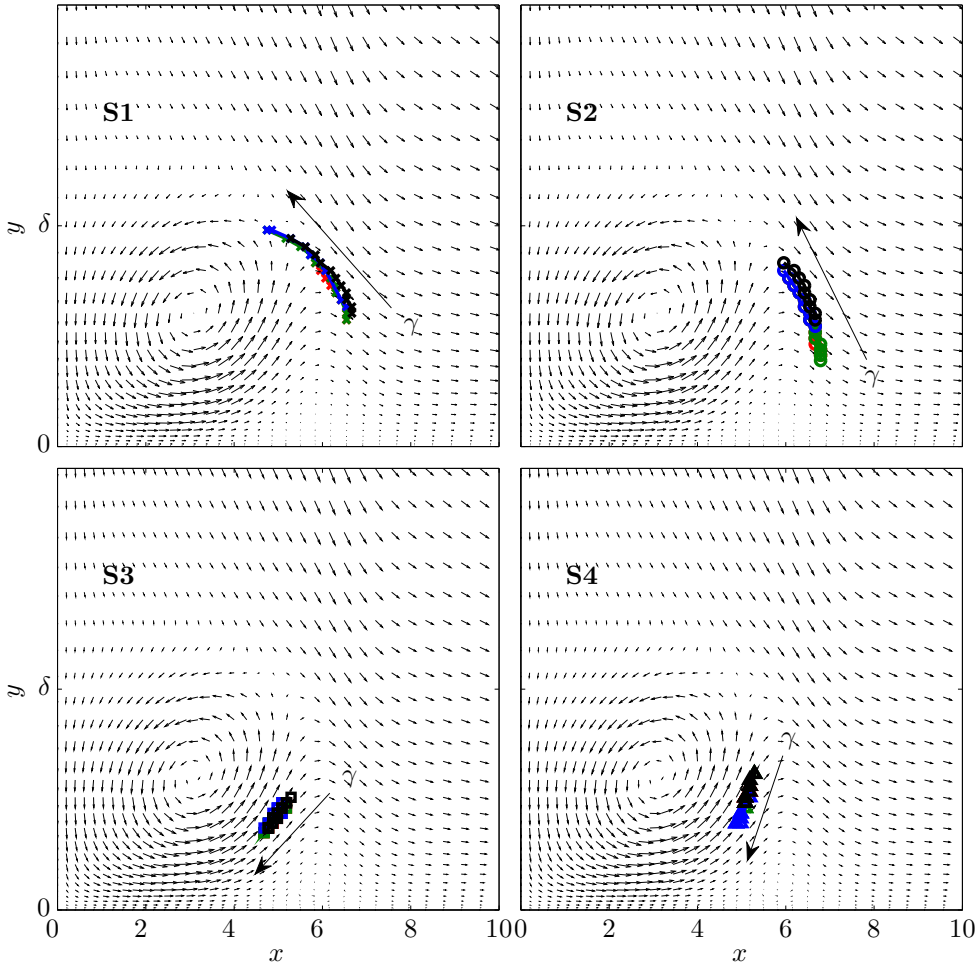

Figure C.19.: Tracks of the maximum values of $|\hat{w}|$ of the symmetric eigenmodes under varying γ for different relaxations. Parameters were set to Re = 300 at $z_{extr} = 94$, $L_x = 20$, $L_y = 15$, $N_x = 147$, $N_y = 120$ (**S1**, **S2**), $N_x = 154$, $N_y = 130$ (**S3**, **S4**) and $x_{\text{half}} = L_x/3$, $y_{\text{half}} = L_y/3$ and BC $\partial^2/\partial x^2 \hat{u}(x = 0, y) = 0$. The colors represent: —Ψ_U, —Ψ_{U+V}, —Ψ_V, —unrelaxed.

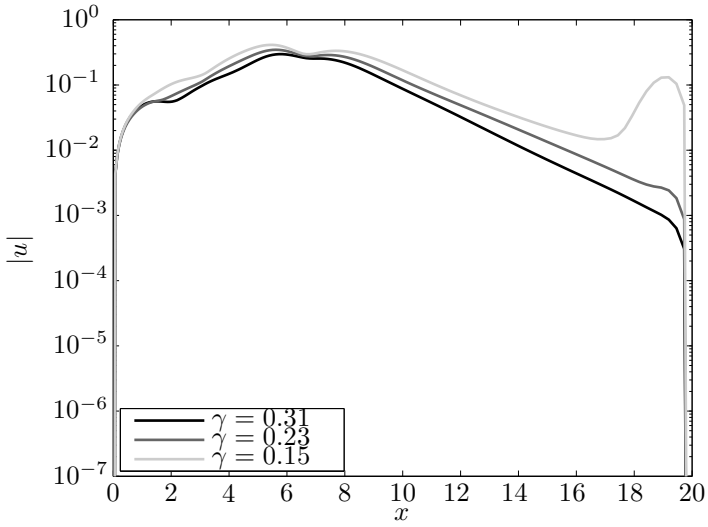

(a) Mode **S1** averaged over $0 \leq y \leq 3.5$

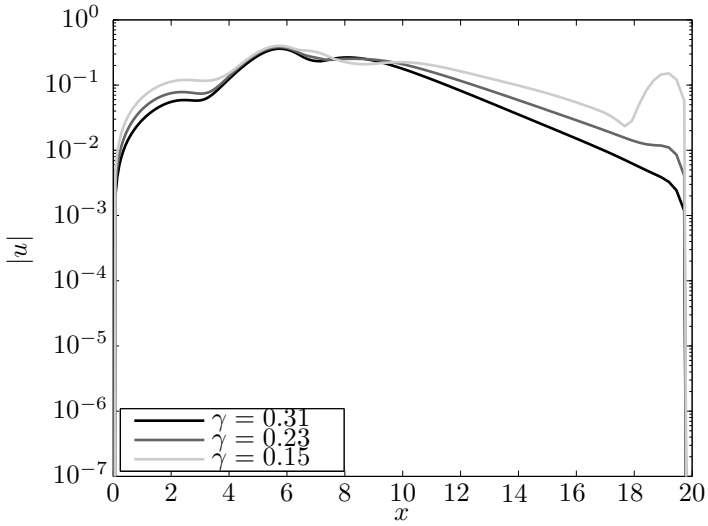

(b) Mode **S2** averaged over $0 \leq y \leq 3.5$

Figure C.20.: The unstable modes' **S1** and **S2** decay along x is influenced at the far-field boundary as γ approaches smaller values. There is a noticeable overshoot at the domain edge for $\gamma \lesssim 0.3$. These simulations were run for parameters Re $= 300$ at $z_{extr} = 94$, $\Psi = \Psi_{UV}$ ($\chi = 0.5$), $L_x = 20$, $L_y = 15$, $N_x = 147$, $N_y = 120$ and $x_{\text{half}} = L_x/3$, $y_{\text{half}} = L_y/3$ and BC $\hat{u}(x = 0, y) = 0$.

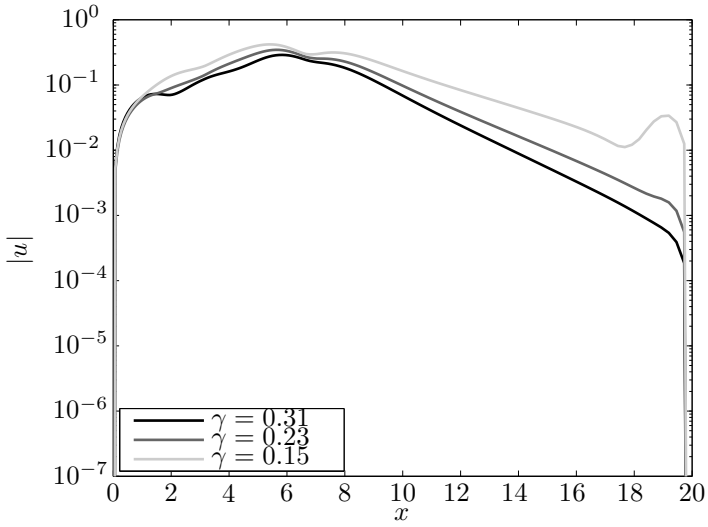

(a) Mode **S1** averaged over $0 \leq y \leq 3.5$

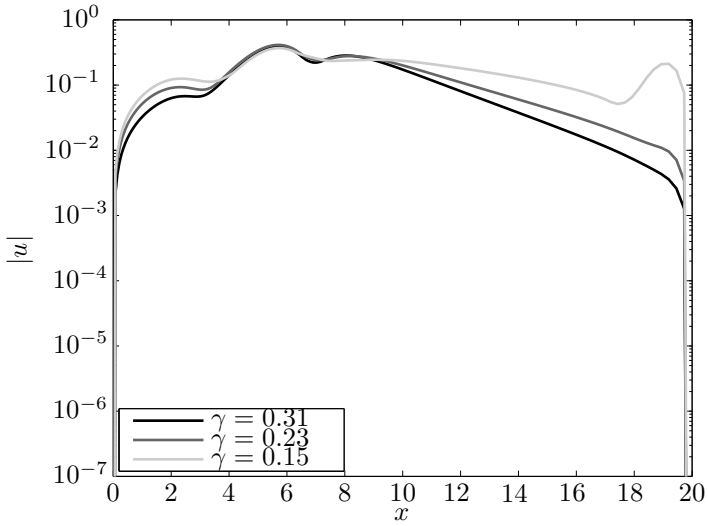

(b) Mode **S2** averaged over $0 \leq y \leq 3.5$

Figure C.21.: The unstable modes' **S1** and **S2** decay along x is influenced at the far-field boundary as γ approaches smaller values. There is a noticeable overshoot at the domain edge for $\gamma \lesssim 0.3$. These simulations were run for parameters Re $= 300$ at $z_{extr} = 94$, $\Psi = \Psi_V$ ($\chi = 0.0$), $L_x = 20$, $L_y = 15$, $N_x = 147$, $N_y = 120$ and $x_{\text{half}} = L_x/3$, $y_{\text{half}} = L_y/3$ and BC $\hat{u}(x = 0, y) = 0$.

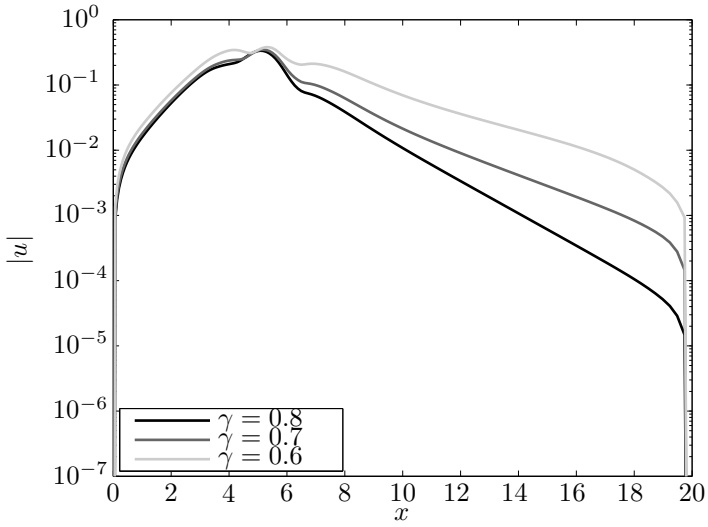

(a) Ψ_{UV}

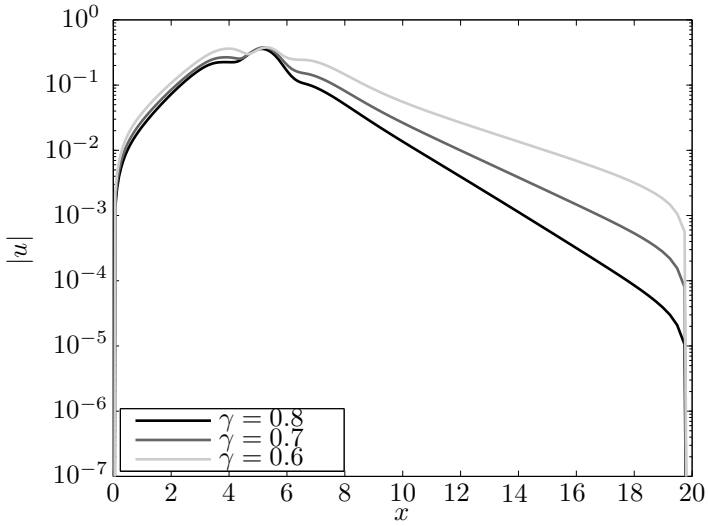

(b) Ψ_V

Figure C.22.: Mode **S4** averaged over $y \in [0, 3.5]$. The stable mode **S4**'s decay along x is influenced at the far-field boundary as γ approaches smaller values. There is a noticeable overshoot at the domain edge for $\gamma \lesssim 0.7$. These simulations were run for parameters Re = 300 at $z_{extr} = 94$, $L_x = 20$, $L_y = 15$, $N_x = 154$, $N_y = 130$ and $x_{\text{half}} = L_x/3$, $y_{\text{half}} = L_y/3$ and BC $\hat{u}(x = 0, y) = 0$.

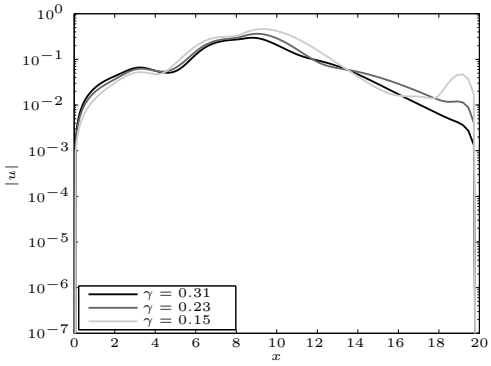

(a) Ψ_U

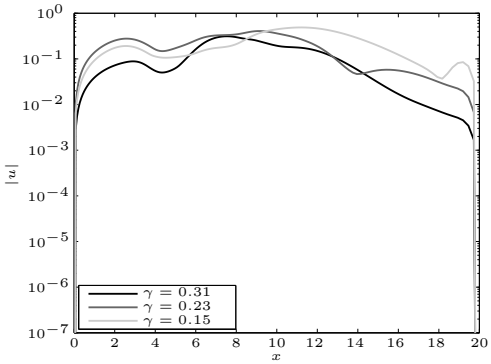

(b) Ψ_{UV}

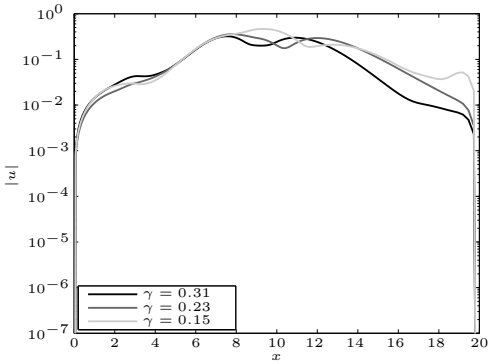

(c) Ψ_V

Figure C.23.: Mode **S1** averaged over $y \in [0, 3.5]$. The unstable mode **S1**'s decay along x is influenced at the far-field boundary as γ approaches smaller values. There is a noticeable overshoot at the domain edge for $\gamma \lesssim 0.3$. These simulations were run for parameters Re $= 300$ at $z_{extr} = 159$, $L_x = 20$, $L_y = 15$, $N_x = 147$, $N_y = 120$ and $x_{\text{half}} = L_x/3$, $y_{\text{half}} = L_y/3$ and BC $\hat{u}(x = 0, y) = 0$.

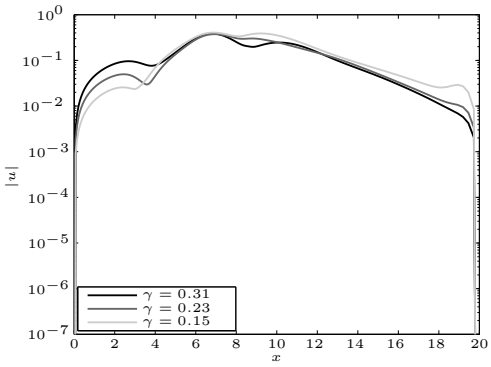

(a) Ψ_U

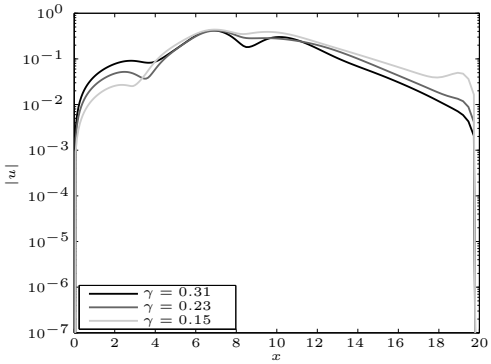

(b) Ψ_{UV}

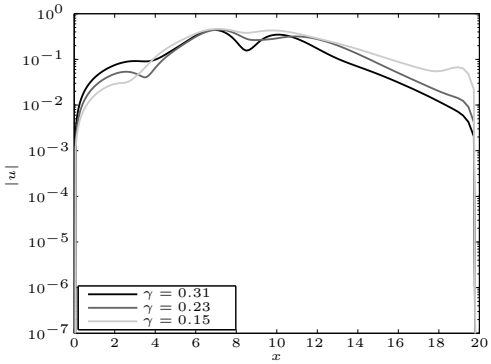

(c) Ψ_V

Figure C.24.: Mode **S2** averaged over $y \in [0, 3.5]$. The stable mode **S2**'s decay along x is influenced at the far-field boundary as γ approaches smaller values. There is a noticeable overshoot at the domain edge for $\gamma \lesssim 0.3$. These simulations were run for parameters $\mathrm{Re} = 300$ at $z_{extr} = 159$, $L_x = 20$, $L_y = 15$, $N_x = 147$, $N_y = 120$ and $x_{\mathrm{half}} = L_x/3$, $y_{\mathrm{half}} = L_y/3$ and BC $\hat{u}(x = 0, y) = 0$.

D. Code

D.1. Creating the Differentiation Matrices

```
function [D,DD] = mod_getDiffMatrix(x)

    % compute first derivative of 4th order
    % compute second derivative of 4th order


    N = size(x,1);
    D = zeros(N);
    DD = zeros(N);

    A = zeros(5,5);

    for j = 3:N-2

        % compute local differentiation matrix A at x = x_j
        for n = 1:5
            Delta = x(j+n-3)-x(j);
            for m = 1:5
                A(n,m) = Delta.^(m-1)/factorial((m-1));
            end
        end


        % invert A and store local differentiation stencil for
        % first and second derivative
        A = inv(A);
         D(j,(j-3)+1:(j-3)+5) = A(2,1:5);
        DD(j,(j-3)+1:(j-3)+5) = A(3,1:5);

    end
    clear A;
    A = zeros(5,5);


    % compute local differentiation matrix for border points
    for n = 1:5
        Delta = x(n)-x(1);
        for m = 1:5
           A(n,m) = Delta.^(m-1)/factorial((m-1));
        end
    end

```

```
43      A = inv(A);
44      D(1,1:5) = A(2,1:5);
45      DD(1,1:5) = A(3,1:5);
46
47      clear A;
48      A = zeros(5,5);
49
50      for n = 1:5
51          Delta = x(N-5+n) - x(N);
52          for m = 1:5
53             A(n,m) = Delta.^(m-1)/factorial((m-1));
54          end
55      end
56      A = inv(A);
57      D(N,(N-5+1):N) = A(2,1:5);
58      DD(N,(N-5+1):N) = A(3,1:5);
59
60      clear A;
61      A = zeros(5,5);
62
63      % compute local differentiation matrix for one point away from border
64      for n = 1:5
65          Delta = x(n)-x(2);
66          for m = 1:5
67             A(n,m) = Delta.^(m-1)/factorial((m-1));
68          end
69      end
70      A = inv(A);
71      D(2,1:5) = A(2,1:5);
72      DD(2,1:5) = A(3,1:5);
73
74      clear A;
75      A = zeros(5,5);
76
77      for n = 1:5
78          Delta = x(N-5+n)-x(N-1);
79          for m = 1:5
80             A(n,m) = Delta.^(m-1)/factorial((m-1));
81          end
82      end
83      A = inv(A);
84      D(N-1,(N-5+1):N) = A(2,1:5);
85      DD(N-1,(N-5+1):N) = A(3,1:5);
86
87
88  end
```

D.2. Implementation of Boundary Conditions

```
function [BCmult, BCadd] = mod_createBCmatrix(Nx, Ny, BCx0y, BCxLy,...
                           BCxy0, BCxyL, Dx1, Dx2, Dy1, Dy2)

    % creates two matrices for BCs specified in strings chordBCs and
    % normBCs, one of which serves as a element-wise multiplicator stencil
    % matrix and the other for superimposing non-zero elements. BCs are
    % formulated for L_aa and R_aa matrices (a equal u or v).
    % structure of eigenfunction u^(x,y) in workspace
    %
    % size(u^) = {Nx*Ny , 1}
    %
    %              /            1         \
    %              |            2         |
    %              |          ...         |
    %              |           Nx         |
    %              | ---------------------|
    %              |           Nx+1       |
    %   u^(x,y) =  |           Nx+2       |
    %              |          ...         |
    %              |         2*Nx         |
    %              | ---------------------|
    %              |         2*Nx+1       |
    %              |         2*Nx+2       |
    %              |          ...         |
    %              | ---------------------|
    %              |          ...         |
    %              \ (Ny-1)*Nx + (Nx-1) /
    %
    % === PARTICULAR LINES ===
    %  x = 0   ([1:Ny]-1)*Nx + [ 1  ]
    %  x = Lx  ([1:Ny]-1)*Nx + [ Nx ]
    %  y = 0   (   [0]  )*Nx + [1:Nx]
    %  y = Ly  ( [Ny-1] )*Nx + [1:Nx]
    NN = Nx*Ny;
    BCmult = double(ones(NN));
    BCadd  = double(zeros(NN,2*NN));

    x0 = ((1:Ny)-1)*Nx + ( 1  );
    xL = ((1:Ny)-1)*Nx + ( Nx );
    y0 = (   (0)  )*Nx + (1:Nx);
    yL = ( (Ny-1) )*Nx + (1:Nx);

    for l = 1:length(BCx0y)
        switch char(BCx0y(l))
            case 'Dirichlet'
               for i = x0
                % BCs for a(x=0,y) =0
                   BCmult(i,:) = 0.;
                   BCadd(i,i)  = 1.;
               end
```

```
51
52
53
54              case 'Neumann'
55
56                  % BCs for da/dx(x=0,y)=0
57                     BCmult(x0,:)    = 0.;
58                     BCadd(x0,1:NN) = Dx1(x0,:);
59
60
61              case 'SecDeriv'
62
63                  % BCs for d2a/dx2(x=0, y)=0
64                     BCmult(x0,:)    = 0.;
65                     BCadd(x0,1:NN) = Dx2(x0,:);
66
67
68              case 'Conti'
69                  % BCs for du/dx(x=0,y) + dv/dy(x=0) = 0
70                     BCmult((x0+1),:) = 0.;
71                     BCadd((x0+1),1:NN) = Dx1(x0,:);
72                     BCadd((x0+1),(NN+1):end) = Dy1(x0,:);
73
74              otherwise
75                  varname=@(x) inputname(1);
76                  disp(['WARNING: No Boundary Conditions at '...
77                      varname(BCx0y) ' set for either u or v!'...
78                      'Please check BCs if not correct.']);
79
80          end
81      end
82
83      for l = 1:length(BCxLy)
84          switch char(BCxLy(l))
85              case 'Dirichlet'
86                  for i = xL
87                  % BCs for a(x=Nx,y)=0
88                     BCmult(i,:) = 0.;
89                     BCadd(i,i)  = 1.;
90                  end
91
92              case 'Neumann'
93                  % BCs for da/dx(x=Nx,y)=0
94                     BCmult((xL-1),:)    = 0.;
95                     BCadd((xL-1),1:NN)  = Dx1(xL,:);
96
97                     BCmult((xL-2),:)    = 0.;
98                     BCadd((xL-2),1:NN)  = Dx1((xL-1),:);
99
100
101             case 'SecDeriv'
102                 % BCs for d2a/dx2(x=Nx,y)=0
103                    BCmult((xL-1),:)    = 0.;
104                    BCadd((xL-1),1:NN)  = Dx2(xL,:);
```

```
105
106             otherwise
107                 varname=@(x) inputname(1);
108                 disp(['WARNING: No Boundary Conditions at '...
109                     varname(BCxLy) ' set for either u or v!'...
110                     'Please check BCs if not correct.']);
111
112
113         end
114     end
115
116     for l = 1:length(BCxy0)
117         switch char(BCxy0(l))
118             case 'Dirichlet'
119                 for i = y0
120                 % BCs for a(x,y=0)=0
121                    BCmult(i,:) = 0.;
122                    BCadd(i,i)  = 1.;
123                 end
124
125
126             case 'Neumann'
127                 % BCs for da/dy(x,y=0)=0
128                    BCmult((y0+Nx),:)    = 0.;
129                    BCadd((y0+Nx),1:NN) = Dy1(y0,:);
130
131
132             case 'SecDeriv'
133                 % BCs for d2a/dy2(x,y=0)=0
134                 disp('Not yet implemented');
135
136
137             otherwise
138                 varname=@(x) inputname(1);
139                 disp(['WARNING: No Boundary Conditions at '...
140                     varname(BCxy0) ' set for either u or v!'...
141                     'Please check BCs if not correct.']);
142
143
144         end
145     end
146
147     for l = 1:length(BCxyL)
148         switch char(BCxyL(l))
149             case 'Dirichlet'
150                 for i = yL
151                 % BCs for a(x,y=Ny)=0
152                    BCmult(i,:) = 0.;
153                    BCadd(i,i)  = 1.;
154                 end
155
156
157             case 'Neumann'
158                 % BCs for da/dy(x,y=Ny)=0
```

```
159                     BCmult((yL-Nx),:)    = 0.;
160                     BCadd((yL-Nx),1:NN) = Dy1(yL,:);
161
162
163             case 'SecDer'
164                 % BCs for d2a/dy2(x,y=Ny)=0
165                 disp('Not yet implemented');
166
167             otherwise
168                 varname=@(x) inputname(1);
169                 disp(['WARNING: No Boundary Conditions at '...
170                     varname(BCxyL) ' set for either u or v!'...
171                     'Please check BCs if not correct.']);
172
173         end
174     end
175 end
```

D.3. Creating the Eigenvalue Matrices

```
function [L,R] = mod_getbiLEBLoperator(x,y,Rey,gamma, U,Uy,V,Vx,Vy,Vyy,...
                 W,Wx,Wy,Wxx,Wxy,Wyy, sing, BCs, baseFlowType)

    %%%%%%%%%%%%%%%%%%%%%%%%%%%%%%%%%%%%%%%%%%%%%%%%%%%%%%%%%%%%%%%%%%%%%%%%
    % define the operators L and R for problem   %
    %                                                                        %
    %  [Luu Luv] [u]     [Ruu Ruv] [u]           %
    %  [       ] [ ] = c [       ] [ ]           %
    %  [Lvu Lvv] [v]     [Rvu Rvv] [v]           %
    %                                                                        %
    %%%%%%%%%%%%%%%%%%%%%%%%%%%%%%%%%%%%%%%%%%%%%%%%%%%%%%%%%%%%%%%%%%%%%%%%
    %
    % INPUT
    %  BCs:             type of boundary conditions to be set
    %  baseFlowType:    type of baseflow (U_b(y), i.e. line vector,
    %                   vs. U_b(x,y), i.e. 2D x-dependent matrix)
    %

    % definitions
    im = sqrt(-1);
    Nx = size(x,1);
    Ny = size(y,1);
    NN = Nx*Ny;
    Idx = eye(Nx);
    Idy = eye(Ny);
    Id  = eye(NN);

    %%% KEEP IN MIND: DX1 AND DX2 ONLY APPLY TO DISTURBANCE QUANTITIES, NOT
    %%% TO BASE FLOW!!
    % compute 4th order first and second derivative, the x direction
    [Dx1,Dx2] = mod_getDiffMatrix(x);
    Dx1 = kron(Idy,Dx1);
    Dx2 = kron(Idy,Dx2);

    % compute 4th order first and second derivative, the x direction
    [Dy1,Dy2] = mod_getDiffMatrix(y);
    Dy1 = kron(Dy1,Idx);
    Dy2 = kron(Dy2,Idx);


    % auxiliary operators
        Laplacex = Dx2 - gamma^2*Id; %partial Laplacian: dx^2 - gamma^2
        Laplacey = Dy2 - gamma^2*Id; %partial Laplacian: dy^2 - gamma^2
        norm  = sing*im*gamma;

    if(strcmp(baseFlowType,'cylinder') || strcmp(baseFlowType,'hiemenz'))
        baseFlowType = 'hiemenz';
        norm  = sing*im*gamma*Rey;
    end

```

```
51      switch baseFlowType
52
53          case 'hiemenz';
54
55              Lop = ( Dx2 + Dy2 + kron(diag(Vy),diag(x))*Dx1 - ...
56                  kron(diag(V),Idx)*Dy1...
57                  - gamma^2*Id - im*gamma*Rey*kron(diag(W),Idx) );
58
59
60              % ================= L ==================================
61                  % dummy matrices (speedup only)
62          %         LopPlusVy = Lop + kron(diag(Vy),Idx);
63          %         LopMinuVy = Lop - kron(diag(Vy),Idx);
64          %         WyD_Dx = im*gamma*Rey*kron(diag(Wy),Idx)*Dx1;
65          %         xVyy = kron(diag(Vyy),diag(x));
66          %         Dx1Dy1 = Dx1*Dy1;
67
68
69
70
71              % obtain BC matrices and set BCs for u
72              [BCmult, BCadd] = mod_createBCmatrix(Nx, Ny, BCs.uBCx0y,...
73                                  BCs.uBCxLy, BCs.uBCxy0, BCs.uBCxyL, Dx1, Dx2, Dy1, Dy2);
74
75              Luu = sparse( (Lop + kron(diag(Vy),Idx))*Laplacex...
76                              .*BCmult + norm*BCadd(:,1:NN) );
77              Ruu = sparse( -Laplacex...
78                              .*BCmult + BCadd(:,1:NN) );
79              Luv = sparse( ((Lop + kron(diag(Vy),Idx))*Dx1*Dy1...
80                              + im*gamma*Rey*kron(diag(Wy),Idx)*Dx1...
81                              - gamma^2*kron(diag(Vyy),diag(x)))...
82                              .*BCmult + norm*BCadd(:,(NN+1):end) );
83              Ruv = sparse( -Dx1*Dy1...
84                              .*BCmult + BCadd(:,(NN+1):end) );
85
86              % obtain BC matrices and set BCs for v
87              [BCmult, BCadd] = mod_createBCmatrix(Nx, Ny, BCs.vBCx0y,...
88                                  BCs.vBCxLy, BCs.vBCxy0, BCs.vBCxyL, Dx1, Dx2, Dy1, Dy2);
89
90              Lvu = sparse( ((Lop - kron(diag(Vy),Idx))*Dx1*Dy1...
91                              - im*gamma*Rey*kron(diag(Wy),Idx)*Dx1...
92                              + kron(diag(Vyy),diag(x))*Dx2)...
93                              .*BCmult );
94              Rvu = sparse(  -Dx1*Dy1...
95                              .*BCmult );
96              Lvv = sparse( ((Lop - kron(diag(Vy),Idx))*Laplacey...
97                              + im*gamma*Rey*kron(diag(Wyy),Idx)...
98                              + kron(diag(Vyy),diag(x))*Dx1*Dy1)...
99                              .*BCmult + norm*BCadd(:,1:NN) );
100             Rvv = sparse(  -Laplacey...
101                             .*BCmult + BCadd(:,1:NN) );
102
103             clear BCmult BCadd;
104
```

```
105
106         case 'impact'
107
108             % create large operator
109             Lop = (Dx2 + Dy2 - gamma^2*Id)/Rey - (diag(U(1:end))*Dx1...
110                     + diag(V(1:end))*Dy1 + diag(W(1:end))*im*gamma);
111
112             % obtain BC matrices and set BCs for u
113             [BCmult, BCadd] = mod_createBCmatrix(Nx, Ny, BCs.uBCx0y,...
114                                 BCs.uBCxLy, BCs.uBCxy0, BCs.uBCxyL, Dx1, Dx2, Dy1, Dy2);
115
116             Luu = sparse((  ( Lop+diag(Vy(1:end)) )*Laplacex + im*gamma*diag(Wxx(1:end))...
117                              -diag(Vx(1:end))*Dx1*Dy1)...
118                                .*BCmult + norm*BCadd(:,1:NN) );
119             Ruu = sparse( -Laplacex...
120                             .*BCmult + BCadd(:,1:NN) );
121             Luv = sparse( (( Lop+diag(Vy(1:end)) )*Dx1*Dy1...
122                              + im*gamma*diag(Wy(1:end))*Dx1 - diag(Vx(1:end))*Dy2...
123                              -im*gamma*diag(Wx(1:end))*Dy1...
124                              + gamma^2*diag(Uy(1:end)) + im*gamma*diag(Wxy(1:end)))...
125                                .*BCmult + norm*BCadd(:,(NN+1):end));
126             Ruv = sparse( -Dx1*Dy1...
127                     .*BCmult + BCadd(:,(NN+1):end) );
128
129             % obtain BC matrices and set BCs for v
130             [BCmult, BCadd] = mod_createBCmatrix(Nx, Ny, BCs.vBCx0y,...
131                                 BCs.vBCxLy, BCs.vBCxy0, BCs.vBCxyL, Dx1, Dx2, Dy1, Dy2);
132
133             Lvu = sparse( (( Lop-diag(Vy(1:end)) )*Dx1*Dy1...
134                              + im*gamma*diag(Wx(1:end))*Dy1 - diag(Uy(1:end))*Dx2...
135                              - im*gamma*diag(Wy(1:end))*Dx1...
136                              + gamma^2*diag(Vx(1:end))+im*gamma*diag(Wxy(1:end)))...
137                                .*BCmult);
138             Rvu = sparse(  -Dx1*Dy1...
139                             .*BCmult );
140             Lvv = sparse( (( Lop-diag(Vy(1:end)) )*Laplacey...
141                              + im*gamma*diag(Wyy(1:end)) -diag(Uy(1:end))*Dx1*Dy1)...
142                                .*BCmult + norm*BCadd(:,1:NN));
143             Rvv = sparse(  -Laplacey...
144                             .*BCmult + BCadd(:,1:NN) );
145
146             clear BCmult BCadd;
147
148     end
149
150     % build L
151     if(~strcmp(baseFlowType,'impact'))
152         L = [Luu Luv ; Lvu Lvv]/(im*gamma*Rey);
153     else
154         L = [Luu Luv ; Lvu Lvv]/(im*gamma);
155     end
156     clear Luu Luv Lvu Lvv;
157     clear LopPlusVy LopMinuVy WyD_Dx xVyy;
158
```

```
159     % build R
160     R = [Ruu Ruv ; Rvu Rvv];
161     clear Ruu Ruv Rvu Rvv;
162
163 end
```

E. Supplement